Investigation of the tunneling emitter bipolar transistor as spin-injector into silicon

by

Marc Julien van Veenhuizen

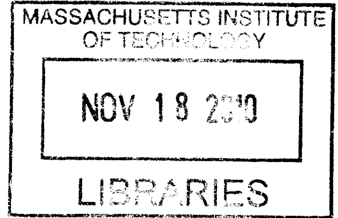
MASSACHUSETTS INSTITUTE OF TECHNOLOGY
NOV 18 2010
LIBRARIES
ARCHIVES

Submitted to the Department of Physics
in partial fulfillment of the requirements for the degree of

Doctor of Philosophy

at the

MASSACHUSETTS INSTITUTE OF TECHNOLOGY

February 2010

© Massachusetts Institute of Technology 2010. All rights reserved.

Author . . . .
Department of Physics
December 17, 2009

Certified by . . . .
Jagadeesh S. Moodera
Research Scientist
Thesis Supervisor

Certified by . . . .
Mildred S. Dresselhaus
Professor
Thesis Supervisor

Accepted by . . . .
Thomas J. Greytak
Professor, Associate Department Head for Education

Investigation of the tunneling emitter bipolar transistor as spin-injector into silicon

by

Marc Julien van Veenhuizen

Submitted to the Department of Physics
on December 21, 2009, in partial fulfillment of the
requirements for the degree of
Doctor of Philosophy

Abstract

In this thesis is discussed the tunneling emitter bipolar transistor as a possible spin-injector into silicon. The transistor has a metallic emitter which as a spin-injector will be a ferromagnet. Spin-polarized electrons from the ferromagnet tunnel directly into the conduction band of the base of the transistor and are subsequently swept into the collector. The tunneling emitter bipolar transistor as a spin-injector allows for large spin-polarized currents and naturally overcomes the conductivity mismatch and Schottky barrier formation. In this work, the various aspects of the transistor are analyzed. The transfer of spin-polarization across the base-collector junction is simulated. The oxide MgO is considered as a tunnel barrier for the transistor. Electron spin resonance is proposed as a measurement technique to probe the spin-polarization injected into the collector. The fabrication of the transistors is discussed and the importance of the tunnel barrier for the device operation is fully analyzed. The observation of negative differential transconductance in the transistor is explained.
A number of side- or unrelated studies are presented as well. A study on scattered and secondary electrons in e-beam evaporation is described. Spin-orbit coupling induced spin-interference of ring-structures is proposed as a spin-detector. A new measurement technique to probe bias dependent magnetic noise in magnetic tunnel junctions is proposed. Also, an IV fitting program that can extract the relative importance of the tunnel and Schottky barrier is discussed and employed to fit the base-emitter IV characteristics of the transistor. The development of several fabrication and experimental tools is described as well.

Thesis Supervisor: Jagadeesh S. Moodera
Title: Research Scientist

Thesis Supervisor: Mildred S. Dresselhaus
Title: Professor

Acknowledgments

Several people directly or indirectly provided help during my PhD research.

I gratefully thank Jagadeesh Moodera for his support over the years and for allowing me the freedom to pursue my own ideas.

I am indebted to Millie Dresselhaus for always willing to take time out of her schedule to provide advise.

I also thank the other members of my thesis committee, Pablo Jarillo-Herrero and Patrick Lee, for the insightful discussions.

It is a pleasure to acknowledge Anatoly Dementyev, Sekhar Ramanathan and David Cory for collaborating on the ESR experiments.

Many thanks also to Ron DeRocher and David Johnson for lots of advise on and assistance with machining.

I give thanks to Bernard Alamariu and Kurt Broderick for the numerous helpful discussions about processing.

It was as well a pleasure to collaborate with Ya-Hong Xie on the SiGe project; although not realized until so far, the research was very interesting and insightful.

I am grateful to Nicolas Locatelli who helped a lot during the initial stages of the epiwafer research.

I also enjoyed discussing with Mark Hickey, Guo-Xing Miao, Joonyeon Chang, Martina Müller, Marius Costache, Karthik V.Raman, Sjors Schellekens, and John Philip.

My gratitude goes as well to Oliver Dial and Gary Steele for teaching me so much about experiments and programming, and to Ray Ashoori for bringing me to MIT.

Of all the good things MIT has to offer, I will miss most David Bono's lab where so many ingenious experiments are realized as possibly only one person can do. Being able to experience David's organizational skills, eye for detail, and his readiness to share his unique insights has been especially rewarding.

A special thanks to my parents Coen and Marianne and my sister Dominique for their continuous support, to my grandparents opa Wim and oma Els and all my other family-members for their interest in my research, hospitality, and for being a

great family.

This work was sponsored by:

KIST-MIT project

DARPA W911NF-08-1-0087

NSF DMR 0504158

ONR N00014-09-1-0177

Contents

1 Introduction **13**

1.1 Short overview of semiconductor spintronics 13

1.2 Tunneling emitter bipolar transistor as spin-injector into silicon . . . 17

2 Medici simulation of the tunneling emitter bipolar transistor **21**

2.1 Effect of emitter work function on the transistor 21

2.2 Effect of tunnel barrier height 23

2.3 Setting the base voltage instead of base current 26

2.4 Effect of tunnel barrier width 27

2.5 Effect of base doping 28

3 Spin transport through a PN junction **33**

3.1 Theory of spin in PN junctions 33

3.2 Simulation results 34

4 The growth of MgO on silicon **41**

4.1 Band structure of MgO 41

4.2 Fe/MgO on silicon 44

4.3 Epitaxial growth of MgO on silicon 46

5 Electron Spin Resonance as a probe to detect spin-injection **51**

5.1 Electron Spin Resonance defined 51

5.2 Spin-detection 54

5.3 ESR on 1st generation transistors 56

6 Fabrication of the tunneling emitter bipolar transistor 59

6.1 Epiwafer transistors 59

6.1.1 Thinning down the base 60

6.1.2 Collector and base definition 61

6.1.3 Emitter definition 62

6.2 2nd generation transistors 63

6.2.1 Wafer choice 63

6.2.2 Device shape 64

6.2.3 Isolation of the transistors 65

6.2.4 Backside etch 65

6.2.5 Active area 67

6.2.6 Ion implantation 67

6.2.7 Cut of Emitter-Base 68

6.2.8 Base definition 68

6.3 Wafer pieces 69

6.3.1 Emitter definition (1) 69

6.3.2 Emitter definition (2) 70

7 Observation of Negative Differential Transconductance in tunneling emitter bipolar transistors 73

7.1 Negative differential transconductance in tunneling emitter bipolar transistors 75

7.1.1 Introduction 75

7.1.2 Device fabrication 76

7.1.3 Measurement results 76

7.1.4 Simulation of the NDTC 77

7.1.5 Conclusions 81

8 On the gain of tunneling emitter bipolar transistors 83

8.1 NPN BJT 83

8.1.1 Temperature dependence of current gain 86

8.2 Tunneling emitter bipolar transistor 88
8.2.1 Temperature dependence of current gain 91
8.3 Epiwafer transistors 92
8.4 Implanted base transistors, emitter (1) 94
8.5 Implanted base transistors, emitter (2) 102

9 The influence of spin-polarization on the $h/2e$ and h/e oscillations of ring-structures in the presence of the Rashba Spin-Orbit Interaction 111

9.1 Introduction 112
9.2 Rashba induced interference in ring-structures 113
9.2.1 Counter-clockwise rotation for the circle 115
9.2.2 Interference intensity round-trip 117
9.2.3 Interference intensity half-way 118
9.3 Aharonov-Bohm oscillation amplitude modulations 119
9.3.1 $\frac{h}{2e}$ oscillations 120
9.3.2 $\frac{h}{e}$ oscillations 121
9.3.3 Influence of Larmor precession 122
9.3.4 Experimental observability 124
9.4 Multiple rings 125

10 Electron deflector in UHV system: scattered electrons in e-beam evaporation 131

10.1 Introduction 131
10.2 Electron deflector 133
10.3 Measurements: Iron 133
10.3.1 $V_{sample} = 0$ V 133
10.3.2 $V_{sample} = -100$ V 136
10.3.3 $V_{sample} = 100$ V 139
10.4 Measurements: MgO 139
10.5 Conclusion 140

11 Conclusion **143**

A Modelling with TSUPREM4 **145**

A.1 The growth of silicon-oxide 145

A.2 Ion implantation 146

B MEDICI simulation model and additional results **149**

B.1 Import from TSUPREM4 149

B.2 Setting up the grid 149

B.3 Tunneling model 151

B.4 Transistor action plots for varying base currents 151

C Machining and electronics **157**

C.1 Measurement probes 157

C.2 Spin-coater head 158

C.3 Annealing boat 159

C.4 Electron deflector 160

C.5 Probe station 160

C.5.1 Base plate 161

C.5.2 Sample stage 161

C.5.3 Probe holder 162

C.6 Curve tracer 163

D Current-voltage characteristics and curve fitting **167**

D.1 Modelling the MIS tunnel diode 167

D.1.1 Tunnel barrier 168

D.1.2 Schottky barrier 169

D.1.3 Tunnel and Schottky barriers together 170

D.2 IV fitting of data 170

D.2.1 MgO on epiwafer 171

D.2.2 Thermal oxide tunnel barrier 171

D.2.3 Al_2O_3 tunneling barrier grown with ALD 172

D.2.4 Resonant tunneling via an inversion layer 174
D.2.5 Fitting parameter influence on IV 176

E Differential magnetoresistance (DMR) 179

E.1 Previous results and new proposal on DMR 179
E.2 Electronics 180
E.2.1 AC current source 181
E.2.2 Band-pass filter 182

Chapter 1

Introduction

1.1 Short overview of semiconductor spintronics

Over the last two decades major advances in spintronics research have been made [1]. Starting from all-metal based spintronics in the seminal experimental work [2], and the highly successful giant magnetoresistance stacks [3], spintronics has branched out to semiconductors as well which, owing to their in general longer spin-coherence lengths as well as their engineering feasibility are promising materials for new or better device technology.

Conventional sources of spin-polarization are the 3d ferromagnets whose high Curie temperatures as well as their ease of fabrication make them a logical choice as sources of spin-current into semiconductors. A main issue involved in incorporating ferromagnetic metals with semiconductors however is the conductivity mismatch which hinders efficient spin-injection [4], the reason being that an applied bias will mainly drop across the semiconductor because its high intrinsic resistance dominates. Since the semiconductor is not spin-polarized, the driving electric field mainly results in spin-unpolarized current. Theoretically it has been shown that an interfacial barrier may mitigate the conductivity mismatch [5],[6] if its resistance becomes comparable to or larger than that of the semiconductor. The nature of the barrier may be spin-selective such as for instance Eu based ferromagnetic insulators [7] or crystalline Fe/MgO(100) [8] but even spin-independent barriers such as Al_2O_3 [9] work since the

tunneling current depends on the density of states of the ferromagnet [10]. Also the naturally formed Schottky barrier may act as an efficient tunnel barrier [11].

Spin-injection into the direct band-gap semiconductor GaAs has been explored thoroughly. The direct band gap together with the quantum selection rules allows for optical spin-injection which has been demonstrated in a set of visionary experiments using time-resolved Faraday rotation as a probe of the induced spin-polarization, see [12] and references therein. In addition, extensive research has been done on electrical spin-injection from a ferromagnet into GaAs with the injected spin-efficiency detected optically. The typical optical detection structure used is the spin LED [13, 14] and consists of an n(-doped)-i(ntrinsic)-p(-doped) semiconductor layer structure. Spin-polarized electrons electrically injected into the n-doped region radiatively recombine with unpolarized holes from the p-doped layer in the intrinsic active region. If the intrinsic region forms a quantum well then due to quantum confinement, the heavy hole (HH) and light hole (LH) energy bands are split such that the polarization of the emitted light directly reflects the polarization of the injected electrons. Otherwise the quantum selection rules [15] give a maximum light polarization of 50%.

Several different approaches have been followed to maximize spin-injection efficiency. Diluted magnetic semiconductors have been used [16] as spin-injectors yielding very efficient spin-injection but having the draw-back of requiring low operating temperatures because of their low Curie temperatures. Also ferromagnetic metals have been incorporated as the spin-injector and two basic approaches to overcome the conductivity mismatch have been followed: spin-injection through the Schottky barrier [17], and spin-injection through a tunnel barrier such as Al_2O_3 [18, 19] and MgO [20]. In the case of the Schottky barrier, often a thin highly n-doped contact layer is included directly below the ferromagnet [21] in order to minimize the depletion region width where electron-hole recombination reduces the spin-injection efficiency. This is especially important since the Schottky barrier is reverse biased in order to inject spin-polarized electrons. Spin-injection through forward biased Schottky barriers, i.e. polarization of the semiconductor by spin-dependent reflection from the ferromagnet, has also been observed experimentally [22] but intrinsically suffers

from the spin-current having to diffuse against the drift current, i.e. upstream, which yields a smaller spin-coherence length as theoretically shown in [23, 24, 25, 26] and experimentally in [27]. The theoretical investigations show that the downstream spin-current decays with a spin-coherence length L_d and the upstream spin-current with spin-coherence length L_u , both of them strongly dependent on electric field but in an opposite way, such that the intrinsic spin-coherence length L_s is equal to the geometric mean of the two, i.e. $L_s^2 = L_u \times L_d$. In fact it has been argued [23, 24] that high electric fields may increase the spin-injection efficiency since the effective resistance of the semiconductor is proportional to the upstream spin-coherence length which becomes smaller with increasing electric field, giving a reduction in the conductivity mismatch. Choices of spin-sources range from conventional 3d ferromagnets such as Fe [21] to lattice-matched MnAs [28] with accompanying high-quality interfaces which have been shown [29] to affect spin-injection efficiency.

With the injected spin-polarized electrons in GaAs a whole range of spin-dependent phenomena has been investigated. Electrically injected spin-polarized electrons have been observed to polarize the nuclei via the hyperfine interaction [30, 31, 32]. Furthermore, the effect of semiconductor carrier concentration on spin-relaxation has been investigated and it was found [33] that higher doping concentrations decrease the D'yakonov-Perel (DP) spin-relaxation rate (ch.11 of [15]) by faster thermalization. In addition, the influence of temperature on the injected spin has been investigated and found to be rather weak both optically [34] and electrically [35] with in the latter case a possible reason being the reduction of DP spin-relaxation by motional narrowing. The electrical spin-injection itself may be reduced by increasing the temperature because of field-assisted thermionic emission which is spin-unpolarized [35]. In addition, spin-orbit coupling of injected spins has been probed and quantified [36]. For zinc blende semiconductors, such as GaAs, the conduction band spin-splits because of the bulk inversion asymmetry as shown by Dresselhaus in the founding article of spintronics [37]. For semiconductor quantum well structures, the asymmetric doping profile gives rise to a net interfacial electric field which induces spin-orbit coupling in the quantum well as investigated by Bychkov and Rashba [38]. The effect of strain

on spin-orbit interaction (SOI) has been investigated and perpendicular strain has been shown to alter the Dresselhaus SOI [39, 40] whereas lateral strain gives rise to a Rashba type SOI [41, 42]. Also, it has been demonstrated that the Rashba SOI strength in quantum wells can be altered either by using a gate voltage [43] or by changing the doping profile [44], both of which affect the average position of the electron wavefunction and hence the average interfacial electric field experienced by the electron. Consequently, manipulation of spin via SOI as envisioned in the Datta-Das spin field effect transistor [45] is feasible as has been demonstrated in [46].

All-electrical spin-injection and detection experiments on GaAs (based structures) have also been done in [47], [48] and recently in [49], [50] where in the latter a Hanle spin-precession [51] of the injected spin is observed. Nevertheless, the tremendous progress made on spintronics in GaAs was mainly facilitated by having optical means either to inject or to detect spin-polarization.

In that respect, the indirect band-gap of *silicon*, necessating the need of phonons for either excitation or recombination has long kept these optical means at bay. Consequently, silicon spintronics research has fallen behind GaAs based with only recently the reports of major breakthroughs. Spin-detection using a spin LED structure made out of silicon has now been demonstrated [52]. It has now as well been demonstrated that charge can be excited across the indirect band-gap [53]. Optical spin-pumping still remains elusive although schemes have been devised [54] which may become possible. However, at present, spin-injection into silicon [55] has to be done electrically. Electrical spin-injection and detection in silicon is currently an active and productive field of research after the success of [56] where a hot-electron transistor was used as a spin-injector in which the high energy electrons become spin-polarized by tunneling through a ferromagnet. Spin-injection and nonlocal detection has been obtained using both Al_2O_3 tunnel barriers [57] and Fe_3Si Schottky barriers [58]. Very recently, room-temperature spin-injection has been realized [59]. That work also demonstrated injection of spin-polarization into P-type silicon, in the form of spin-polarized holes.

All the recent progress is good news for spintronics. Namely, silicon is a promising spintronics material because it has a long spin-coherence length [60], resulting from

the absence of Dresselhaus SOI by inversion symmetry and the little other SOI because of the low mass (i.e. nuclear charge), and the negligible hyperfine interaction (most abundant isotope ^{28}Si has zero nuclear spin, and the concentration of the spin-$\frac{1}{2}$ isotope ^{29}Si is only about 4.7% [61]). Furthermore, silicon is abundant and widely used in industry. Although spin-manipulation via the SOI is not feasible in silicon, recently a different spin-manipulation scheme in silicon has been demonstrated to success [62] using electrostatic modulation of the spin-polarization.

1.2 Tunneling emitter bipolar transistor as spin-injector into silicon

In all the work described above, spin was injected into the semiconductor being tied to a majority charge carrier. All but one ([62]) considered N-type semiconductors as the medium. This work will focuss on a completely different approach to electrical spin-injection, based on a heterojunction bipolar transistor.
Bringing a ferromagnetic metal into contact with a semiconductor will give rise to Schottky barrier formation. Although spin-injection through Schottky barriers is well-established and effective, reverse biasing the Schottky barrier increases its resistance and hence limits the current flow whereas forward biasing suffers from the short upstream spin-coherence length (i.e. poor spin-extraction). Using a magnetic semiconductor instead as a spin-source has the disadvantage of a rather low Curie temperature but also from a reduction of spin-injection efficiency with increasing bias as a result of band-bending of the magnetic semiconductor [63].
The approach in this work will naturally solve excessive Schottky barrier formation. Namely, here electron spins are injected from a ferromagnetic metal into P-type silicon as *minority carriers*. Since the minority diffusion length is rather short, it is necessary to extract the carriers quickly. This can be done by incorporating the P-type silicon as a silicon PN junction. The electric field of the PN junction will then readily sweep the minority electrons into the N-type region where they will further

drift-diffuse. PN junctions form the basic component of the spin-LED as described above. For the spin-LED however the spin-polarized electrons recombine in an intrinsic region separating the N- and P-regions hence the spins do not travel through the PN junction itself. Theory [64, 65] predicts though that spin may cross PN junctions quite efficiently. Experimentally [66, 67], spin transport through a magnetic PN junction has been demonstrated.

Together with the ferromagnet, the structure resembles a bipolar junction transistor with the ferromagnet being the emitter, and the P-type and N-type silicon being the base and collector, respectively, as shown in Fig. 1-1. In the active biasing region

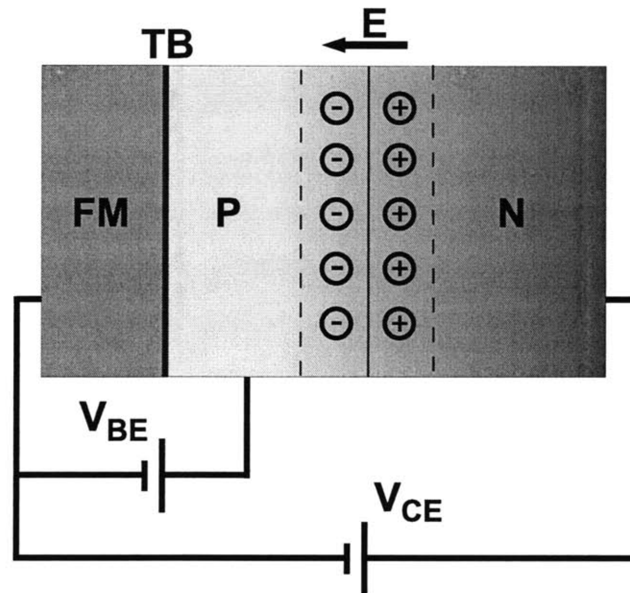

Figure 1-1: Tunneling emitter bipolar transistor as spin injector into silicon. The FM denotes the ferromagnet which forms the emitter, TB stands for tunnel barrier, and P and N indicate the P-doped and N-doped silicon that form the base and collector, respectively. The transistor is hooked up in the common emitter geometry.

the ferromagnet-semiconductor Schottky barrier is forward biased allowing for large current flow. Spin-injection into the N-doped silicon collector can be electrically controlled with a base voltage. It is emphasized that an indirect band-gap semiconductor such as silicon is particularly well suited for this approach because it suppresses the electron-hole recombination which would otherwise degrade the electron current flow

in the base region, limiting spin-injection efficiency [68]. One (as it turns out) crucial addition is needed, namely a tunnel barrier separating the ferromagnet and P-type silicon electrostatically. In addition, the tunnel barrier also prevents the precipitation of the emitter metal into silicon, potentially yielding an interfacial magnetically dead layer (although these layers need not necessarily form as demonstrated for iron on GaAs [69]). Moreover, the tunnel barrier will naturally solve the conductivity mismatch issue since in the active region of the transistor it will easily dominate the base-emitter resistance. With this addition, the transistor may rightly be called a *tunneling emitter bipolar transistor*. Using this transistor as a spin-injector may have several advantages over other schemes. For instance it will allow for large spin-currents, being a bipolar transistor. Also, it is a 3-terminal device enabling more control and variability than 2-terminal approaches.

In this work the tunneling emitter bipolar transistor as spin-injector into silicon will be systematically investigated. First, in Ch. 2, simulation results will be presented that focus on the transistor action of the device. Next, in Ch. 3, simulations of the spin transport through PN junctions will be given that illustrate that the transistor can be used as a spin-injector. In Ch. 4 the oxide MgO is analyzed as a possible tunnel barrier for the transistor. Ch. 5 deals with using Electron Spin Resonance (ESR) as a potential detector of the spin injected into the collector of the transistor. ESR is potentially well suited to probe the injected spin in these devices because of their vertical structure and the large collector currents. Ch. 6 is dedicated to describing how the tunneling emitter transistor is fabricated. Two different generations of transistors have been fabricated, the first based on epiwafers and the second on implanted base transistors. In Ch. 7 is analyzed the negative differential transconductance observed in the first generation transistors. Ch. 8 focusses solely on the current gain of the transistor, giving both theoretical and experimental results. In Ch. 9 a digression is made to spin-orbit coupling induced spin-interference in ring-structures where it is argued that ring-structures can be used as a spin-detector. The final chapter, Ch. 10, describes an experiment on electron beam evaporation, analyzing the presence of scattered and secondary electrons.

Several Appendices support and further clarify this work. App. A describes how TSUPREM4 is invoked in the device fabrication whereas App. B gives details about the use in this work of the device simulator MEDICI. A significant part of the research was spent on the development of fabrication and measurement tools which is presented in App. C. In App. D IV characteristics of the base-emitter junction are analyzed in the light of spin-injection requirements. App. E is somewhat outside this study; it proposes a measurement technique to probe the effect of magnetic domain switching on the magnetoresistance of magnetic tunnel junctions.

Although this work has not yet succeeded in proving that the tunneling emitter bipolar transistor can inject electron spin into silicon, it will extensively be argued that it is a promising and feasible approach. In addition, interesting findings have been made along the way. This research will then facilitate future experiments on spin-injection using the tunneling emitter bipolar transistor.

Chapter 2

Medici simulation of the tunneling emitter bipolar transistor

In this Chapter the tunneling emitter bipolar transistor is simulated with the 2-dimensional device simulator MEDICI. The precise working of this transistor is analyzed in Ch. 8. In Appendix B are given the simulation model used as well as additional simulation results.

The schematic of the tunneling emitter bipolar transistor is given in Fig. 1-1. It consists of a metallic emitter, separated from a silicon PN junction by a tunnel barrier. Below the influence of emitter, tunnel barrier, and base characteristics on the device performance are simulated. Unless otherwise stated, the silicon PN junction corresponds to the implanted base with implant oxide thickness 120 nm of Fig. A-2. The simulations model the device in the common emitter geometry, as depicted in Fig. 1-1.

2.1 Effect of emitter work function on the transistor

In order to probe how the work function of the metal emitter influences the transistor behavior, different values for the emitter work function have been chosen. In this

study the tunnel barrier affinity is kept at 3.0 eV which would correspond to a tunnel barrier height, compared to the electron affinity of silicon, of about 1.1 eV. In Sec. 2.2 the influence of the tunnel barrier height on the device performance is studied. In Fig. 2-1 are shown the collector I_c and base I_b currents, as a function of base-emitter voltage V_{be} (called Gummel plots) for several emitter work function values ranging across the bandgap. From Fig. 2-1 it can be inferred that the effect of the

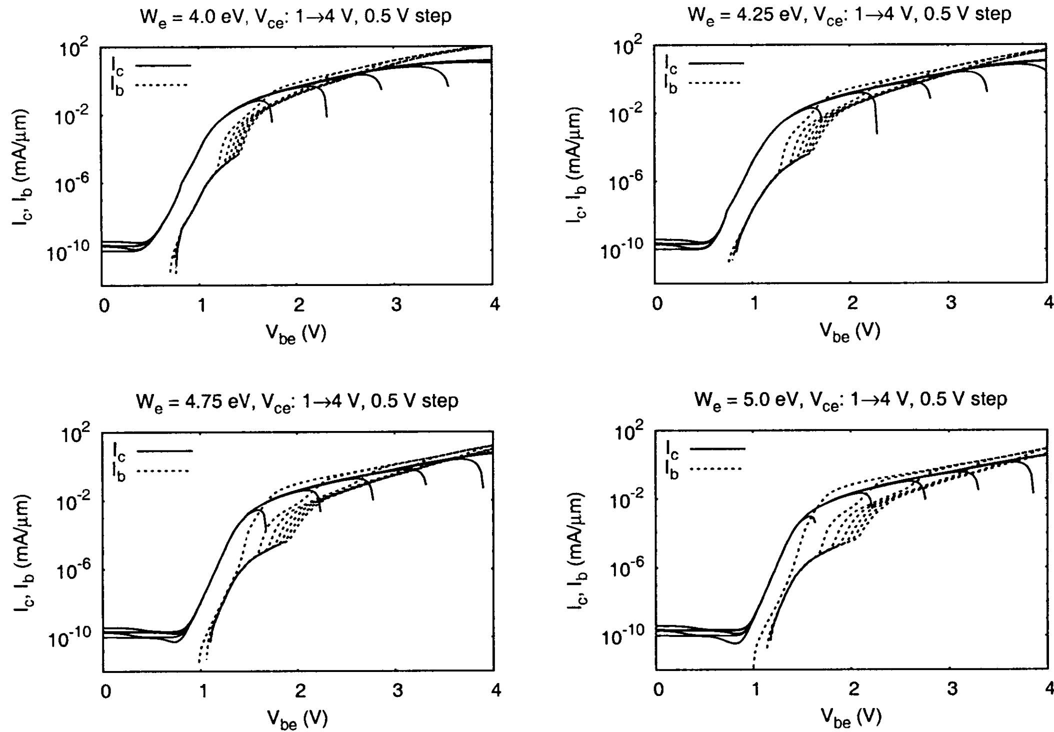

Figure 2-1: Gummel plots for four different emitter work functions EM_{WF}. The tunnel barrier affinity is 3.0 V and the tunnel barrier width is 20 Å. The drop in I_c and corresponding increase in I_b results from the base-collector junction becoming forward biased.

emitter work function is mainly on the obtained current level, with comparable effect on the collector and base current, and therefore with minimal influence on the current gain, given by the ratio of the two, see Eq. (8.4). Lower work function implies that electrons more readily tunnel into the base conduction band however, since less base-emitter bias is needed to pull the conduction band below that of the Fermi energy

of the metal. The fact that the transistor works for varying emitter work functions is important in light of the fact that ferromagnets will be used as the emitter whose work function therefore will not limit the device performance.

The increase in base current observable in Fig. 2-1 is explained next, in Sec. 2.2.

2.2 Effect of tunnel barrier height

The affinity of the dielectric which will determine the tunnel barrier height, will in general deviate from its ideal value because of defects and imperfections. In addition, it may vary across the tunnel barrier area in which case the resulting tunnel barrier height will be an average value. To investigate how the (average) tunnel barrier height affects the transistor action, simulations with various dielectric affinities have been performed. The emitter work function will be kept fixed at 4.5 eV. Consider the Gummel plots shown in Fig. 2-2. It is seen in Fig. 2-2 that above a certain base-emitter voltage the base current increases dramatically. This can be explained by looking at the band-alignment, carrier density, and electron and hole currents for different base-emitter biases, as shown in Fig. 2-3. The appearance of a significant base current above a certain base-emitter threshold voltage is apparent from Fig. 2-3. In fact, so much current is flowing that the band bending of the silicon becomes negligible. This is a manifestation of the Kirk effect in which the buildup of charge inside the base, associated with the high current densities, effectively pushes the depletion region into the collector. The onset of the effect is then determined by the minority current density which is confirmed by examining the current levels for a different tunnel barrier height, as in Fig. 2-4. Since the electron current levels obtained just before the increases in base current are comparable for Figs. 2-3 and 2-4, it is indeed the current level that determines the base push out in which the charge associated with the collector current becomes larger than the charge of the ionized donors over a finite region of the collector. This effectively increases the width of the base leading to additional losses and an increase in base current, as reflected in a distinctive knee in the base current Gummel plot of Fig. 2-2. The tunnel barrier

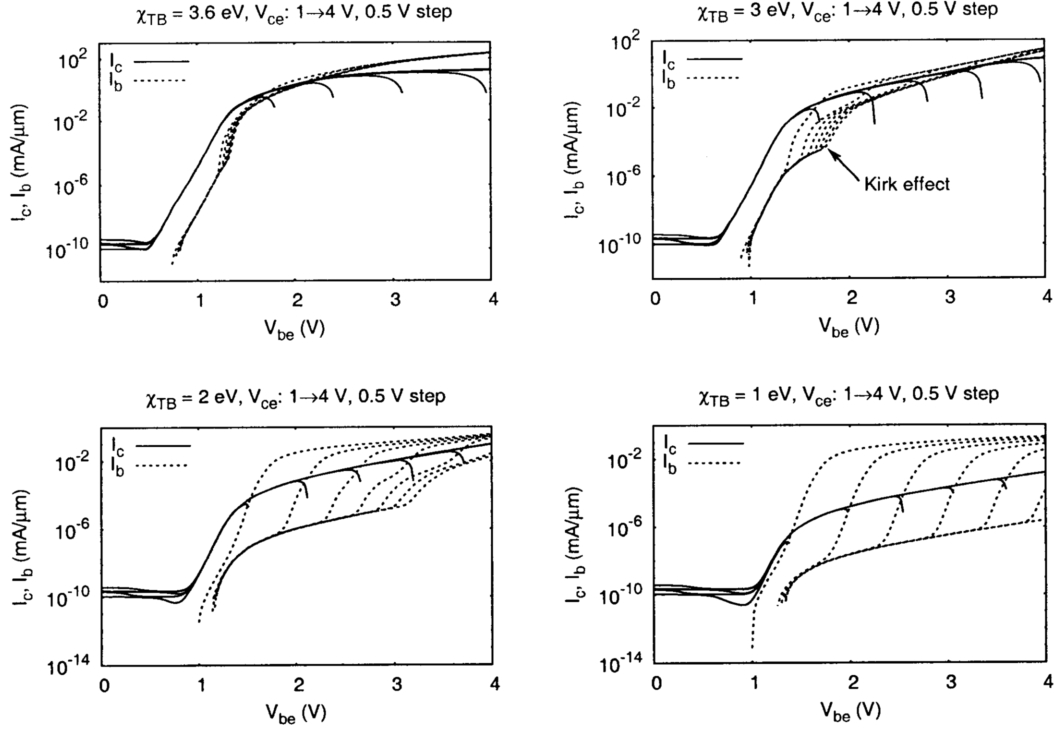

Figure 2-2: Gummel plots for several tunnel barrier affinities, left to right, top to bottom: 3.6 V, 3.0 V, 2.0 V, 1.0 V. The emitter work function is for all 4.5 eV. The tunnel barrier width is 20 Å. In the upper right picture is indicated the onset of an increase in base current, caused by the Kirk effect.

height then merely determines for which base-emitter voltages the onset begins since it influences directly the tunneling current. The change in effective base width is also seen from the electric field, plotted in Fig. 2-5 below and above the onset of the Kirk effect, demonstrating that the dipole of the base-collector junction moves into the collector for high-level injection.

The Kirk effect depends strongly on the collector doping concentration. This is illustrated in Fig. 2-6 which shows two Gummel plots with different collector doping. Below the high base current knee the transistor has a significant gain, largely independent of the exact current levels, as shown in Fig. 2-9 further below. The evolution of the collector current and gain over a wide range of base currents is shown in Appendix B.4. All in all, it can be concluded that the tunnel barrier determines

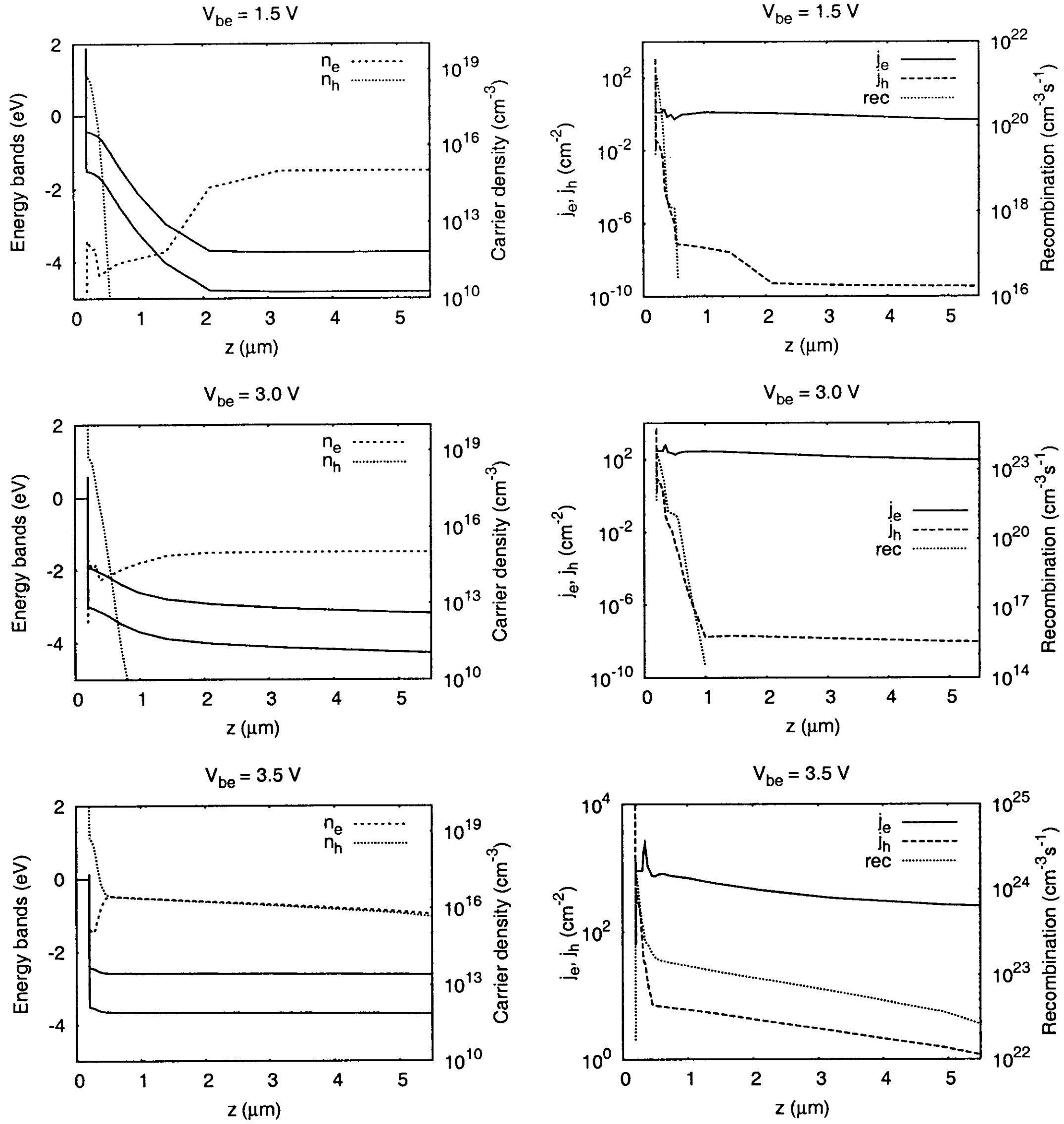

Figure 2-3: The left column depicts the bandstructure and carrier density, the right the electron, and hole currents and recombination. From top to bottom the base-emitter voltages are $V_{be} = 1.5$ V, $V_{be} = 3.0$ V, $V_{be} = 3.5$ V. The bottom row shows that for large I_c, the energy bands flatten out pushing the base-collector junction into the collector. The collector-emitter voltage $V_{ce} = 4.0$ V, the dielectric affinity is 2.0 V. The tunnel barrier width is 20 Å.

for which bias the Kirk effect sets in and that a tunnel barrier with a reasonable height will make the transistor more controllable over a range of bias voltages. The current levels obtained are then limited by the collector doping, but still significant

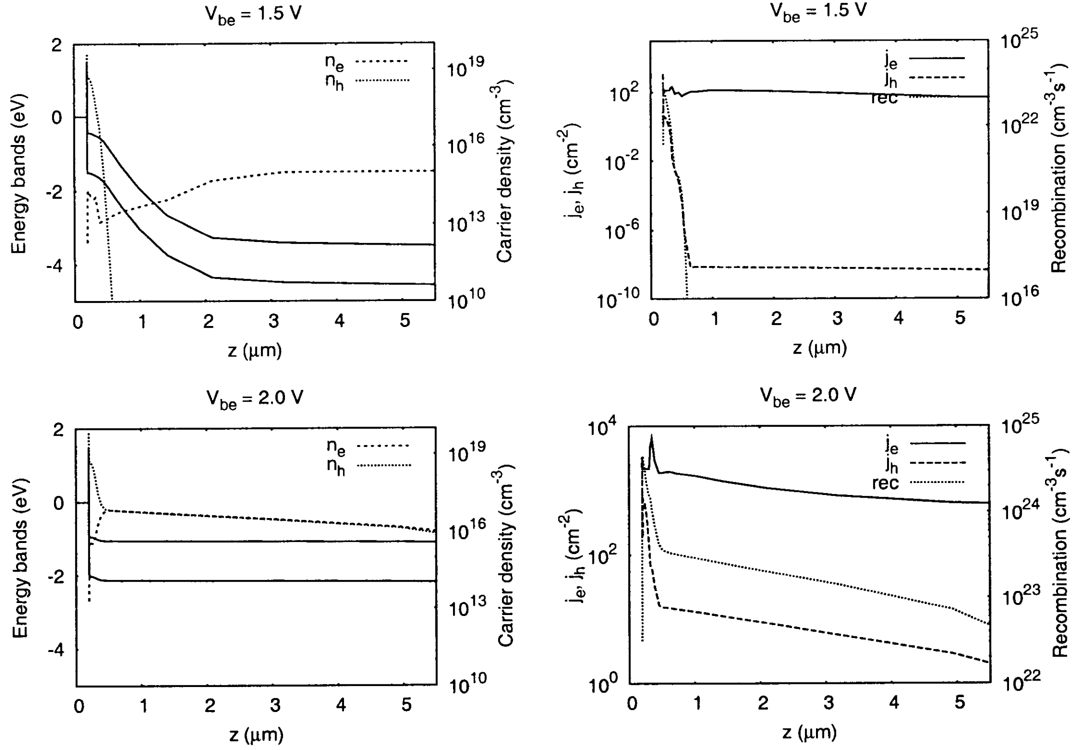

Figure 2-4: The left column depicts the band structure and carrier density, the right the electron, and hole currents and recombination. From top to bottom the base-emitter voltages are $V_{be} = 1.5$ V, and $V_{be} = 2.0$ V. The collector-emitter voltage $V_{ce} = 4.0$ V, the dielectric affinity is 3.0 V. The tunnel barrier width is 20 Å.

taking the 2-dimensionality and the small contact areas of the simulated device into account. The ultimate gain in the low base-current regime is then independent of the tunnel barrier height.

2.3 Setting the base voltage instead of base current

The home-built curve tracer, see Appendix C.6, developed to measure the implanted base transistors, can capture the response over 6 decades of base currents. The measurement setup used to analyze the epiwafer transistors however, used a voltage source to control the base *voltage* instead of current. This changes qualitatively the

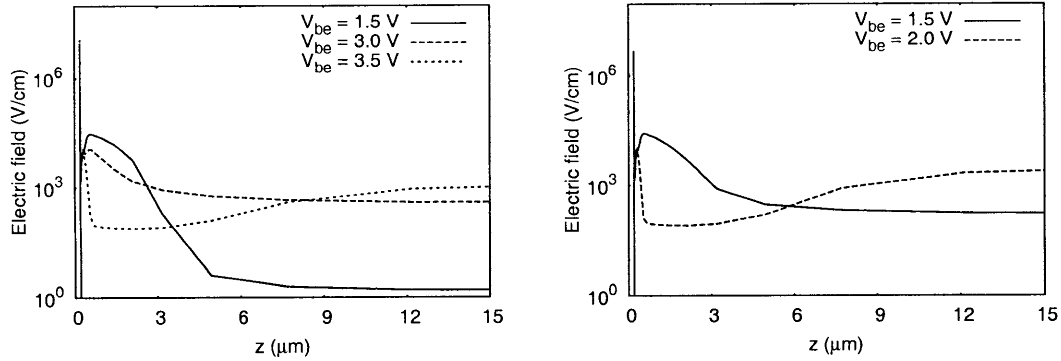

Figure 2-5: Electric field distribution below and above the high-level injection onset. The left corresponds to Fig. 2-3 with dielectric affinity 2.0 V, the right corresponds to Fig. 2-4 with dielectric affinity 3.0 V. The tunnel barrier width is 20 Å.

obtained transistor action plots as shown for instance in Fig. 2-7. It is apparent from Fig. 2-7 that the voltage drop across the tunnel barrier (and base) shows up as an offset in V_{ce} for increasing V_{be}. Obviously, for thicker or higher tunnel barriers the offsets become more pronounced.

2.4 Effect of tunnel barrier width

The tunneling current is sensitively dependent on the width of the tunnel barrier. In order to demonstrate that, the Gummel plots for a 40 Å thick barrier have been simulated, for various tunnel barrier heights, and are shown in Fig. 2-8. The results for the thick barrier shown in Fig. 2-8 should be contrasted with those for a thin barrier, i.e. Fig. 2-2. Because of the thicker barrier, more of the collector-emitter voltage drops across the barrier which does not contribute to reverse-biasing the collector-base junction. Consequently, the base-collector junction becomes more easily forward biased, reflected in the dramatic increase in base current for low base-emitter voltages. The thicker barrier requires as well a larger base-emitter voltage to induce a reasonable collector current. Qualitatively though, the results for a thick and thin barrier are comparable. The main difference is in the required larger voltage levels for the thick barrier which makes the device more difficult to handle; higher voltage

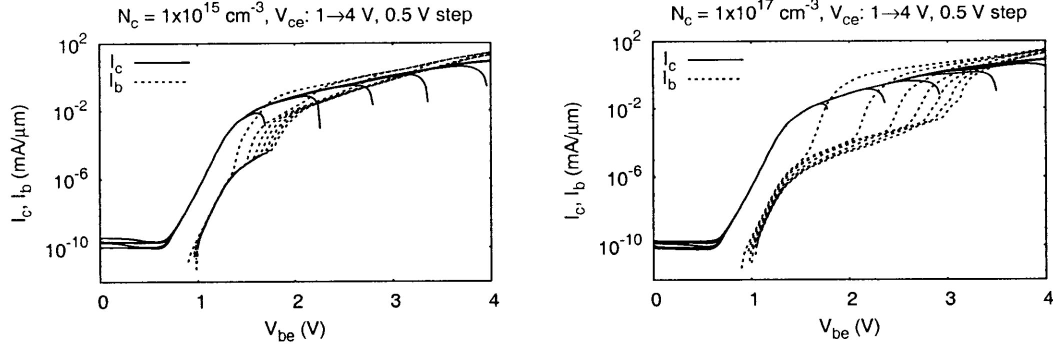

Figure 2-6: Gummel plots for 2 different collector doping concentrations: 1×10^{15} cm^{-3} (left, same as top right of Fig. 2-2) and 1×10^{17} cm^{-3} (right). The emitter work function is for both 4.5 eV and the dielectric affinity is 3.0 V. The tunnel barrier width is 20 Å.

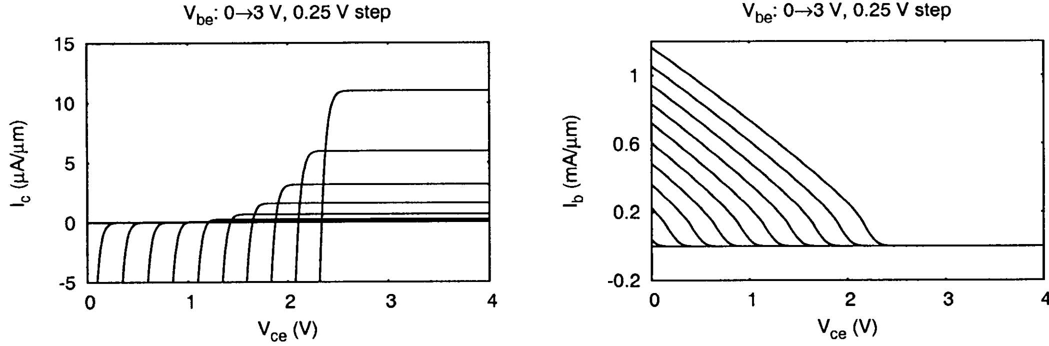

Figure 2-7: On the left is shown the collector current, and on the right the base current. The dielectric affinity is 2.0 V. The tunnel barrier width is 20 Å.

levels may cause breakdown of the tunnel barrier[1].

2.5 Effect of base doping

As described in Appendix A, three different base doping profiles were obtained by implanting through different oxide thicknesses. Here the influence of the doping on

[1]Although the tunnel barrier breakdown voltage is higher for thicker barriers, it is not expected that the tunnel barrier is everywhere evenly thick. Hence locally at thin regions voltages larger than the breakdown voltage may appear. This is especially relevant for thicker barriers since the currents will be more concentrated at local hotspots.

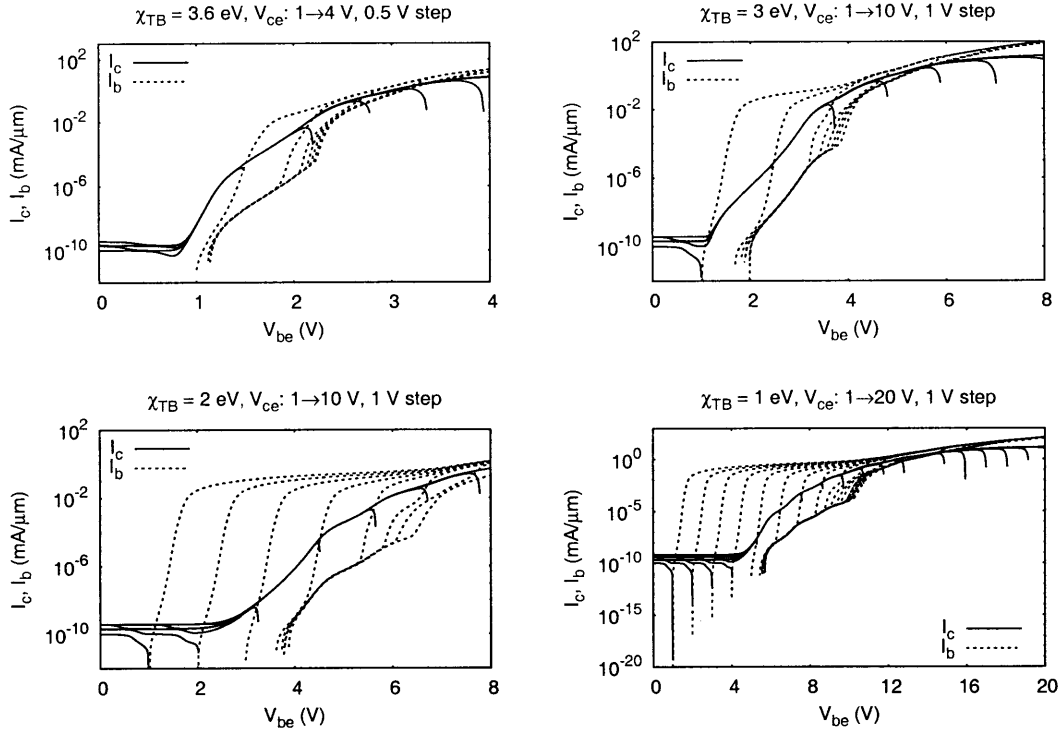

Figure 2-8: Gummel plots for several tunnel barrier affinities, left to right, top to bottom: 3.6 V, 3.0 V, 2.0 V, 1.0 V. The emitter work function is for all 4.5 eV. The tunnel barrier width is 40 Å.

the current gain will be discussed. In Fig. 2-9 are shown the collector current and current gain for the three different concentrations. It can be seen from Fig. 2-9 that the gain is significantly higher for the shallow base transistor. This results from an increase in base transport factor, Eq. (8.2), i.e. a reduction in recombination inside the base. For ordinary bipolar transistors the doping concentration of the base has a direct effect on the current gain, as explained in Sec. 8.1, but this fails to hold for tunneling emitter bipolar transistors, as described in Sec. 8.2. Reducing the base doping concentration merely reduces the base width, see Fig. A-2, yielding less recombination inside the base. Another effect is the variation of I_c with V_{ce}, as evident from Fig. 2-9. This stems from base-width modulation; the base becomes increasingly narrow for rising V_{ce}. This will increase the collector current and the gain. The slopes of the I_c curves intersect at a common point on the V_{ce} axis; this point defines the

Early voltage V_{early}. A small V_{early} therefore reflects little recombination inside the base but has as disadvantage that I_c is sensitively dependent on V_{ce}.

In this Chapter the influence of the various components of the tunneling emitter bipolar transistor on the transistor characteristics was considered. It was found that changes in emitter work function, and tunnel barrier width and height, will only affect the voltage levels for which the transistor enters the active region or is subject to high-level injection conditions but will not for instance limit the current gain that can be obtained. The ultimate gain of the transistor is determined by the base doping concentration. Here it was assumed though that the tunnel barrier behaves perfectly, as described in Appendix B. The role of the tunnel barrier in the working of the transistor and the effects of non-idealities of the tunnel barrier are described in Chapter 8.

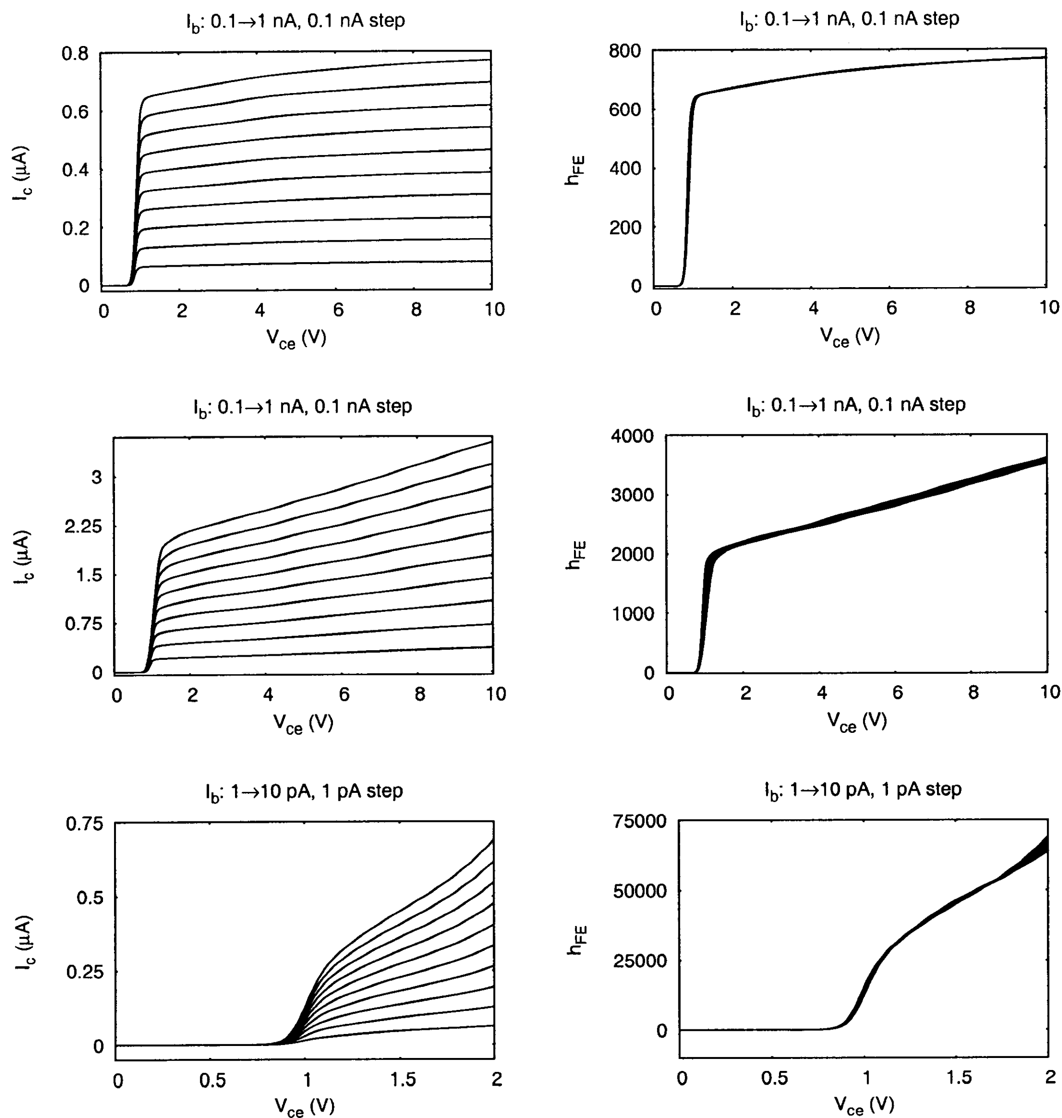

Figure 2-9: Transistor plots for low base currents for the three different ion implanted bases given in Fig. A-2. The left column gives the collector current I_c, and the right column the current gain. The implant oxide thickness for the top, middle, and bottom row are 120 nm, 146 nm, 180 nm, respectively. The dielectric affinity is 3.0 V. The tunnel barrier width is 20 Å.

Chapter 3

Spin transport through a PN junction

For the spin injecting tunneling emitter bipolar transistor to work, it is necessary to consider what happens to the electron spin while traversing the PN junction. This Chapter will discuss the results of a computer simulation modelling spin transport through PN-junctions[1].

3.1 Theory of spin in PN junctions

The theory of spin polarized transport through the depletion layer of PN junctions has been fully developed[65]. Various types of PN junctions have been considered; with a magnetic P-layer or N-layer[70], or both nonmagnetic[64, 71]. It is the latter that will be considered here; the source spin is then assumed to be introduced by external means at the edge of the P-layer. This configuration has been simulated in [64] for GaAs. Here the simulation results for silicon are presented. The major difference between the two materials is the generation-recombination term which for silicon is given by the Shockley-Read-Hall mechanism, i.e. recombination via a deep-level defect state. The defining equations are then given by

[1]The computer simulation has been written by Nicolas Locatelli.

Poisson's equation:

$$\frac{d^2V}{dz^2} = -\frac{\rho}{\epsilon_r\epsilon_0}$$
$$\rho = e(N_D - N_A - n + p) \tag{3.1}$$

Drift-diffusion equation:

$$J_{n\uparrow} = en_\uparrow \mu_n E + eD_n \frac{dn_\uparrow}{dz}$$
$$J_{n\downarrow} = en_\downarrow \mu_n E + eD_n \frac{dn_\downarrow}{dz} \tag{3.2}$$
$$J_p = ep\mu_p E - eD_p \frac{dp}{dz}$$

Continuity equation:

$$\frac{dn_\uparrow}{dt} = -\frac{n_\uparrow p - n_i^2/2}{\tau_n(n+n_i) + \tau_p(p+n_i)} - \frac{n_\uparrow - n_\downarrow}{2T_s} + \frac{1}{e}\frac{dJ_{n\uparrow}}{dz}$$
$$\frac{dn_\downarrow}{dt} = -\frac{n_\downarrow p - n_i^2/2}{\tau_n(n+n_i) + \tau_p(p+n_i)} - \frac{n_\downarrow - n_\uparrow}{2T_s} + \frac{1}{e}\frac{dJ_{n\downarrow}}{dz} \tag{3.3}$$
$$\frac{dp}{dt} = -\frac{np - n_i^2/2}{\tau_n(n+n_i) + \tau_p(p+n_i)} - \frac{1}{e}\frac{dJ_p}{dz}$$

This set of equations is numerically solved in steady-state with as boundary conditions a spin-polarized contact on the left and an ohmic, unpolarized contact on the right, as shown in Fig. 3-1. A bias voltage V_{cb} between the contacts is incorporated using Gummel's method. The results of the simulation are presented in Sec. 3.2.

3.2 Simulation results

The PN junction will be modeled as abrupt with the hole doped region on the left with uniform concentration 2×10^{15} cm^{-3} and the electron doped region on the right with uniform concentration 1×10^{15} cm^{-3}. These correspond approximately to the measured PN epiwafer parameters. The P-region is chosen to be 1 μm long, and the N-region extends 20 μm. For zero applied bias the charge, electric field, and potential are given by Fig. 3-2. As observable in Fig. 3-2, on the left end of the P-region is introduced a non-equilibrium concentration of electrons of $\delta n = 1 \times 10^{14}$ cm^{-3}. These

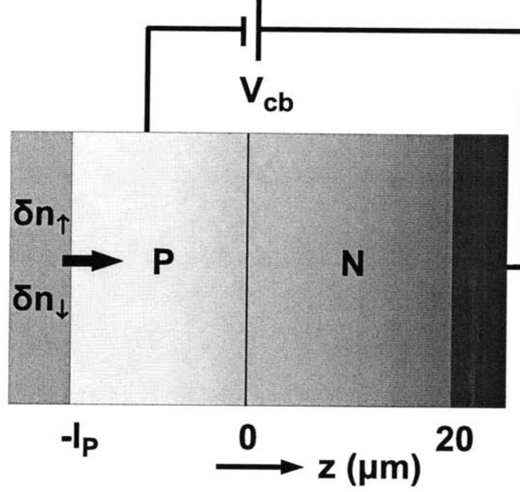

Figure 3-1: Schematic of PN junction subject to spin-injection. On the very left end of the P-region is introduced a non-equilibrium spin-polarized charge density. The simulation will evaluate what happens to this spin-density across the PN junction until it reaches the ohmic, unpolarized contact on the right end of the N-region. An additional collector-base voltage V_{cb} can be applied that enhances the depletion region of the PN junction.

electrons are spin polarized according to

$$\begin{aligned} &\alpha = 0.5 \Rightarrow \\ &\delta n_{\uparrow} = 7.5 \times 10^{13}\ \text{cm}^{-3} \\ &\delta n_{\downarrow} = 2.5 \times 10^{13}\ \text{cm}^{-3} \end{aligned} \tag{3.4}$$

with α the carrier spin-polarization. The charge inbalance corresponds to a current density of

$$J = \delta nev \approx 10\ \text{A/cm}^2 \tag{3.5}$$

which is a realistic value for this structure. The spin distribution across the PN junction is plotted in Fig. 3-3. From Fig. 3-3 it is observed that the carrier polarization stays (approximately) constant inside the P-region. This is because the exponential decay is negligible considering the short length, whereas recombination does not affect spin-polarization in the P-region (only) since it is the ratio of carriers that matters. Across the depletion region of the PN junction the carrier polarization

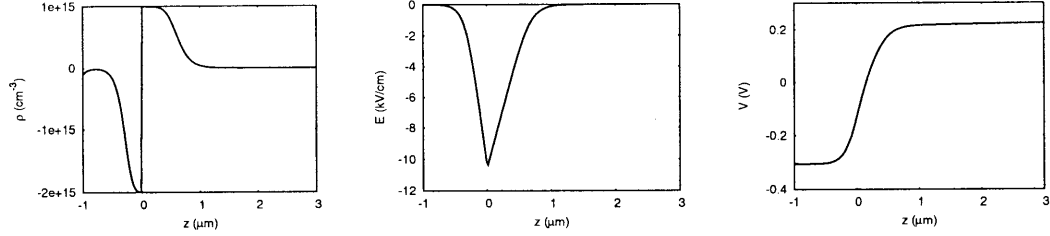

Figure 3-2: PN junction under zero bias. On the left the charge density, in the middle the electric field, and on the right the potential. At the left end of the P-region are introduced 1×10^{14} cm^{-3} electrons.

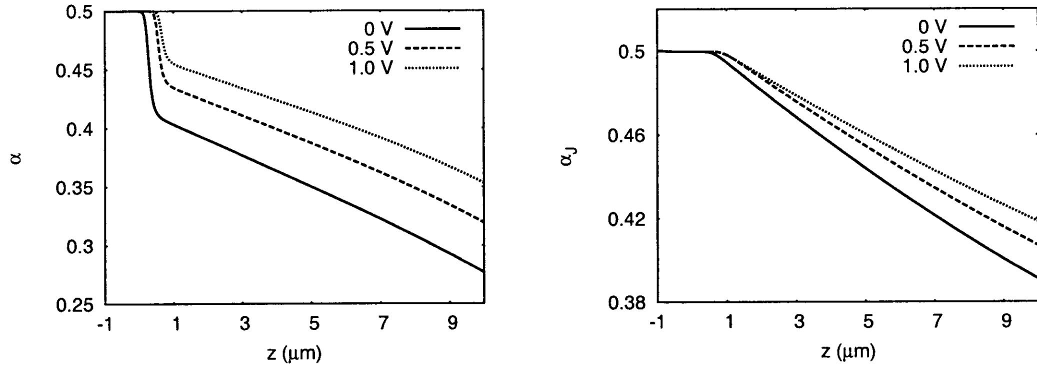

Figure 3-3: Spin transport through the PN junction for various bias voltages V_{cb}. On the left is plotted the carrier polarization, and on the right the current polarization.

drops. This results from the fact that the spin-polarized electrons originating from the P-region will be only a small part of all the majority electrons inside the N-region. Recombination inside the P-region will therefore directly affect the spin-polarization inside the N-region, yielding a bigger drop for larger recombination. Notice that the drop occurs at the edge of the depletion region and not at the abrupt PN junction because of the carrier depletion inside the depletion region. Furhter away from the depletion region, the carrier polarization decays exponentially by spin-decoherence. Also shown in Fig. 3-3 is the current polarization α_J. The current polarization stays approximately constant across the depletion region and decays much slower inside the N-region, clearly a result of the drift.

If the PN junction is reverse biased, the carrier and current polarization within the N-region increase. The bias will increase the width of the depletion region which will

reduce the recombination inside the P-region. It is also interesting to consider the effect of longer P-region lengths. This is shown in Fig. 3-4. For longer P-region

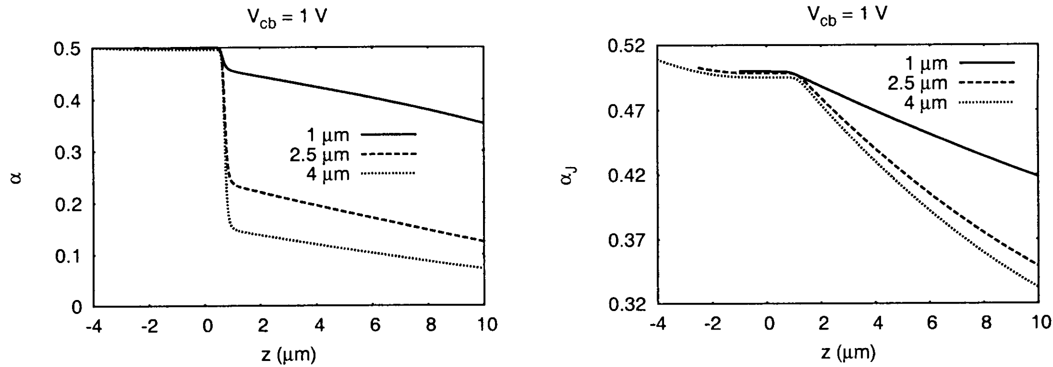

Figure 3-4: Spin transport through the PN junction for various P-region lengths l_P. On the left is given the carrier polarization, and on the right the current polarization. The abrupt PN junction is for each case located at $z = 0$.

lengths, the carrier and current polarization inside the N-region decrease rapidly, as reflected in Fig. 3-4. Again, the recombination inside the P-region lies at the origin. In Sec. A.2 it was shown that for the second generation transistors bases with varying doping concentration were fabricated and it is interesting to see what its effect on the spin-transfer across the base-collector PN junction is. Because a graded base doping is not incorporated in the model, the base doping is increased uniformly. The results are shown in Fig. 3-5. For increasing doping concentrations the drop in α across the PN junction increases. However, it quickly converges with only little increase in drop for even higher doping. The drop stems from recombination inside the base; for low base doping the base width outside the depletion region is small. Increasing the doping will increase the effective base width experienced but this will saturate quickly with most of the depletion happening inside the N-region. Consequently, the Gummel number of the base, as given in Fig. A-2, does not directly influence the spin transport across the base-collector junction.

Another interesting effect can be seen in Fig. 3-6. In Fig. 3-6 is plotted the spin density $n_\uparrow - n_\downarrow$. Interestingly, the spin density is larger in the N-region than at the point of injection (very left of P-region, also Eq. (3.4)). This was also observed in

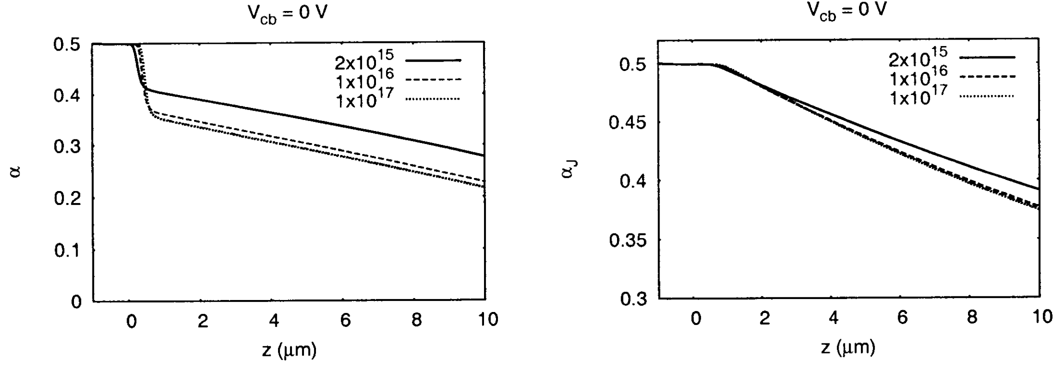

Figure 3-5: Spin transport through PN junction for various P-region doping (in units cm^{-3}). On the left the carrier polarization, and on the right the current polarization. The abrupt PN junction is in each case located at $z = 0$. The simulation is performed for zero applied bias across the PN junction.

GaAs PN junctions in [64] and dubbed "spin pumping through the minority channel". It results from the spin being injected faster than it can decay (with time constant τ_s, here 1×10^{-7} s).

In conclusion, the simulations predict that spin can be transported very efficiently through the depletion region of a silicon PN junction. Any electron spin introduced in the P-region will polarize the N-region. This is a validation of using a PN junction to inject electron spin into silicon. The challenge is now reduced to introducing source spins into the P-region.

It remains to be noticed that also theory describing spin-transport in bipolar transistors has been developed for devices with a magnetic region[72][73] or with all regions nonmagnetic semiconductor[68]. The tunnel emitter transistor however does not fit into these categories; its working is closer to that of a nonmagnetic PN junction with a source spin at the edge of the P-region.

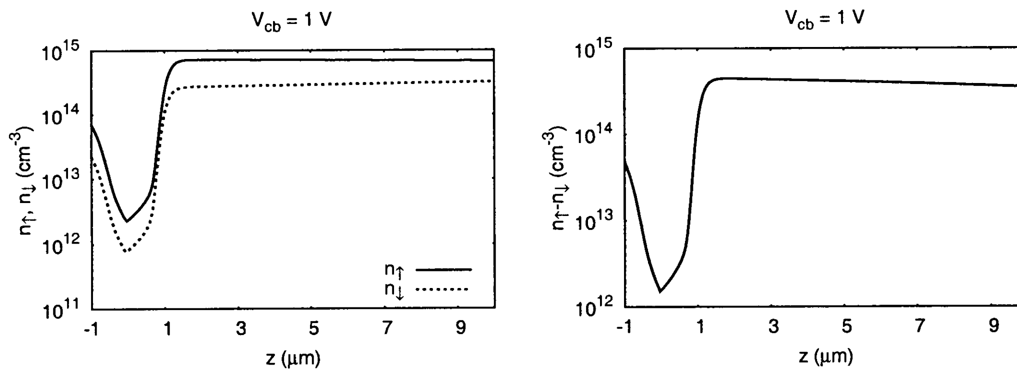

Figure 3-6: Spin resolved carrier concentration (left) and spin density (right) across the PN junction. The curve in the right plot is the difference of the two curves shown in the left figure. The applied bias to the P-region is -1 V.

Chapter 4

The growth of MgO on silicon

The tunnel barrier MgO, in conjunction with bcc iron, will act as a spin filter if it is epitaxial in the (100) direction with Fe. This feature makes MgO an attractive choice as a tunnel barrier for the tunneling emitter bipolar transistor. In this Chapter some background information about MgO will be given and a study of the growth of MgO on silicon will be discussed, which appeared in [74].

4.1 Band structure of MgO

The crystal structures of Fe, MgO, and silicon are shown in Fig. 4-1. MgO forms a rock salt structure with both the magnesium and oxygen arranged in FCC lattices, mutually displaced by half an atomic distance. Iron crystallizes under normal conditions into the BCC form. Silicon has a tetragonal structure which is formed by two interpenetrating FCC lattices, displaced by a quarter of the body diagonal. The tetragonal structure has an inversion center (at 1/8 of the body diagonal) hence the Dresselhaus spin-orbit interaction is absent in silicon.

The lattice constants of the three materials are

$$\begin{aligned} d_{\mathrm{Fe}} &= 2.866\ \text{Å} \\ d_{\mathrm{MgO}} &= 4.212\ \text{Å} \\ d_{\mathrm{Si}} &= 5.431\ \text{Å}. \end{aligned} \tag{4.1}$$

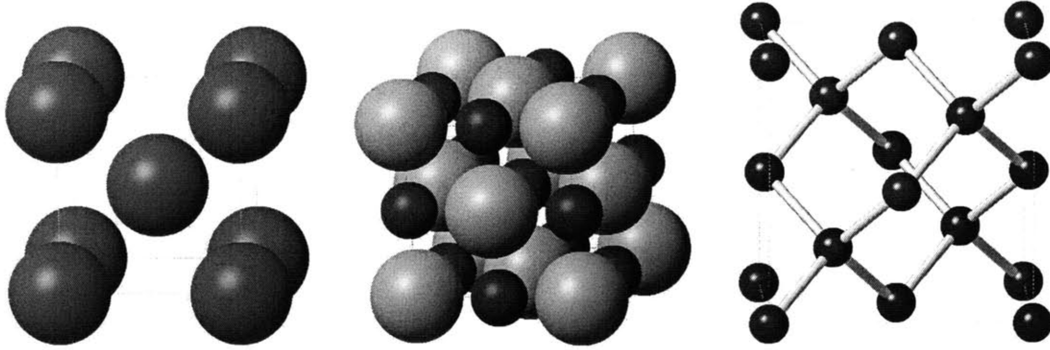

Figure 4-1: Crystal structure of BCC Fe (left), rock salt MgO (middle, small spheres are Mg), and tetragonal Si (right). The structures have been generated with crystalmaker[75].

Since MgO is an insulator, it has an energy gap which is approximately 7.6 eV. For bulk MgO, the dispersion relation has no solutions inside the energy gap. However, near the surface, solutions within the energy gap are allowed. Those MgO states have complex wavevectors and form evanescent waves confined to the surface, i.e. the states decay exponentially within the MgO bulk. The states form a so-called complex band structure with wave vectors that are complex. These energy bands extend between the valence and conduction band. The wavevectors can be split into a part perpendicular to the surface $\boldsymbol{k}_{\perp}$ and a part parallel to the surface $\boldsymbol{k}_{\parallel}$. The perpendicular part determines the decay within in the bulk whereas the parallel part determines the symmetries the Bloch state can take. Different symmetries are only preserved when the MgO is crystalline.

If MgO is now sandwiched by two Fe electrodes, then electrons from the electrodes will tunnel through the MgO via a complex band. The symmetry of the wave function is conserved during the tunneling, therefore electrons from the Fe with a certain symmetry will need to tunnel via a band in the MgO with the same symmetry. Different bands in the MgO have different decay rates however hence the symmetry of the wavefunction influences directly the tunneling probability. The decay rates inside the MgO for four different symmetries are shown in Fig. 4-2. In the (100) direction, and for $\boldsymbol{k}_{\parallel} = 0$, Fe has different Bloch state symmetries for majority and minority

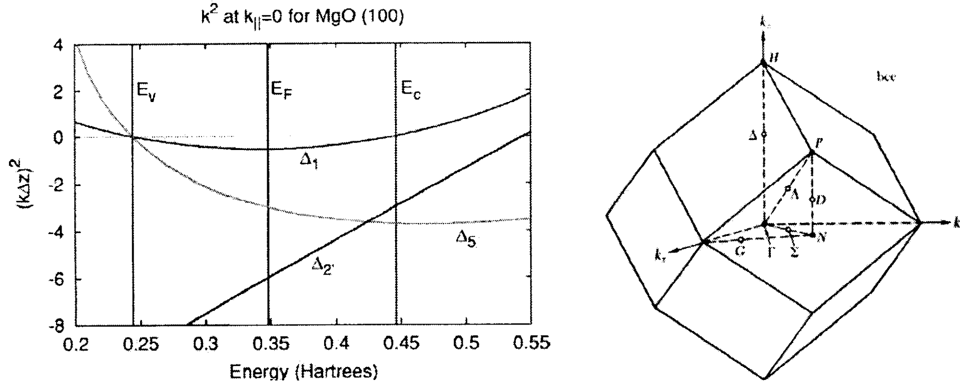

Figure 4-2: Adapted from [8] (left) and [76] (right). Decay rates inside MgO for four different wave function symmetries are shown on the left for in-plane wave vector $\boldsymbol{k}_{\|} = 0$. The right shows the Brillouin zone with symmetry axes for a BCC lattice.

spin. The majority spin has symmetries Δ_1, Δ_5, Δ_2' whereas the minority spin has Δ_2, Δ_5, Δ_2', hence the minority spin is missing the slowly decaying Δ_1 symmetry of Fig. 4-2. This is then translated into a slow decay rate for majority spins compared to a much more rapid decay for minority spins as depicted in Fig. 4-3. Because of the

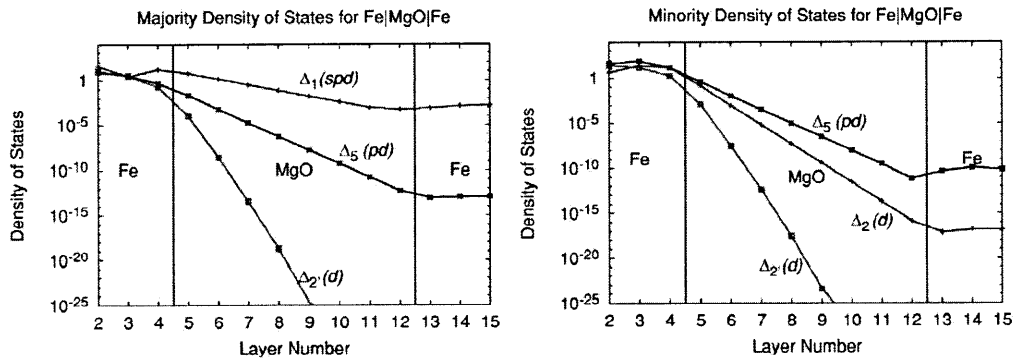

Figure 4-3: Adapted from [8]. Tunneling density of states of parallel Fe/MgO/Fe illustrating the slow decay of majority spins (left) and the rapid decay of minority spins (right). The in-plane wave vector $\boldsymbol{k}_{\|} = 0$.

different decay rates, the spin-polarization of Fe is amplified by the tunneling process yielding an effective spin-filter. In Figs. 4-2 and 4-3 only $k_{\|} = 0$ is considered. This is valid because most of the majority conductance happens via this point in k-space because of the presence of a Δ_1 band and a large majority spin density of states.

Minority spins will preferentially tunnel via states away from the Γ-point, with a Δ_5 symmetry, because of the near-absence of density of states at the Γ-point.

Magnetic tunnel junctions made out of Fe/MgO/Fe stacks exhibit a very large magnetoresistance, that is, a large difference in resistance between parallel and anti-parallel configuration. This can be understood by considering the tunneling DOS for anti-parallel alignment of the ferromagnets given in Fig. 4-4. Although majority spins can

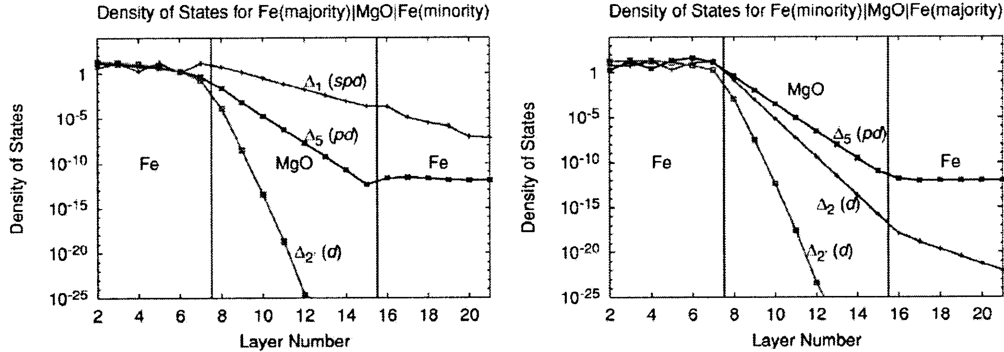

Figure 4-4: Adapted from [8]. Tunneling density of states of anti-parallel Fe/MgO/Fe. Both the majority and minority spins now tunnel preferentially via the Δ_5 band. The in-plane wave vector $\boldsymbol{k}_{\|} = 0$.

still tunnel inside the MgO via the Δ_1 band, this band is lacking in the Fe electrode on the opposite end. Hence the spins in this band would continue to decay inside that electrode yielding a total reflection of states with the Δ_1 symmetry. On the other hand, the Δ_5 symmetry band is present in both electrodes hence spins (majority and minority) will tunnel preferentially via this band. The difference in decay of the Δ_1 band and Δ_5 band then determines the magnetoresistance difference for parallel and anti-parallel alignment of the Fe electrodes.

4.2 Fe/MgO on silicon

When one of the Fe electrodes is replaced with silicon, it is necessary to consider what will happen with the symmetry of the wave function. The band structure of silicon is given in Fig. 4-5. Silicon has an indirect bandgap with the minimum of the

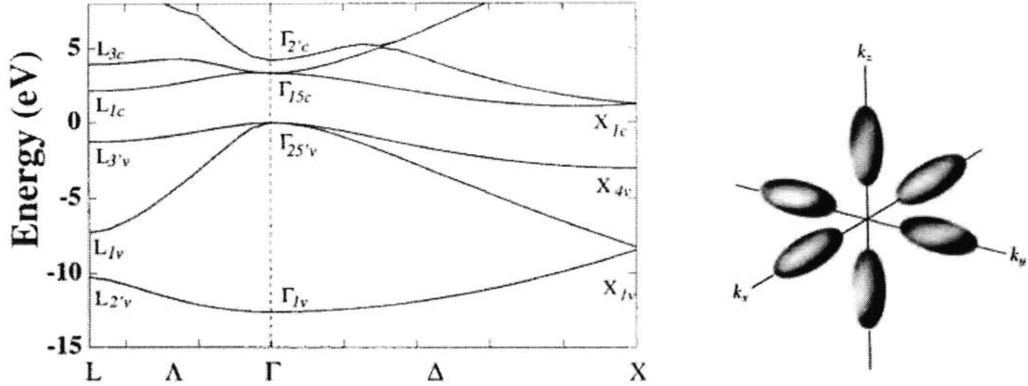

Figure 4-5: Adapted from [77] (left) and [76] (right). The left image shows the band structure of silicon with wave function symmetries indicated. The right depicts the conduction electron pockets.

conduction band along the Δ direction, 85% away from Γ towards X. The conduction band directly above the valence band maximum at the Γ-point is approximately 2 eV higher. In [78] spin-coherent *tunneling* through silicon was studied for an Fe/Si/Fe system, i.e. the electrons have an energy that is located within the band gap. For that system it was found that for tunnel electron energies close enough to the valence band the tunneling happens predominantly with $k_{\|} = 0$ via a Δ_1 band. However, if the tunnel electron energy is within 0.35 eV of the conduction band minimum, then tunneling happens away from the Γ-point with $k_{\|}$ that of the conduction band minimum. This would have consequences for the spin-filtering since away from the Γ-point the Δ_1 band decays much faster.

For the tunnel emitter transistor, the electrons will tunnel directly into the conduction band minimum along the Δ direction. The conduction band minimum consists of 6 cigar-shaped pockets shown in Fig. 4-5. Those electrons have the Δ_1 symmetry [79] and a nonzero wave vector. The symmetry is compatible with that of the majority spins of Fe. Since however most of the tunneling is concentrated around the Γ-point for the in-plane wave vector of Fe, the perpendicular wave vector should provide the value of the location of the conduction band minimum of silicon. This may be possible since there are electron pockets in any major direction and the electrons will have energies

above the band gap. The minority spins of Fe will predominantly tunnel via the Δ_5 band. Since the density of states of Fe for minority spin is concentrated away from the Γ point, now the non-zero wave vector for conduction electrons in silicon should be provided by the in-plane component, implying therefore that the perpendicular component is almost zero. This would imply that majority and minority spins end up in different pockets.

4.3 Epitaxial growth of MgO on silicon

The epitaxial growth of MgO on silicon is complicated by the large lattice mismatch between MgO and silicon which from Eq. (4.1) is about 3.4% for a 4 : 3 ratio of MgO:Si. It has been realized before using pulsed laser deposition [80] where the substrate temperature was raised to increase the interaction energy between silicon and MgO. In that work it was shown that the competition between surface energy and interface energy will determine the orientation of MgO; for lower substrate temperatures, the surface energy dominates and MgO will grow oriented in the (110) direction which yields the lowest surface energy. For much higher substrate temperatures, the MgO takes on the (111) direction since it yields the highest interaction energy. In between this temperature range, for T $\approx$ 450°C, the preferred direction turned out to be (100), a compromise between surface and interface energy minimization.
Here the growth of MgO using electron beam deposition in a UHV system will be discussed. The work comprises two parts, the demonstration of epitaxial growth of MgO on silicon and the proof that Fe/MgO/Fe MTJ's grown on silicon with an MgO buffer layer display coherent tunneling with accompanying large magnetoresistance. The fabrication is further discussed in [74]. The substrate is heated to 300°C, a necessary condition to obtain epitaxial growth. The TEM images of Fig. 4-6 show the crystallinity of MgO on silicon. From the TEM images Fig. 4-6 it is observed that regions of homogeneous epitaxial growth are interspersed with small angle grain boundaries, formed by the slight misorientation of neighboring regions. These grain boundaries give rise to diffraction patterns as shown on the left of Fig. 4-6. The

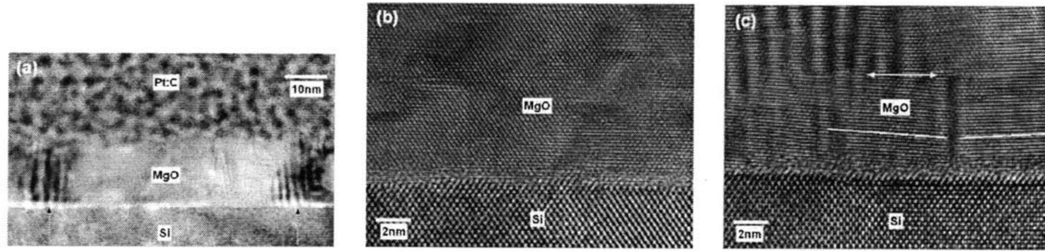

Figure 4-6: TEM images of epitaxial MgO on silicon. The left shows the occurrence of Moire patterns, the middle a region of homogeneous growth and the right the existence of small angle grain boundaries in the film.

lateral periodicity of the grain boundaries is approximately between $40 - 60$ nm. As observed in Fig. 4-6, the first couple of MgO layers are not oriented. This was also observed in [80] and attributed to the complete relaxation of the strain between MgO and silicon. Below however it is shown that for thin enough layers the MgO is still under tensile strain. The unresolved couple of monolayers may instead be the result of a thin surface oxide forming on the silicon before the actual start of the MgO deposition, or because of some intermixing between MgO and silicon.

The epitaxy of MgO is further demonstrated from the tunneling magnetoresistance (TMR) of MTJ's fabricated out of Fe/MgO/Fe stacks grown on a buffer layer of MgO on silicon. By varying the thickness of the buffer layer and observing the response in TMR, the quality of the buffer layer can be probed electrically. This is shown in Fig. 4-7. The TMR versus buffer layer thickness, Fig. 4-7, displays a maximum. Below the maximum the MgO thickness may not be enough to provide a good enough buffer against intermixing, whereas for increasing thicknesses, the tensile strain on the MgO will relax with the formation of dislocations and accompanying roughness. The development of the strain in the MTJ's can also be seen from XRD measurements on the MTJ's as given in Fig. 4-8. Clearly observed in Fig. 4-8 is that the MgO is initially under tensile strain but that the strain is relieved for increasing buffer thickness. The Fe in turn starts relaxed, a consequence of the small lattice mismatch of 0.5% with silicon, assuming a $4\sqrt{2} : 3$ ratio of Fe:Si[1]. Since the MgO expands for

[1]The $\sqrt{2}$ results from the 45° rotation of Fe with respect to MgO and Si.

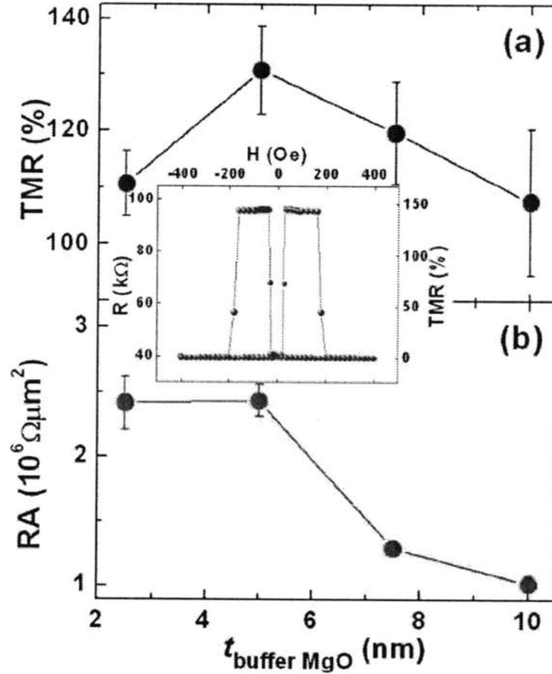

Figure 4-7: TMR of MTJ's grown on a buffer layer of varying thickness. The inset gives the magnetoresistance curve for a buffer layer thickness of 5 nm.

increasing buffer thicknesses, the Fe becomes more stressed under compressive strain. The relaxation of the MgO introduces interface roughness which translates through the MTJ stack, yielding a decrease in magnetoresistance.

In summary, Fe/MgO(100) can be grown epitaxially on silicon by ebeam evaporation. Growth conditions require that the substrate is heated to 300°C during growth which may complicate device fabrication. The MgO is under tensile strain, and if the MgO thickness is increased above 5 nm, it starts to relax introducing dislocations. It is uncertain whether the Fe/MgO on top of silicon acts as a spin-filter, considering the fact that the conduction band minimum of silicon is far away from the Γ-point.

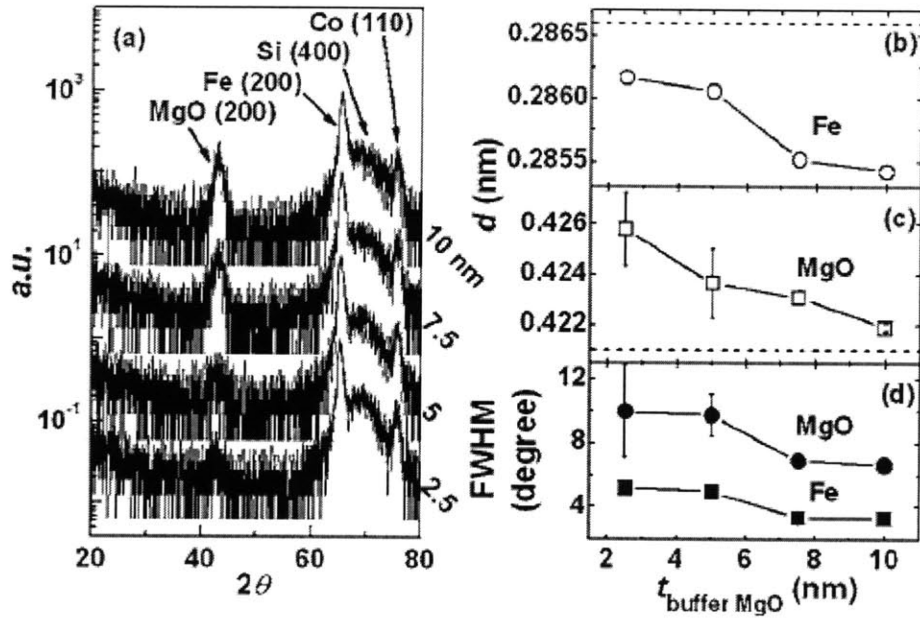

Figure 4-8: XRD of the MTJ's for different MgO buffer layer thicknesses. On the left is shown the $\theta - 2\theta$ scan (with θ offset by 2° to escape the narrow Si peak). The cobalt (110) peak results from the cobalt layer used to exchange bias the top Fe layer of the MTJ. On the right is given the derived out-of-plane lattice spacings of Fe (b) and MgO (c) with the dashed lines the lattice constant of bulk Fe and MgO. The bottom right (d) shows the rocking curve.

Chapter 5

Electron Spin Resonance as a probe to detect spin-injection

The tunneling emitter bipolar transistors described in this work have a perpendicular structure. This makes electrical spin-detection more difficult. A different way is to use Electron Spin Resonance (ESR) to detect the injected spin. ESR as a spin-detection scheme was first employed in [81] on EuO/InSb samples, and is particularly well suited for the tunneling emitter bipolar transistor because of the perpendicular structure of the samples. Hence ESR is analyzed in this Chapter as a potential measurement technique to probe the spin-polarization injected into the collector.

5.1 Electron Spin Resonance defined

ESR [82] is a measurement technique that exploits the Zeeman splitting of electron spins in a magnetic field to determine the spin-population. Consider Fig. 5-1. The static magnetic field creates an energy level splitting of the spins linearly proportional to the applied field. Importantly, the splitting in energy creates a spin-population inversion. If now an rf electromagnetic field is applied that is tuned to the level splitting, i.e. whose frequency matches the energy difference between the two spin directions, then there will be a net absorption of the rf field. The net absorption is directly proportional to the spin-population inbalance; an unpolarized ensemble

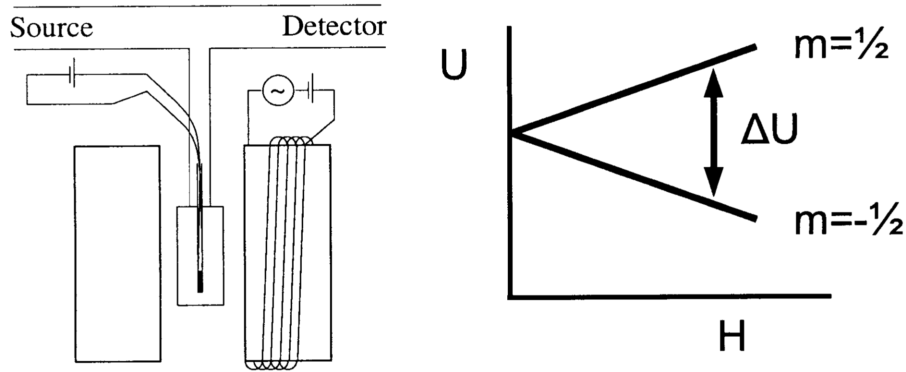

Figure 5-1: Schematics of ESR setup (left) and energy level splitting (right).

for instance would give equal amounts of absorption and emission and hence zero net absorption. In order for ESR to work, there need to be electron spins that are polarizable. For instance, the ESR signal of pure crystalline silicon would be zero[1] since all atoms have formed covalent bonds and the electron spins are interlocked and oppositely directed. Introducing donor dopants into the silicon however adds free conduction electrons to the system whose spins can orient along the applied magnetic field. The corresponding ESR signal is called conduction electron ESR. At low enough temperatures, the extra electrons from the donors are not excited to the conduction band but are bound to the donor atoms as dangling bonds. The spins of the dangling bonds are still free to align. Interestingly however, because of the promixity of these electrons with their mother nuclei, their spins couple to the nuclear spins of the donor atoms which gives rise to a hyperfine energy splitting. The influence of the transition of donor bound electrons to conduction electrons on the ESR signal is demonstrated in the measurements that were done on a piece of the PN epiwafer and shown in Fig. 5-2.

[1]There is a finite contribution from the edge of the sample.

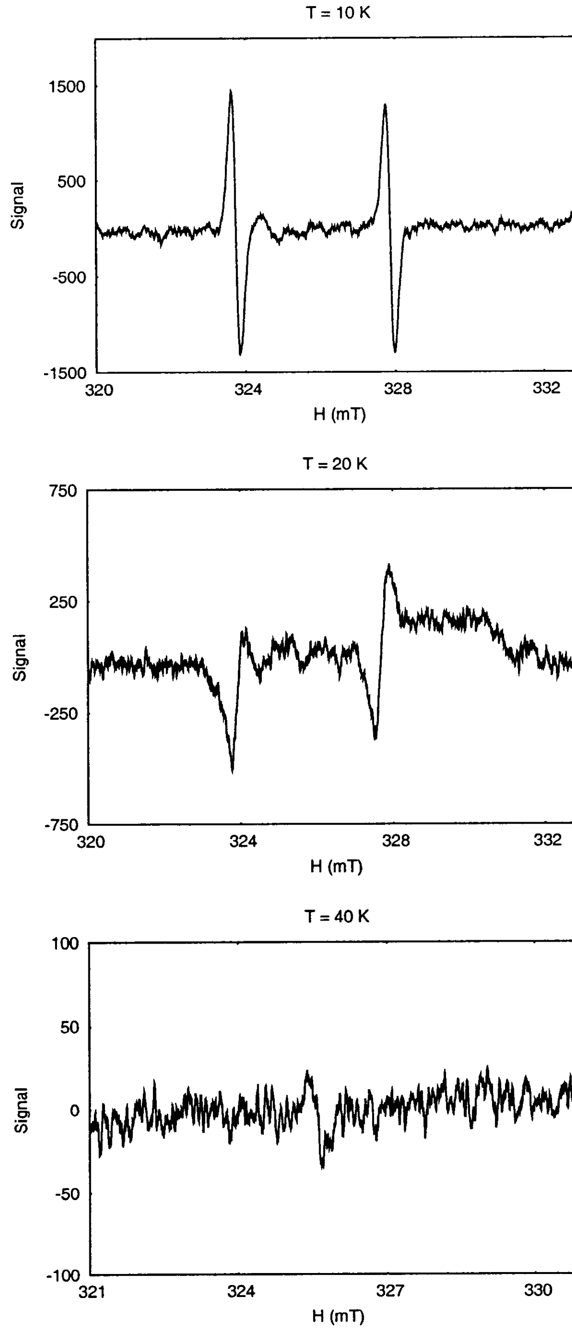

Figure 5-2: ESR signal of PN epiwafer for three different temperatures: 10 K (top), 20 K (middle), 40 K (bottom). In the top and middle plots the electrons are donor-bound and undergo hyperfine coupling with the phosphorus nuclei. In the bottom plot a sufficient number of electrons are excited and the ESR signal is that of the conduction electrons. The detected signal is actually the first-derivative of the absorbance since a lockin amplifier is used.

5.2 Spin-detection

Since ESR is able to detect a finite spin-polarization in the silicon induced by the applied magnetic field, it may also be able to detect spin-polarization resulting from the injection of a spin-polarized current. Namely, a spin-polarized current will replace (part of) the spin-unpolarized electron population with a spin-polarized one. This can be quantified with a back-of-the-envelope calculation as follows[2]. The drift-diffusion equation describing the spin-polarization is given by[83]

$$D\frac{\partial^2\sigma}{\partial z^2} + v_d\frac{\partial\sigma}{\partial z} - \frac{\sigma}{\tau_s} = 0, \tag{5.1}$$

where D is the diffusion constant, v_d is the drift velocity, and τ_s is the spin-coherence time. Eq. (5.1) must be solved under the boundary condition

$$J_{s|_{z=0}} = \frac{\alpha}{e}J = D\frac{\partial\sigma}{\partial z} \tag{5.2}$$

with α the fraction of the current that is spin-polarized. The solution of the system of equations (5.1-5.2) is given by

$$\begin{aligned} \sigma(z) &= \frac{2\alpha L_d n_0}{L_d + \sqrt{L_d^2 + 4L_s^2}} \exp\left(-\frac{z}{2L_s^2}\left(\sqrt{L_d^2 + 4L_s^2} - L_d\right)\right) \\ L_s &= \sqrt{D\tau_s} \\ L_d &= v_d\tau_s \end{aligned} \tag{5.3}$$

with L_s the spin-coherence length and L_d the diffusion length. An approximation to Eq. (5.3) can be obtained by noting that the spin-coherence length is much longer than the diffusion length. The spin-polarization then reduces to

$$\begin{aligned} &L_s \gg L_d : \\ &\sigma(z) = \alpha\frac{eEL_s}{kT}\exp\left(-\frac{z}{L_s}\right) \end{aligned} \tag{5.4}$$

[2]Courtesy of Anatoly Dementyev

where use has been made of the Einstein relation $D = \mu kT$ and E is the electric field. Now an estimate of the change of the ordinary conduction ESR signal induced by the spin-polarized current can be obtained. If the applied magnetic field is in-plane with the spin-injecting ferromagnet, the following enhancement[3] of the ESR signal can be expected

$$\frac{I}{I_0} \approx 1 + \alpha \frac{eEL_s^2}{g\mu_0 HL} \tag{5.5}$$

with L the total thickness of the sample. Here it has been assumed that the injected spin only contributes over the spin-coherence length hence the ratio L_s/L. This is reasonable because of the exponential decay in spin-polarization. This is visualized in Fig. 5-3 which plots the spin-polarization Eq (5.3) for three different values of τ_s. The ESR signal detected will be a contribution from the total sample volume. Hence

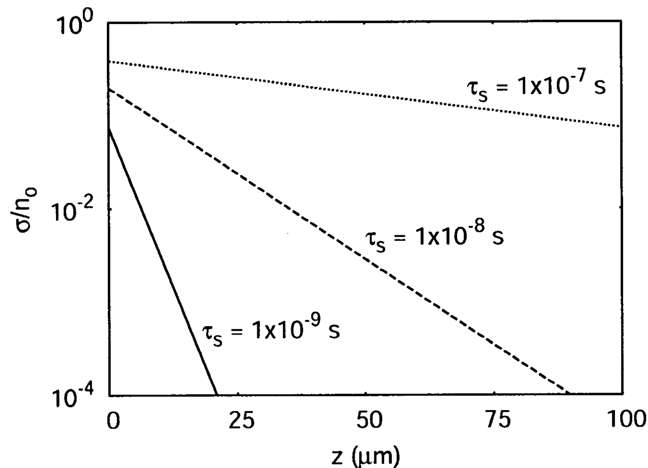

Figure 5-3: Ratio of spin-polarized carriers Eq. (5.3) to total number of carriers for three different spin-coherence times. The current density is 1 A/cm^2 and the dopant density 1×10^{15} cm^{-3}.

the enhancement of the ESR signal by the injected spin-polarization is determined by the ratio of the sample volume through which a (still) spin-polarized current flows to the total volume, expressed in Eq. (5.5) by the thickness ratio L_s/L with L the sample thickness. The spin-polarization will decay rapidly over a few spin-coherence lengths, as is evident from Fig. 5-3. Care should be taken to make L_s as large as

[3]The g-factor is positive.

possible compared to L. In the 2nd generation transistors described in Sec. 6.2, the wafer has therefore been thinned down to $100 - 150\ \mu m$ using a backside RIE etch. Also, the emitter contact area has been chosen as large as possible while still being compatible with limited current crowding, as described in Sec. 6.2.2. Besides, the doping concentration of the collector has been chosen quite low $10^{15}\ \text{cm}^{-3}$ which is a compromise between longer L_s and less initially unpolarized carriers for lower doping concentrations, and enough carriers present to give a measurable ESR signal.

Plugging the following numbers into Eq. (5.5): spin-coherence length $L_s = 30\ \mu m$ (corresponding to $\tau_s = 1\times10^{-7}$s), $L = 100\ \mu m$, $H = 0.3$ T, and electrical conductivity $\sigma = 10^2$ S/m gives

$$\frac{I}{I_0} \approx 1 + 2\alpha \times 10^{-3} J \tag{5.6}$$

hence a current density of 1 A/cm^2 would give a factor of 10 enhancement on the ESR signal which is significant.

Since the transistor surface is covered with metallic contacts, it is necessary to consider the attenuation of the rf-field by these metal films. The attenuation length of electromagnetic fields in metals is given by the skin depth [84]

$$\delta = \sqrt{\frac{2}{\omega\sigma\mu_0}} \tag{5.7}$$

with ω the radial frequency, σ the conductivity of the metal, and μ_0 the (vacuum) permeability. The rf-field will be attenuated exponentially over the skin depth which has been plotted for the three different metals used in the transistor in Fig. 5-4. It is observed from Fig. 5-4 that for film thicknesses upto 100 nm the attenuation is acceptable. At lower temperatures (i.e. $T = 100$ K) the attenuation will be enhanced somewhat because of the higher conductivity.

5.3 ESR on 1st generation transistors

Despite the low gain of the first generation transistors, ESR measurements have been performed trying to probe whether indeed a spin-polarized current is present

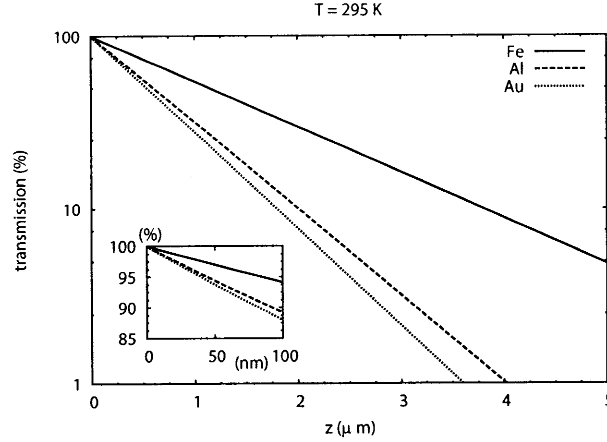

Figure 5-4: Transmission of rf-field through a metallic film versus film thickness. The inset shows the transmission over a narrow thickness range of 100 nm. The conductivities used in Eq. (5.7) have been taken from [76].

in the collector of the transistor. The measurements were performed with an X-band ESR machine with a microwave frequency of $\nu \approx 9.1$ GHz. Transistors were mounted in a glass probe (inner diameter 2 mm), filled with nitrogen exchange gas, and placed in a high-Q cavity in a cryostat in the center of the ESR electromagnet. Measurements were performed at $T = 100$ K which is the optimum value to detect spin-resonance, a result from the competition between thermal broadening and enough conduction electrons present. The results of a representative measurement are shown in Fig. 5-5. From Fig. 5-5 it is observed that the ESR signal gets smaller for larger collector currents whereas from Eq. (5.5) it is expected to get bigger if spin-injection results. Apparently, the spin-polarization injected is too small to offset the Joule heating induced by the current flowing through the sample. This is especially relevant considering the poor gain of the transistor yielding a large base current that contributes to heating as well. In light of these findings, the decision was taken to try to improve the transistor performance.

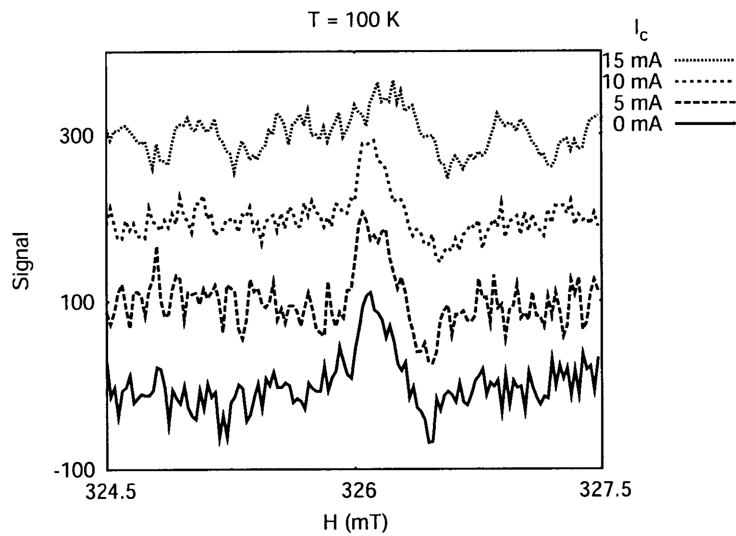

Figure 5-5: ESR signal of epiwafer transistor subject to varying levels of collector current I_c. The signal is diminished for higher I_c, likely because of the current induced heating.

Chapter 6

Fabrication of the tunneling emitter bipolar transistor

Two different fabrication schemes, referred to as generations in the following, have been used to fabricate the tunneling emitter bipolar transistor. The initial round of fabrication was useful to gain insight in the various aspects of making a bipolar transistor but did not produce transistors with a high current gain. In order to single out definitively the cause of the poor performance of the devices, the fabrication was greatly altered, helped by the fact that a research proposal had been granted that would fund this work. In this Chapter both fabrication sequences will be described; measurement results for each generation of transistor will be presented in Chapter 8. With the goal in mind to use ESR as a spin-detector, the transistor device design for both generations was influenced to facilitate ESR measurements on the transistors.

6.1 Epiwafer transistors

The first generation of transistors was based on silicon PN epiwafers that were donated by the company Siltronic. On request, a 10 μm thick boron-doped silicon layer was grown epitaxially on a 6 inch, (100), phosphorus-doped silicon wafer. The doping concentrations were chosen based on the simulation results of the spin transport

through a PN junction, described in Chapter 3. The N-type silicon had a resistivity of 2.5−5 Ωcm, corresponding to a doping concentration of $2\times10^{15}-9\times10^{14}$ cm^{-3}. The resistivity of the P-type layer was 4 Ωcm, corresponding to a doping concentration of 3×10^{15} cm^{-3}. The wafers were cleaved into 1×1 inch^2 pieces. Subsequently, bipolar transistors were made out of the pieces following the fabrication process described below.

6.1.1 Thinning down the base

The epilayer thickness of 10 μm was chosen to allow for flexibility in choosing the base width. The width had to be at least large enough to accommodate both the depletion region of the reverse biased base-collector junction and the depletion region of the emitter-base junction since otherwise punch-through of the transistor would result [85]. The depletion region width of an abrupt PN junction varies with applied voltage as [86]

$$\begin{aligned} z_n &= \sqrt{\frac{2K_s\varepsilon_0}{e}(V_{bi}-V)\frac{N_A}{N_D(N_A+N_D)}} \\ z_p &= \sqrt{\frac{2K_s\varepsilon_0}{e}(V_{bi}-V)\frac{N_D}{N_A(N_A+N_D)}} \\ V_{bi} &= \frac{kT}{e}\ln\left(\frac{N_DN_A}{n_i^2}\right) \end{aligned} \tag{6.1}$$

where z_n and z_p are the widths in the N- respectively P-region, K_s the dielectric constant, V_{bi} is the built-in potential and V the applied bias (plus voltage with respect to the P region). The emitter-base PN junction is a MIS diode and its depletion region extends into the base a distance [87]

$$\begin{aligned} W_d &= \sqrt{-\left(\frac{K_s\varepsilon_0}{C_{TB}}\right)^2+\frac{2K_s\varepsilon_0(-V-\phi_{MS})}{eN_D}}-\frac{K_s\varepsilon_0}{C_{TB}} \\ \phi_{MS} &= \phi_M-(\chi+\frac{E_g}{2}+(E_i-E_F)) \\ N_A &= n_i\exp\left(\frac{E_i-E_F}{kT}\right) \end{aligned} \tag{6.2}$$

where ϕ_{MS} is the difference between the work functions of the metal and semiconductor and C_{TB} the tunnel barrier capacitance. The bias dependence of the depletion widths Eq. (6.1) and Eq. (6.2) are shown in Fig. 6-1 for the doping concentrations of the PN epiwafer. From Fig. 6-1 it is apparent that a base width of a micron or

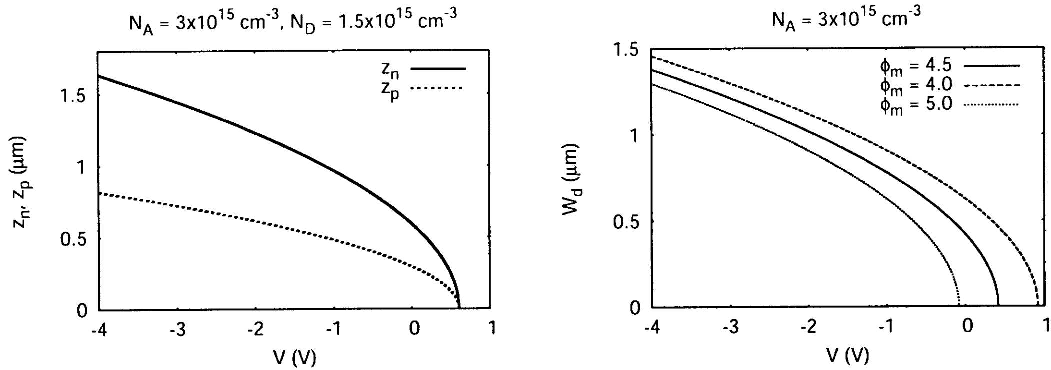

Figure 6-1: The left side shows the base-collector depletion region width inside the P region (x_p) and N region (x_n). The right plots the emitter-base depletion region inside the base for three different emitter work functions. The emitter tunnel barrier is 20 Å thick SiO_2. The bias voltage V is for both plots with respect to the base.

more is enough to prevent punch-through. Therefore transistors were made with a base width of between $1 - 6$ μm which is smaller than the minority carrier diffusion length. The base was thinned down using reactive ion etching (RIE) with as etch gas SF_6 since it does not leave residue on the silicon [88] and causes minimal physical damage [89].

6.1.2 Collector and base definition

The collector contact was defined first; it extends over the whole back of the sample. As the collector contact material was chosen aluminum, it is deposited using thermal evaporation. Prior to mounting in the evaporator, an HF-dip was performed to remove the native oxide on the silicon.

The base definition requires a photolithography step. The mask used was a transparency mask printed with a 5000 dpi (dots per inch) laser printer. It is shown in Fig. 6-2. As observable in Fig. 6-2, a positive photoresist was used. Aluminum was

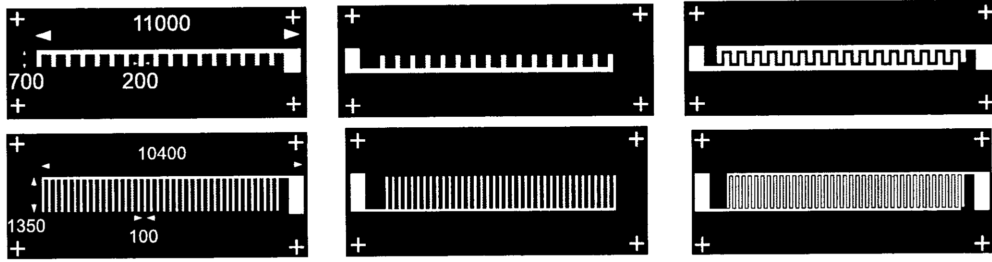

Figure 6-2: Mask drawing of the base (left), the emitter (middle), and the base and emitter together (right). The dimensions are in microns. The base-emitter separation is 100 μm (top) and 25 μm (bottom).

also used as the base-metal, again deposited by thermal evaporation, with an HF-dip just before mounting.

After lift-off, an annealing step was performed at $T = 450°$C for 30 min in a forming gas atmosphere (5% H_2, 95% N_2) using a home-made annealing system and boat; Appendix C.3 has a drawing of the latter. The annealing creates ohmic contacts for the base and collector simultaneously.

6.1.3 Emitter definition

The last step is the emitter definition, again by photolithography using the mask depicted in Fig. 6-2. Deposition of the tunnel barrier and emitter metal was done with ebeam evaporation in a UHV system. Chapter 10 describes a study on ebeam evaporation. The tunnel barrier material was chosen to be MgO, mainly because it can be deposited with the UHV system. Deposition happened at room-temperature, and hence the MgO is expected to be polycrystalline; see Chapter 4 for the properties of crystalline MgO. Since the ferromagnet was chosen to be iron, it is capped with a $5 - 10$ nm thick gold layer to prevent oxidation. After lift-off the device was ready for measurements. Finished devices are shown in Fig. 6-3.

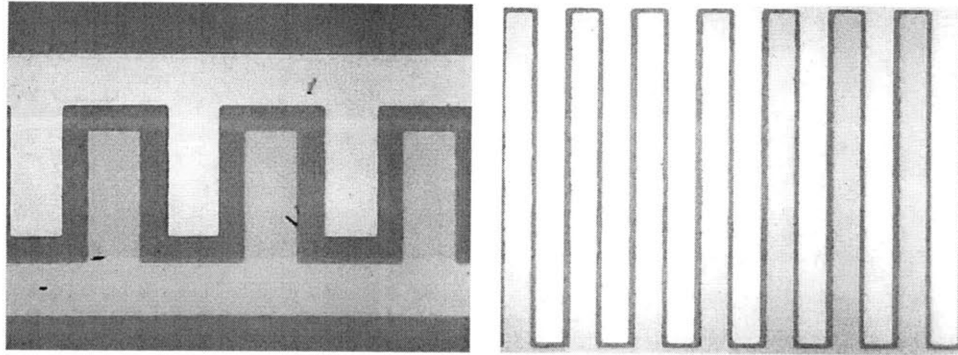

Figure 6-3: Top view of devices pn10mu_24 (left) and pn10mu_29 (right), showing the emitter and base contacts.

6.2 2nd generation transistors

In order to improve the transistor performance, the fabrication process was radically changed. Fabrication was done in the MTL facilities of MIT, that consist of a class-10 and -100 classroom. These facilities have many processing tools such as oxidation tubes, RCA cleaning stations, several different deposition tools, and standard photolithography equipment. Instead of working with wafer pieces as was done in the fabrication of the first generation transistors, described in Sec. 6.1, fabrication was started off with whole wafer processing.

6.2.1 Wafer choice

The choice for a wafer was determined by maximizing the spin-diffusion length while still being measurable by ESR as described in Chapter 5. For instance, the wafer growth method chosen was the float-zone method; those wafers have typically less impurities than wafers grown using the Czochralski process. Phosphorus was chosen as dopant, and for the resistivity $\rho = 2-6\ \Omega$cm was chosen, which has a corresponding doping concentration of [90] $2.3 \times 10^{15} - 7.5 \times 10^{14}$ cm^{-3}. Both phosphorus and the doping concentration are compatible with the ESR detection. The wafer size was chosen to be 4 inch; MTL has whole wafer processing capabilities for 6 inch and 4 inch, the latter was preferred in order to minimize the amount to etch from the

back as described below in Sec. 6.2.4. The wafer thickness is approximately 300 μm and the wafers are single-side polished.

6.2.2 Device shape

As discussed in Chapter 5, the emitter area should be chosen as large as possible since only the area below the emitter contributes to enhancing the ESR signal by spin-injection. However, care must be taken that no current crowding results. The contact shape is therefore chosen to be a pattern of alternating emitter and base strips, each of the strips connected to a long bar, like a comb. Examples are shown below in Figs. 6-9-6-10. The base and emitter contact pads are both on the same side and the device is large enough so that they are outside the high-Q cavity of the ESR. The width of the base strips is 60 μm and the separation between the base and emitter strips is 20 μm. However, part of the base and emitter strips overlap the thermal oxide to make sure no surface is exposed to air. The overlap with the oxide for both contacts is 12.5 μm. Hence the effective width of the base strip is 35 μm. The width of the emitter strips is chosen based on Fig. 6-4 which plots both the fractional area of the device that is the (effective) emitter A_e, and the separation between the center of the emitter and the base strip d_{eb}. Settled upon was an effective emitter

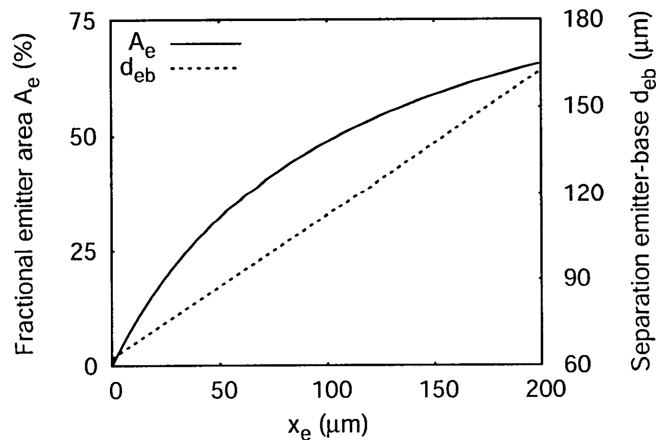

Figure 6-4: Fractional emitter area A_e and distance between the centers of the emitter and base strips d_{eb} as a function of emitter strip width x_e.

strip width of 95 μm (total width 120 μm) yielding according to Fig. 6-4 a fractional area of 47.5% and emitter-base separation of 110 μm. The actual fractional emitter area is actually slightly less because of the connecting bar and the separation between contacts and edge of the active region.

6.2.3 Isolation of the transistors

Individual transistors on a wafer are isolated from each other by a thick thermal oxide. This oxide is grown first, using wet oxidation as described in Sec. A.1, and is 1 μm thick. Of course the oxide grows on both sides of the wafer, which is relevant for the next step.

6.2.4 Backside etch

As described in Chapter 5, the total sample volume contributes to the ESR signal whereas only the part within the spin-diffusion length will yield any enhancement. Therefore it was decided to thin the wafers down using a backside etch. Since the wafers become more brittle when thinned down, only the device area was etched leaving enough support for wafer handling. This requires a photostep to define the device area on the back of the wafer. All photolithoraphy was performed with an EV620 mask-aligner that can do backside alignment. The support requirement also places restrictions on how many devices can be defined on a wafer and, importantly, where they are placed. This is especially relevant for the ion implantation as discussed below in Sec. 6.2.6 since the wafers are spinned at high speed and the breakage of a wafer is to be avoided during the implant. The mask design chosen is shown in Fig. 6-5. Hence as seen in Fig. 6-5, the wafer edge was left unetched which yields enough structural support. After the backside device definition with photolithography, a buffered oxide (BOE) etch was performed to remove the thick thermal oxide of Sec. 6.2.3. Then the wafers were mounted upside down on a 6 inch dummy with photoresist since the RIE tool only admits 6 inch wafers. As the etching gas SF_6 was chosen;

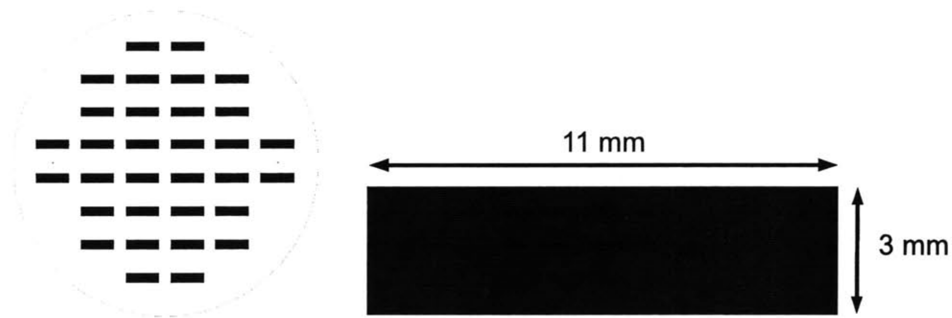

Figure 6-5: Back-side etch mask; whole wafer (left) and device dimensions (right). The mask is printed with a laser printer and subsequently transferred to a chrome blank. The actual mask is the negative image of this Figure.

the etch-rate was about 1 μm/min[1], and the etch depth was approximately 150 μm. The photoresist on the front will get etched as well but is thick enough (1 μm) to last through the run. The photoresist on the back will get burnt because of the heat development[2]. Following the STS etch, the 4 inch wafers are dismounted with a piranha etch, followed by an ash-step. The back-side of the resulting device is shown in Fig. 6-6.

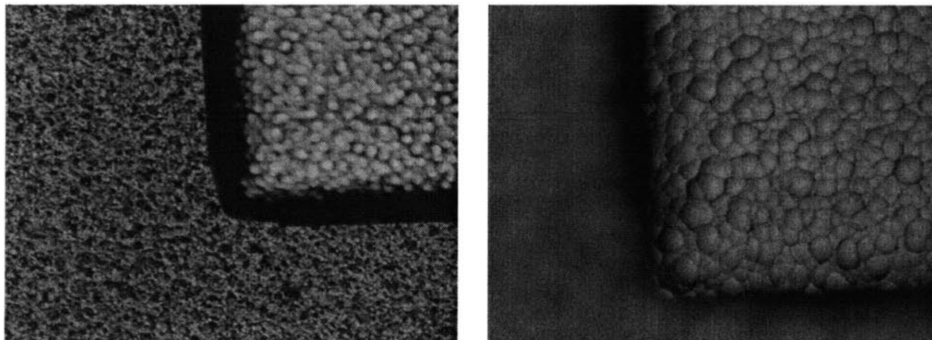

Figure 6-6: Back-side etched device of wafer BJT_W06. The left focusses on the unetched part and the right on the etched region.

[1]The etch rate depends a lot on the chamber conditions and will vary from day to day and even from run to run.

[2]This can be reduced but not avoided by applying the photoresist in a star-shape, leaving cooling channels available for heat dissipation.

6.2.5 Active area

Following the back-side device definition, the active region on the front-side must be defined. This was performed by a photo-step with a subsequent BOE etch. The mask design is shown in Fig. 6-7.

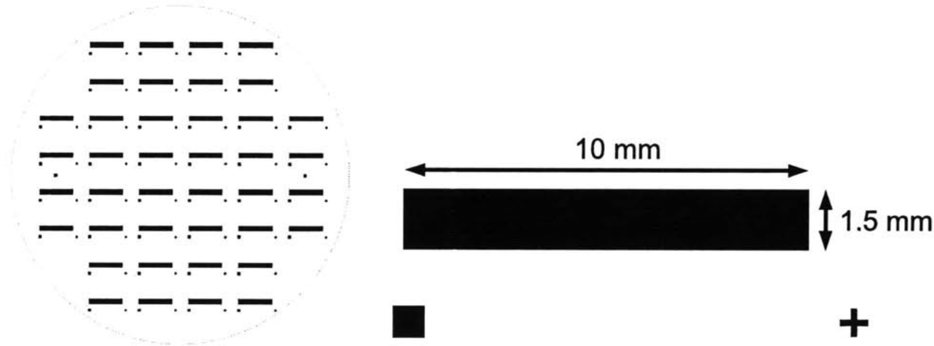

Figure 6-7: Active region mask; whole wafer (left) and device dimensions (right). As compared with Fig. 6-5, more devices are outlayed yielding some devices with no back-side etch. The square and cross on the right side are markers used for alignment of the contact masks. This mask is also printed with a laser printer and subsequently transferred to a chrome blank. The actual mask is the negative image of what is depicted here.

6.2.6 Ion implantation

The base of the transistor was implanted through a thermal oxide. The oxide was grown using dry oxidation as described in Sec. A.1 and three different oxide thicknesses had been grown: 1100 – 1200 Å, 1400 – 1460 Å, and 1750 – 1800 Å. The wafers were sent to the company Innovion where boron was implanted from the top with a dose and energy of 2×10^{14} cm^{-2} and 26 keV, and phosphorus was implanted from the back with 5×10^{15} cm^{-2} at 180 keV. The back-side implant creates an ohmic contact to the collector region. After return from the implant the wafers were piranha cleaned. Then a short anneal was performed at T = 950°C for 10 min to restore crystallinity.

6.2.7 Cut of Emitter-Base

After the anneal following the ion implant, the wafers were ready for contact definition. The first step is to cut through the ion implant oxide to open a window for the base and emitter. The mask is shown in Fig. 6-8.

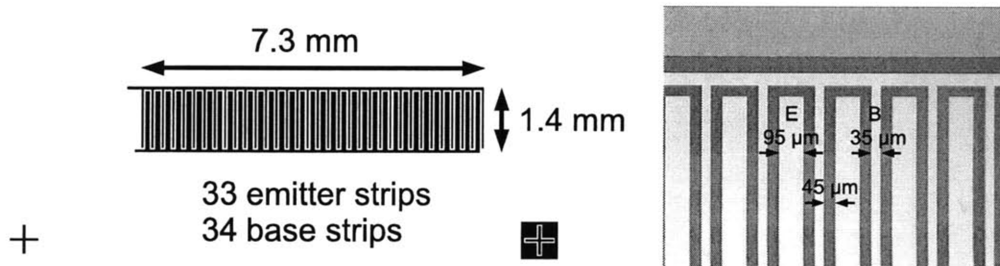

Figure 6-8: Cut of emitter-base through the oxide; shown are the mask of the whole device (left), and the real device BJT_W03 (right). E and B indicate the cut for the emitter and base, respectively. The mask is made with a Heidelberg laser writer and is actually the negative image of what is shown here.

6.2.8 Base definition

For the initial trials of this generation of transistors, the base contact was defined before the emitter contact. The reason for this sequence was that the emitter had to be deposited in the magnet lab in order to use a UHV tool to deposit MgO and Fe. Samples taken out of the cleanroom however cannot be brought back in again. Hence for the first trial wafers the base contact was defined for the whole wafer at once. The base definition requires a photo-step where now an image reversal mask is used to give some undercut that assists in lift-off. The mask is shown in Fig. 6-9.

Immediately before mounting in the ebeam evaporator, an HF-dip was done (5 % HF, 1 min). Aluminum was chosen as the contact material since it forms a good ohmic contact to P-silicon. After the lift-off a sintering step was performed (T = 450°C, 30 min), that diffused the aluminum into the silicon. The resulting device is shown in Fig. 6-9. Often the sintering is done in a hydrogen atmosphere which reduces the number of interface states since the hydrogen binds to the dangling bonds of the silicon surface atoms. However, because the hydrogen option was unavailable at the

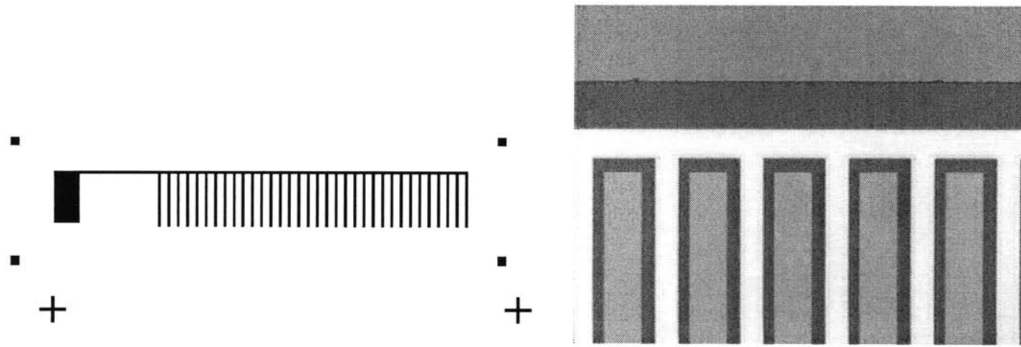

Figure 6-9: Base contact definition; shown are a mask of the whole device (left), and the real device BJT_W06 (right). The mask is made with a Heidelberg laser writer.

time of the device development, sintering was performed without it. Good ohmic contacts were obtained nevertheless.

6.3 Wafer pieces

Since the UHV tool in the magnet lab only accepts 1×1 inch^2 size pieces, the wafer were cleaved before definition of the emitter.

6.3.1 Emitter definition (1)

The emitter is defined with one last photo-step, again using a negative mask. A lift-off step was chosen instead of an etch-step. Consequentially, the MgO had to be deposited at room-temperature and is at best polycrystalline. This choice was made because of ease of fabrication; when a working device would have been demonstrated, it would have been relatively straightforward to switch to a high-temperature deposition step using either high-T bearing resist (for instance PMGI) or changing to an etch-step. The (absence of) crystallinity of the MgO is not expected to influence the transistor action directly, but would affect the spin-filtering properties of the MgO. A crystalline MgO may however be able to withstand larger voltages or current levels, both of which *would* affect the transistor action. The native oxide is etched away before mounting into the UHV system with an HF-dip and the MgO and Fe are deposited with ebeam

evaporation. To prevent oxidation, the Fe is capped with an aluminum layer, in-situ deposited and also with ebeam evaporation. The emitter mask is also an image reversal mask and is shown in Fig. 6-10, together with an image of a final device.

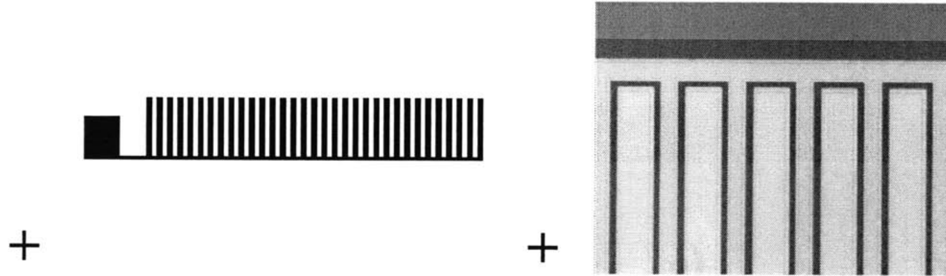

Figure 6-10: Emitter contact definition; the mask is on the left, and the finished device BJT_W03_P08 on the right. The mask is made with a Heidelberg laser writer.

6.3.2 Emitter definition (2)

Because of the high requirements on the tunnel barrier as described in Sec. 8.4, decided was upon to scale down the tunnel barrier area in order to better probe the tunnel barrier characteristics. This was enabled by the development of the probe-station, described in Sec. C.5, with which small size contacts could now easily be probed. In addition the base-first fabrication sequence was changed to emitter-first. Only a few options were available as a tunnel barrier because of the strict requirements for growing such a barrier. The high-quality tools available were either atomic layer deposition (ALD) with as tunnel barrier aluminum-oxide, or oxidation yielding silicon-oxide. Both of the tools are high-temperature steps requiring the change to a deposit-all over, followed by an etch-step. Silicon-oxide was initially chosen as the tunnel barrier. The oxide was grown using dry oxidation: 850°C for 6 min which yields about 20 Å. Different emitter metals were used in order to investigate whether a low work function emitter is essential for the working of the transistor, as claimed in [91]. The metals were aluminum, deposited with a thermal evaporator, and tungsten-nitride (WN), deposited with ALD. The same ALD tool and precursor were used as in [92] and the WN work function in this work is therefore assumed to be same as

in that study, namely 4.6 eV. Aluminum has a much lower work function: 4.1 eV. The disadvantage of thermal SiO_2 as a tunnel barrier is that after the growth in the diffusion tube, the tunnel barrier is exposed to air before mounting in the metal deposition tool. In fact, both these metals required taking the elevator to a different lab and it took between $5-10$ min before the sample could be mounted. In addition, the thermal evaporator was not in a cleanroom and the chamber contaminated, reflected by a base pressure of only high in the 10^{-6} Torr range. The tunnel barrier-metal surface is therefore likely to be contaminated which may appear as charge inside the tunnel barrier. See Appendix D.2.4 for an example of the effect of charge on the base-emitter IV characteristics.

By using these metals, the transistor does not serve as a spin-injector anymore. Switching to a ferromagnet would have been a straightforward change however after the working of the device had been fully analyzed and understood. The new emitter is shown in Fig. 6-11. The wafers were diced into quarters, to save material

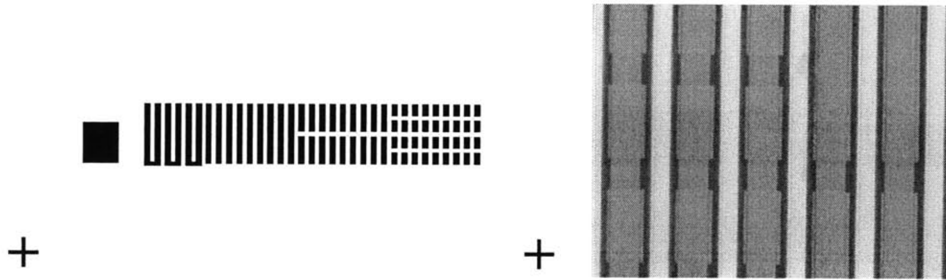

Figure 6-11: Emitter contact definition(2); the mask is on the left, and the finished device BJT_W14_P04_j on the right. The mask is made with a Heidelberg laser writer.

while still being compatable with undergoing RCA cleaning and oxidation. After emitter deposition, the quarters were further diced into 3 parts since those can be spincoat more easily as well as to have backup samples when the emitter-etch-step fails. The aluminum was etched with a PAN etch solution[3], the WN with RIE using SF_6 as etchant[4]. After the emitter is ready, the base can be defined as described be-

[3]It etched the 800 A at room-temperature in 4 min.

[4]WN is readily etched with SF_6 but the etch rate is of course highly contingent upon the tool and conditions.

fore, however, now without the sintering step to improve the ohmic contact between the base metal and the P-region because of potential damage to the emitter-tunnel barrier. The resulting base contact was found though to be low-resistive.

After analysis of the devices with the SiO_2 tunnel barrier, also using Al_2O_3 as a barrier was investigated. The Al_2O_3 was deposited with ALD. As precursor was used TDMAA (Tris(dimethylamido)aluminum) and the barrier was grown at a substrate temperature of 200°C, followed by the in-situ deposition of WN. Other fabrication steps were the same as before.

Above have been described the fabrication processing steps of the two generations of tunneling emitter bipolar transistors considered in this work. In the next Chapter, measurement findings on the PN epiwafer transistors will be given, followed in Chapter 8 by measurement results on all transistors.

Chapter 7

Observation of Negative Differential Transconductance in tunneling emitter bipolar transistors

In general negative differential resistance (NDR) arises from the existence of bias-dependent states into which the charge carriers can tunnel. It has been observed in many different kinds of systems, but all having in common these tunneling states. Its prime example remains to date the device in which the effect was observed originally; the Esaki tunnel diode [93], named after its discoverer. The tunnel diode works as a result of tunneling from the conduction band into the valence band for a certain range of bias voltages, a consequence of the extreme band-bending for heavily doped NP-junctions. This is illustrated in Fig. 7-1. The valley in the IV characteristic results from the N-region conduction band becoming higher in energy than the valence band of the P-region.

Another system displaying NDR is a metal-insulator-semiconductor (MIS) diode where the semiconductor is degenerately doped with holes. NDR results because electrons may tunnel into the valence band before it is energetically favorable to tun-

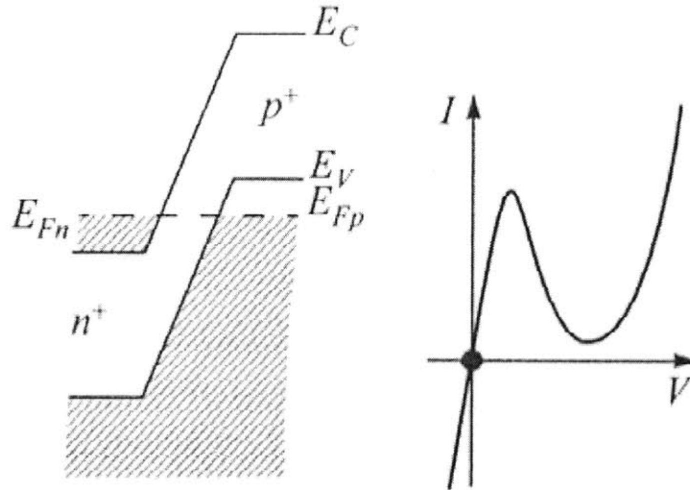

Figure 7-1: Adapted from [87]. Esaki tunnel diode; the left shows the extreme band bending of a heavily doped NP junction, the right gives the IV characteristic (voltage w.r.t. P-region).

nel directly into the conduction band. This is depicted in Fig. 7-2. In the case of Fig.

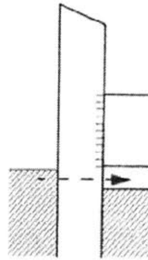

Figure 7-2: Adapted from [87]. MIS tunnel diode with the metal negatively biased compared to the semiconductor.

7-2, the decrease in current is caused by the effective tunnel barrier height seen by the valence electrons in the semiconductor becoming higher for increasing bias voltages, since the semiconductor energy bands move down. The difference in tunnel barrier height for valence and conduction band electrons will be discussed in Sec. 8.2.

NDR may also result in tunneling emitter bipolar transistors, but with valence band tunneling replaced by tunneling into an inversion layer. Also the reason for the valley in the IV characteristic differs; it stems from a geometric effect. This is described in

[94] on which the study described next is based.

7.1 Negative differential transconductance in tunneling emitter bipolar transistors

The first generation of transistors display negative differential transconductance (NDTC). Device simulations reveal that the NDTC is a consequence of an inversion layer at the tunneling-oxide/P-Silicon interface for low base voltages. Electrons travel laterally through the inversion layer into the base and give rise to an increase in collector current. The NDTC results from the recombination of those electrons at the interface between emitter and base contact which is dependent on the base voltage. For larger base voltages the inversion layer disappears marking the onset of normal bipolar transistor behavior.

7.1.1 Introduction

Negative differential conductance (NDC) which saw the limelight with the realization of the Esaki tunneling diode[93] has been predicted and observed to occur in a range of electronics devices[95, 96, 97, 98]. The fundamental origin is the appearance of bias dependent states into which charge carriers can tunnel. Much attention has been devoted to this phenomenon because of the promise it holds to realize high-frequency oscillators. Here is reported the observation of NDC in the collector current of a tunneling emitter bipolar transistor, i.e. Negative Differential Trans-Conductance (NDTC). Gate controlled NDC has been observed in tunnel transistors[99] but never before in the transconductance of bipolar transistors, although theoretical studies of these kind of devices exist[100, 101]. The emitter of the NPN bipolar transistor is comprised of a ferromagnet (Fe)/tunnel barrier (MgO) stack. Different from the metal emitter bipolar transistors in [102][91], a ferromagnet is here chosen as a emitter metal in order to use the transistor as a spin-injection device. In [103] it was theoretically predicted that devices based on tunnel Schottky contacts (although with a different

geometry) may display NDC. Below it is argued that the origin is the formation of an inversion layer at the MgO/P-Silicon interface for low base-emitter voltages, acting not unlike the quantum wells of known NDC devices.

7.1.2 Device fabrication

Transistors were made out of a PN epiwafer and the fabrication has been described in Sec. 6.1. A top-view image of a fabricated device is shown in Fig. 7-3. The base and emitter contacts consist of an alternating long strip pattern designed to minimize current crowding.

7.1.3 Measurement results

Room-temperature measurements were performed in the common emitter geometry with the emitter grounded. All the fabricated devices showed transistor action, an example of which is given in Fig. 7-3. The current gain of the transistors is low

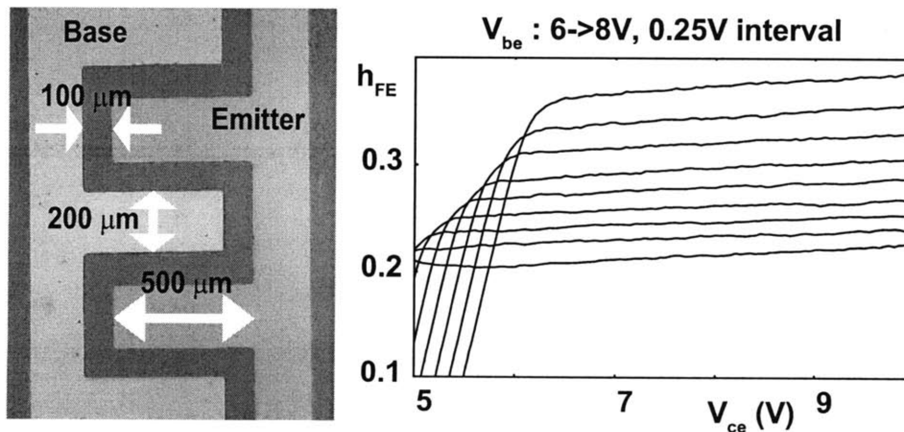

Figure 7-3: On the left is shown a top view micrograph of the tunneling emitter bipolar transistor. The right plot depicts the gain h_{FE} as a function of collector voltage V_{ce} for different base voltages V_{be}.

($\approx$ 0.3), a possible result from a surface current between the base and emitter, see below in Sec. 7.1.4.

The NDTC regime is revealed in the Gummel plot given in Fig. 7-4. For zero base

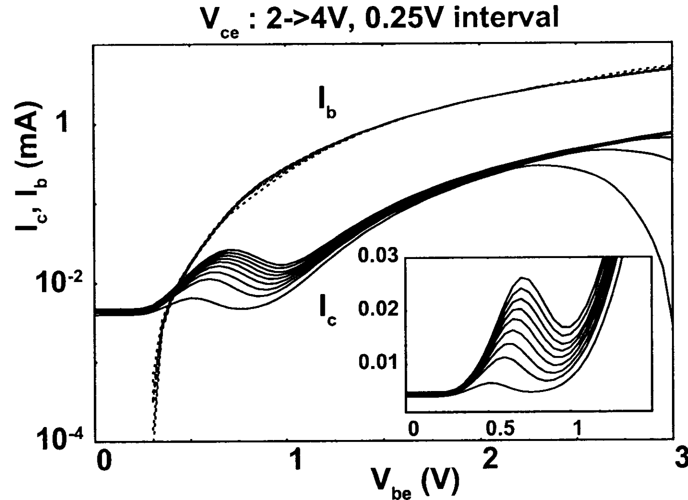

Figure 7-4: Measured Gummel plot showing the collector I_c and base I_b currents as a function of base voltage V_{be} for different collector voltages V_{ce}. The inset zooms in on the NDTC phenomenom. The base width of this transistor is 4 μm.

voltage (V_{be}) the nonzero collector current (I_c) in Fig. 7-4 is due to leakage current between collector and emitter contact. When the base voltage is cranked up, an increase in collector current is observed. Further increasing V_{be} first levels off, and then decreases I_c which is the NDTC regime. After reaching a local minimum, I_c starts to increase again which is the normal active transistor regime and will finally decrease and reverse sign as the Silicon PN junction becomes forward biased.
Several transistors, fabricated in different runs and with different based widths displayed this behavior, as shown in Fig. 7-5.

7.1.4 Simulation of the NDTC

In order to understand the origin of the NDTC feature the transistor is simulated with the two-dimensional (2D) device simulator Medici. The simulated device geometry chosen consists of an emitter contact sandwiched between two base contacts, resembling the measured transistors but with smaller dimensions. The corresponding Gummel plot is shown in Fig. 7-6. The NDTC phenomenom can be clearly

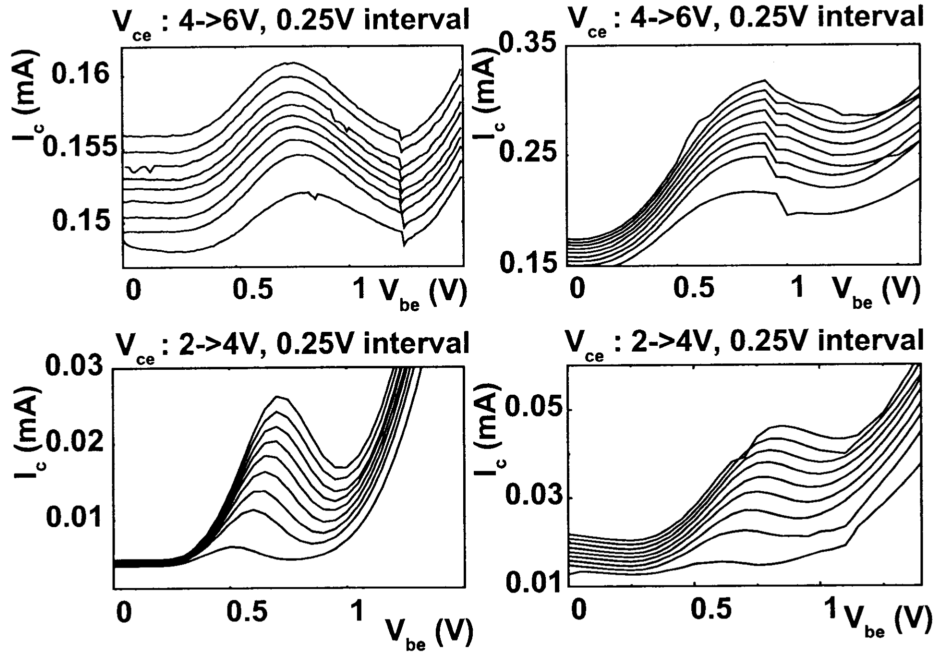

Figure 7-5: NDTC peaks for 4 different devices with different base widths. From left to right, top to bottom the widths are 1.5 μm, 2.1 μm, 4.0 μm, 4.9 μm. The bottom left is the NDTC feature of Fig. 7-4.

observed in the I_c of Fig. 7-6 and resembles the measurement result given in Fig. 7-4. Simulation parameters have been adjusted in order to qualitatively reproduce the measurement results. For instance, for the base current (I_b) to be bigger than I_c for larger biases, an extra (low-conductance) leakage path was included corresponding to a surface current between the base and emitter (a consequence of which is the low gain of the transistor). The currents in the simulated Gummel plot change over more orders of magnitude than in the measured Gummel plot. This indicates that for large V_{be} additional impedances play a role experimentally that are not captured in the model. Neither the leakage nor the presumably missing impedances would affect the NDTC though. Simulation parameters that did influence the NDTC were surface recombination velocity (between the emitter and base), emitter work function, and donor interface states density. By tuning these parameters, the measured NDTC structure could be well reproduced. The only characteristic that the simulation failed to reproduce was the shift of the NDTC peak to larger V_{be} for increasing collector

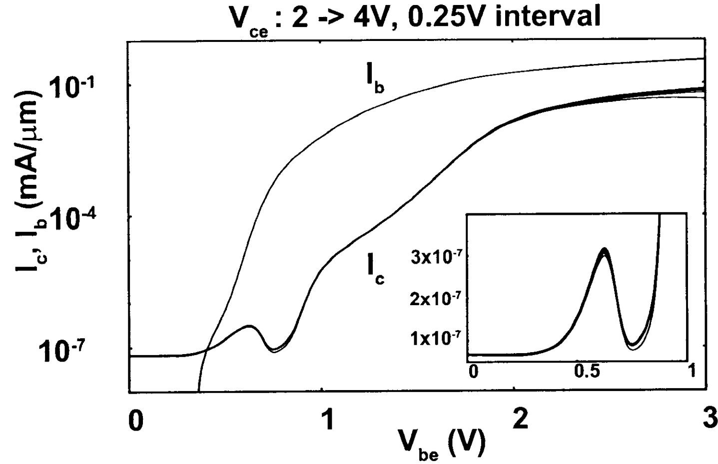

Figure 7-6: Simulated Gummel plot for different V_{ce}. On the left is shown both I_b and I_c over a wide range, the right plot zooms in on the NDTC feature which is the small bump in the left-hand plot. The maximum of the NDTC happens for $V_{be} = 0.62$ V and the minimum for $V_{be} = 0.75$ V. The currents are per unit length since it is a 2D simulation. The base width is 3 μm.

voltage (V_{ce}) which was observed for transistors with a somewhat thicker base as the one in Fig. 7-4. A possible origin of the shift is described below. The NDTC in the Gummel plot as well as its dependence on the given parameters can be understood from the bandstructure and electron concentration on the maximum of the NDTC peak, as given in Fig. 7-7. The bandstructure given in Fig. 7-7 displays the familiar PN behavior with the junction at $z = 3.1$ μm. Interestingly, it is observed that an inversion layer exists next to the tunneling oxide of the emitter. The electrons in the inversion layer are provided both by the emitter and by the interface donors (resulting for instance from an imperfect tunnel barrier). These electrons give rise to the increase in I_c for low V_{be}. They can escape the inversion layer by travelling laterally to where the emitter (and inversion layer) ends which they will do so for increasing V_{be}. Then they will diffuse either further into the base and subsequently be swept into the collector, or instead recombine, mostly at the surface between the emitter and base contact. The NDTC, i.e. the *decrease* in I_c for increasing V_{be} is revealed by looking at the electron current densities along and parallel to the inversion layer, both at the maximum and minimum of the NDTC feature, as given in Fig. 7-8. From Fig. 7-8 it

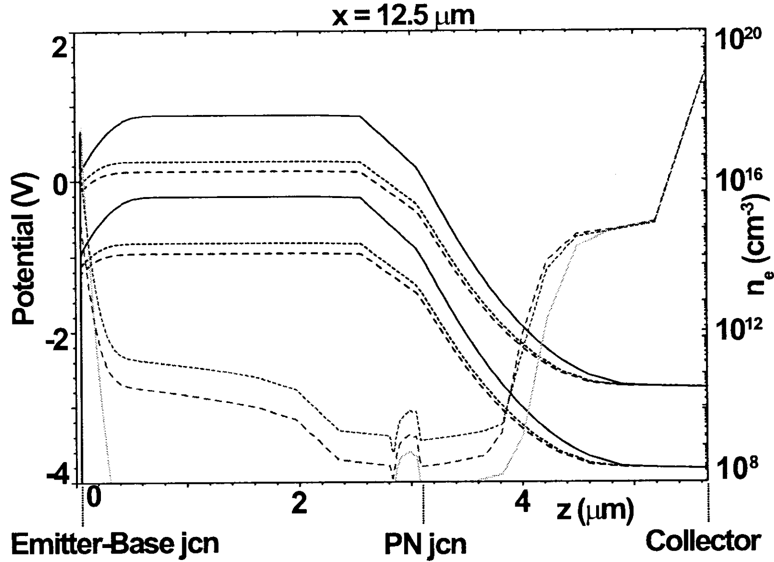

Figure 7-7: [Color online] Band structure (black) and electron concentration (colored) along the cross-section $x = 12.5$ μm intersecting the emitter contact, for bias conditions $V_{ce} = 3$ V and $V_{be} = 0,\ 0.62,\ 0.75$ V with solid, fine-dashed, and dashed lines respectively. The inversion layer can be discerned at the very left side, adjacent to the tunneling oxide of the emitter. At the very right side is the collector contact, the PN junction is at 3.1 μm.

is seen that at the minimum of the NDTC the electron current density is more concentrated close to interface with the tunneling oxide and consequently breaks out of the inversion layer closer to the surface between emitter and base contact, as compared to the electron current at the maximum of the NDTC. This is a result of positive charge piling up at the surface which yields an increase in lateral current flow through the inversion layer with a corresponding decrease in electron concentration in the middle of the layer, as observed in Fig. 7-7. The consequence is that a larger fraction of the electrons recombine instead of making it to the collector with corresponding decrease in I_c. The shift of the NDTC peak for increasing V_{ce} as seen in Fig. 7-4 may be due to the fact that then larger V_{be} values are possible before the recombination starts to dominate. This increase in V_{be} may yield a larger number of electrons in the inversion layer as a result of, for instance, bias-dependent interface donors and/or an increase in tunneling current from the emitter. The simulation assumed a bias-independent number of interface donors and the tunneling model in the simulation may differ from

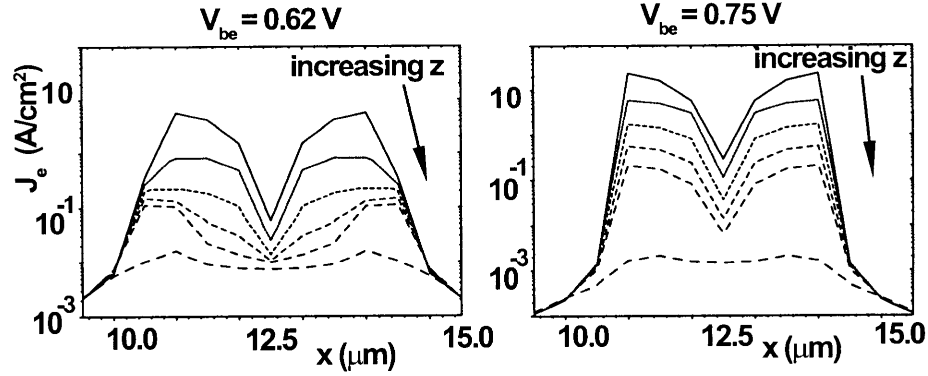

Figure 7-8: Simulated electron current density at the maximum of the NDTC feature (left plot) and minimum (right plot) parallel to the emitter for increasing distance z away from the inversion layer (towards the collector). The z-distances are 0 (in the inversion layer), 25 nm, 50 nm, 75 nm, 100 nm, 500 nm. The emitter contact extends from $x = 11$ μm to $x = 14$ μm.

what is the case experimentally. When V_{be} is further increased beyond the NDTC, the energy bands straighten out, the inversion layer disappears and the transistor enters the active region with electrons from the emitter tunneling straight into the base and being swept into the collector.

7.1.5 Conclusions

In summary, for the first time negative differential transconductance has been observed in the Gummel plot of tunneling emitter bipolar transistors. Device simulations reveal that the NDTC results from the existence of an inversion layer next to the tunneling oxide which is populated by electrons tunneling from the emitter as well as by interface donors. Electrons in the inversion layer travel parallel to the emitter contact and break out at the edges and either recombine or are swept into the collector of the transistor. The measurement and simulation results are relevant as well for other NDC geometries, such as FET style tunnel transistors since they offer crucial insight into how the geometry and charge distribution may determine the ultimate performance of such devices. Moreover, the implementation of the collector contact in the geometry here may itself be used for device applications.

Chapter 8

On the gain of tunneling emitter bipolar transistors

In this chapter both the working, and measurements of tunneling emitter bipolar transistors will be discussed. First, however, a short description of an ordinary NPN bipolar junction transistor (BJT) will be given, following [85].

8.1 NPN BJT

The NPN BJT consists of 2 back-to-back diodes with the base region shared between the diodes. A schematic of the transistor is shown in Fig. 8-1. The different biasing of the PN junctions (forward and reversed) allows for 4 device operation regions. Under normal operating conditions, the emitter-base junction is forward biased and the base-collector is reverse biased, which is called the *active region.* Under those conditions, electrons are injected into the base. A fraction of those recombine with holes within the depletion region giving a contribution I_{rg} to the base current I_b. In addition, holes will be injected into the emitter yielding the current I_{pe} which adds as well to I_b. The emitter injection efficiency is then defined as

$$\gamma = \frac{I_{ne}}{I_{ne} + I_{rg} + I_{pe}} \tag{8.1}$$

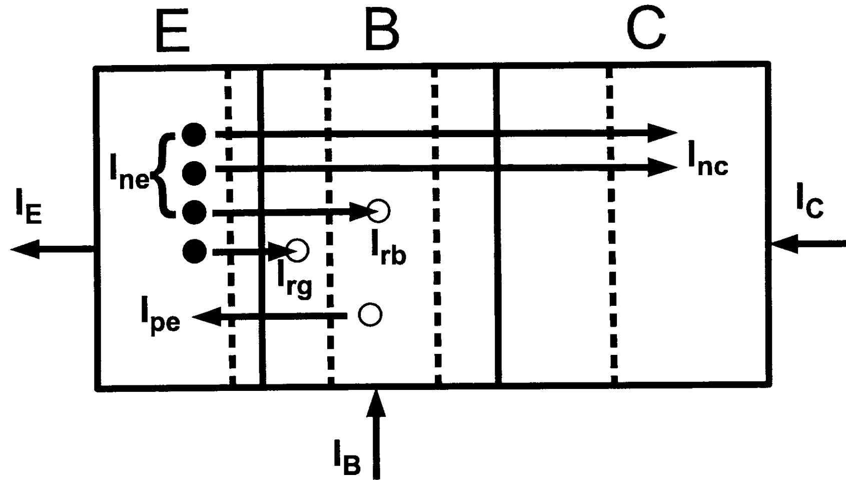

Figure 8-1: Schematic of an NPN transistor with major current components indicated. The dashed vertical lines indicate the depletion region edges. The currents inside the device are the carrier currents (electrons and holes) whereas those outside are the electrical currents. In the schematic and discussion the base-collector leakage current has been neglected since for a good PN junction it is negligible.

and is the ratio of emitter current that makes it into the base over the total emitter current. The electrons that reach the base will drift-diffuse further and are subsequently swept into the collector by the electric field of the reverse biased base-collector junction. A fraction of those electrons will however recombine inside the base giving a current contribution I_{rb} to the base current. The transport factor α_T expresses the recombination inside the base

$$\alpha_T = \frac{I_{nc}}{I_{ne}}. \tag{8.2}$$

The ratio of the collector current over the emitter current can then be written as

$$\alpha = \frac{I_c}{I_e} = \gamma \alpha_T \tag{8.3}$$

and α is called the common base current gain. This gain is obtained when the emitter and collector currents are used as input and output parameter, respectively, and the base as the common terminal. Another configuration is obtained with the base current

instead of the emitter current as an input parameter. The associated current gain is

$$\begin{aligned}\beta &= \frac{I_c}{I_b} \equiv h_{FE} \\ &= \frac{\alpha}{1-\alpha}\end{aligned} \tag{8.4}$$

and is called the common emitter current gain. All the measurements presented below were done in the common emitter geometry.

In order to obtain expressions for the currents, the continuity and drift-diffusion equations need to be solved. A simplifying expression for the current gain can however be readily obtained if the recombination in the depletion region and in the base are neglected, i.e. I_{rg} and I_{rb} of Fig. 8-1 are zero. The base current then solely consists of holes injected into the emitter, I_{pe}, and the collector current is equal to I_{ne}. The current through a PN junction is determined by the minority carrier diffusion inside the bulk region, under the assumption of zero drift outside the depletion region [86]. The bias dependence enters via the boundary conditions for the carriers at the depletion region edge[1], but since both I_{ne} and I_{pe} are forward bias currents, they have the same dependence on the base-emitter voltage V_{be}, namely the standard exponential $\exp\left(\frac{qV_{be}}{kT}\right)$. The currents through the PN junction are then determined by the number of minority carriers times the diffusion velocity. Accordingly, I_{ne} and I_{pe} take the form

$$\begin{aligned}I_{ne} &= A\frac{n_i^2}{N_A}\frac{L_{nb}}{\tau_n}\exp\left(\frac{qV_{be}}{kT}\right) = \frac{An_i^2 D_{nb}}{L_{nb}N_A}\exp\left(\frac{qV_{be}}{kT}\right) \\ I_{pe} &= \frac{An_i^2 D_{pe}}{L_{pe}N_D}\exp\left(\frac{qV_{be}}{kT}\right)\end{aligned} \tag{8.5}$$

with L_{nb} and L_{pe} the minority electron and hole diffusion length in the base and emitter, respectively, and with A the junction area. D_{nb} and D_{pe} are the minority

[1] In equilibrium the carrier diffusion and drift by the built-in electric field cancel each other, yielding zero current. The forward bias brings the junction out of equilibrium, and enhances the carrier diffusion.

diffusion constants given by

$$D_{nb} = \sqrt{L_{nb}\tau_n}$$
$$D_{pe} = \sqrt{L_{pe}\tau_p}. \tag{8.6}$$

Recombination inside the base has been neglected, requiring that the base width is much less than the minority diffusion length: $W_B \ll L_{nb}$, hence W_B should be substituted for L_{nb} in Eq. (8.5). The common emitter current gain is then given by the ratio and found to be

$$h_{FE} = \frac{D_{nb} L_{pe} N_D}{D_{pe} W_B N_A}. \tag{8.7}$$

Therefore h_{FE} is directly proportional to the ratio of the emitter doping and the base doping. The total amount of doping inside the base is defined as the base Gummel number[2]

$$G_b = W_B N_A. \tag{8.8}$$

Example transistor action plots of an NPN BJT are shown in Fig. 8-2.

8.1.1 Temperature dependence of current gain

The characteristics of semiconductors are sensitively dependent on temperature since the temperature directly affects the majority and minority carrier concentration as well as the Fermi level. This is shown in Fig. 8-3. It is observed from Fig. 8-3 that below a certain temperature the acceptors freeze out whereas for high temperatures intrinsic conduction starts to dominate. For the current gain however, this temperature dependence is (partially) cancelled since, from Eq. (8.7), $\mathrm{h_{FE}}$ depends on the ratio of the doping concentrations of the emitter and base. The dominant temperature dependence comes from the doping-induced band gap narrowing. The apparent band gap narrowing is a way to incorporate deviations from the approximate Maxwell-Boltzmann statistics due to carrier degeneracy without having to resort to

[2] An alternative definition is to divide the doping by the minority diffusion constant inside the base: D_{nb}.

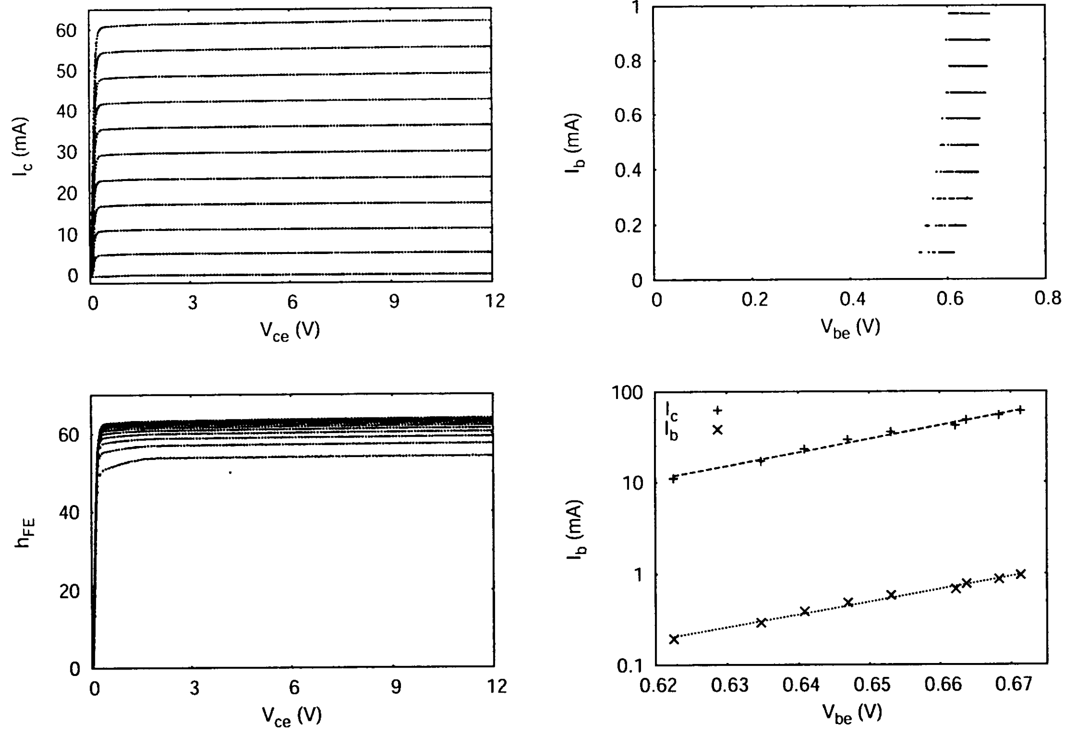

Figure 8-2: Transistor action plots of the NPN bipolar transistor TIP29C. top left: I_c vs V_{ce}, top-right: I_b vs V_{be}, bottom left: h_{FE} vs V_{ce}, bottom right: Gummel plot of I_c and I_b. The transistor was measured with the home-built curve tracer described in Appendix C.6.

the correct Fermi-Dirac statistics [105]. This changes the law of mass-action into [85]

$$n_i^2 = pne^{\frac{\Delta E_g}{kT}} \tag{8.9}$$

where ΔE_g is the artificial decrease in band gap that increases the intrinsic carrier concentration because of carrier degeneracy. Using the relation for ΔE_g from [106], its dependence on doping concentration (equal for both N- and P-type) is given in Fig. 8-4. As a consequence of the band gap narrowing, the current gain Eq. (8.7) is adjusted to

$$h_{FE} \rightarrow h_{FE0}e^{-\frac{\Delta E_{ge}-\Delta E_{gb}}{kT}} \tag{8.10}$$

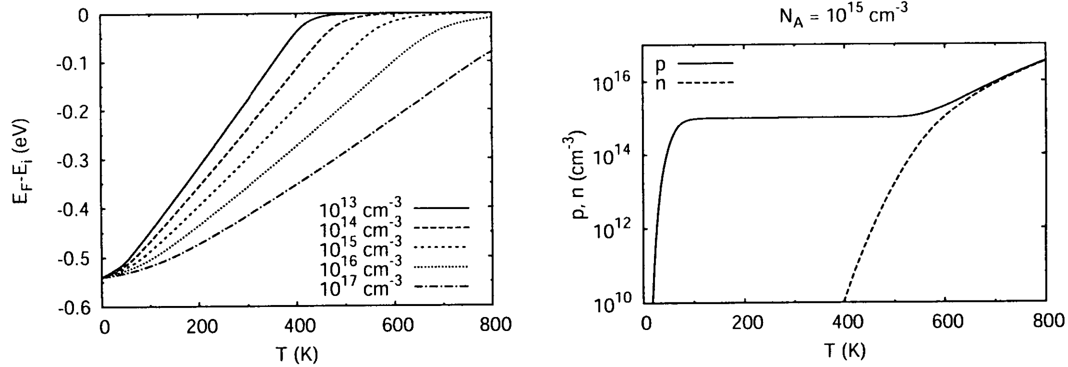

Figure 8-3: Fermi level (left) and carrier concentrations (right) as a function of temperature. The silicon is doped with boron with various concentrations for the left plot and with a concentration of 1×10^{15} cm^{-3} for the right plot. These plots have been generated following the standard model of [104] which takes into account carrier freeze out and intrinsic conduction, but neglects the temperature dependence of the effective masses and the band gap.

with ΔE_{ge} and ΔE_{gb} the band gap narrowing of the emitter and base, respectively, and h_{FE0} the original gain Eq. (8.7). Since the emitter is much more heavily doped than the base, this means that the band gap narrowing reduces the current gain. Because of the exponential temperature dependence, its effect becomes much more pronounced at low temperatures. Therefore, the current gain of a bipolar transistor at low temperatures is severely degraded.

8.2 Tunneling emitter bipolar transistor

The tunneling emitter bipolar transistor [107, 108, 109] belongs to the family of heterojunction tunnel transistors. Examples of this family include hot-electron transistors [87] and polysilicon emitters BJTs [85]. The transistor considered in this work is closely related to these transistors. It consists of a (ferromagnetic) metal emitter, separated from a silicon PN junction by a tunnel barrier. This kind of transistor was first devised by Kisaki [102]. A related device, called the tunnel emitter transistor has the same physical structure, except for the absence of a metallurgical base [110, 111]. For those transistors, the base is induced by the formation of a hole inversion layer

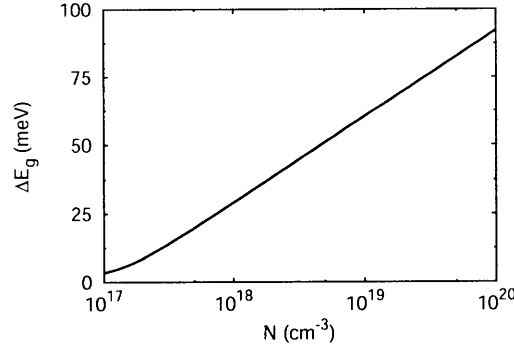

Figure 8-4: Apparent band gap narrowing as a function of doping concentration. The empirical relation can be found in [106] and holds for both N- and P-type silicon.

at the tunnel barrier-silicon interface. Subsequent studies of the tunneling emitter bipolar transistor [91] found that it exhibits a very large current gain, the cause of which remained however unclear. In the following the cause of the high gain is further illucidated and it is argued that the working of the transistor is actually similar to that of polysilicon emitter BJTs [112]. Namely, the tunnel barrier[3] suppresses the back-injection of holes into the emitter, thereby increasing the emitter injection efficiency. The reason why the back-injection is suppressed can easily be understood by considering the energy band diagram of the transistor in the active region, Fig. 8-5. With the transistor in the active region, electrons tunnel from the metal into the conduction band of the base. Electrons may however also tunnel into the valence band. For instance with a standard all semiconductor BJT, both conduction and valence electrons are emitted from the emitter. The current gain then results from the difference in doping profiles between emitter and base, yielding more emitter conduction electrons than valence band holes. Indeed, the current gain assuming zero recombination inside the base is given by the ratio of the doping concentrations, as in Eq. (8.7). Crucially for the tunneling emitter BJT however, the tunnel barrier height for tunneling into the valence band is higher than for tunneling into the conduction band by an amount equal to the band gap of the semiconductor. Therefore,

[3]For polysilicon emitter bipolar transistors the grain boundaries suppress the back-injection of holes.

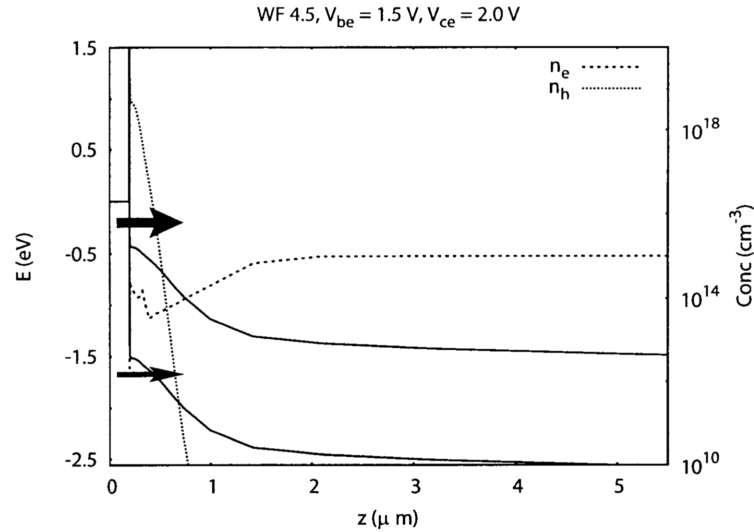

Figure 8-5: Energy band-diagram and carrier concentrations for a tunneling emitter bipolar transistor in the active region. The narrow vertical line indicates the tunnel barrier, here 20 Å thick. The thick and thin arrows indicate conduction band and valence band electron tunneling, respectively. This transistor has an implanted base with doping profile corresponding to the 120 nm implant oxide as described in Sec. A.2.

the tunneling of valence band electrons (and holes) is suppressed as compared to that of conduction electrons. This of course assumes that the tunneling is direct with conservation of perpendicular wave vector. Trap assisted tunneling because of tunnel barrier imperfections and/or interface states may cause additional tunneling into the valence band, thereby reducing the current gain of the transistor.

For increasing base-emitter biases, the bands are pulled down resulting in a further decrease in valence band tunneling and higher gain. This is the same mechanism that caused NDR in MIS diodes, as described in Chapter 7 and in [87]. Under ideal conditions, valence band tunneling will be negligible, as also shown in Appendix B.3. Consequently, the current gain of the transistor can reach enormous values since the only contribution to the base current can come from recombination inside the base. See for instance Chapter 2 where are shown simulation results of the tunneling emitter bipolar transistor. Interestingly, the efficiency of the spin-transfer across the base-collector junction was in Ch. 3 found to be determined as well by recombination

inside the base. Hence in the ideal case the current gain and spin-injection efficiency are directly related.

From the above discussion, it is obvious that the tunnel barrier is very important for the tunneling emitter BJT to have a high gain. The tunnel barrier is also important as an electrical isolation between emitter and base; without it, the energy bands of the base cannot be pulled down enough. As a result, electrons that tunnel into the conduction band will not drift but slowly diffuse through the base giving rise to significant recombination. This is similar to the reduction in gain for high current densities as described in Sec. 2.2 for which the base push-out straightens out the energy bands inside the base region (Kirk effect).

Finally, for spin-injection a good tunnel barrier is important as well as described in Chapter 1 since it is tunneling that links the current to the density of states of the ferromagnet.

With the importance of the tunnel barrier apparent, now the efforts can be described to fabricate a high-gain transistor, but first the influence of temperature on the tunneling emitter bipolar transistor needs to be discussed.

8.2.1 Temperature dependence of current gain

In Sec. 8.1.1 it was shown that band gap narrowing of the emitter severely degrades the current gain at low temperatures. It is to be expected that this fails to hold for the tunneling emitter bipolar transistor. Namely, since the emitter is a metal (hence degenerate), its carrier concentration will stay constant with temperature. Consequently, the current gain is expected to stay roughly constant with decreasing temperature[4]. The temperature independency is important for the ESR measurements (Chapter 5) that are performed at 100 K.

[4]Tunneling is only weakly temperature dependent, and recombination inside the base will decrease somewhat for decreasing temperatures.

8.3 Epiwafer transistors

The initial set of epiwafer transistors had a base and emitter contact as the left image of Fig. 6-3. The fabrication of these devices has been described in Sec. 6.1. IV characteristics of the base-emitter junction, together with their corresponding fit, are shown in Fig. D-4 and demonstrate that the tunnel barrier dominates in the forward bias regime, which solves the conductivity mismatch. The transistor plots are shown in Fig. 8-6. The Gummel plot in Fig. 8-6 shows the transistor in the active region

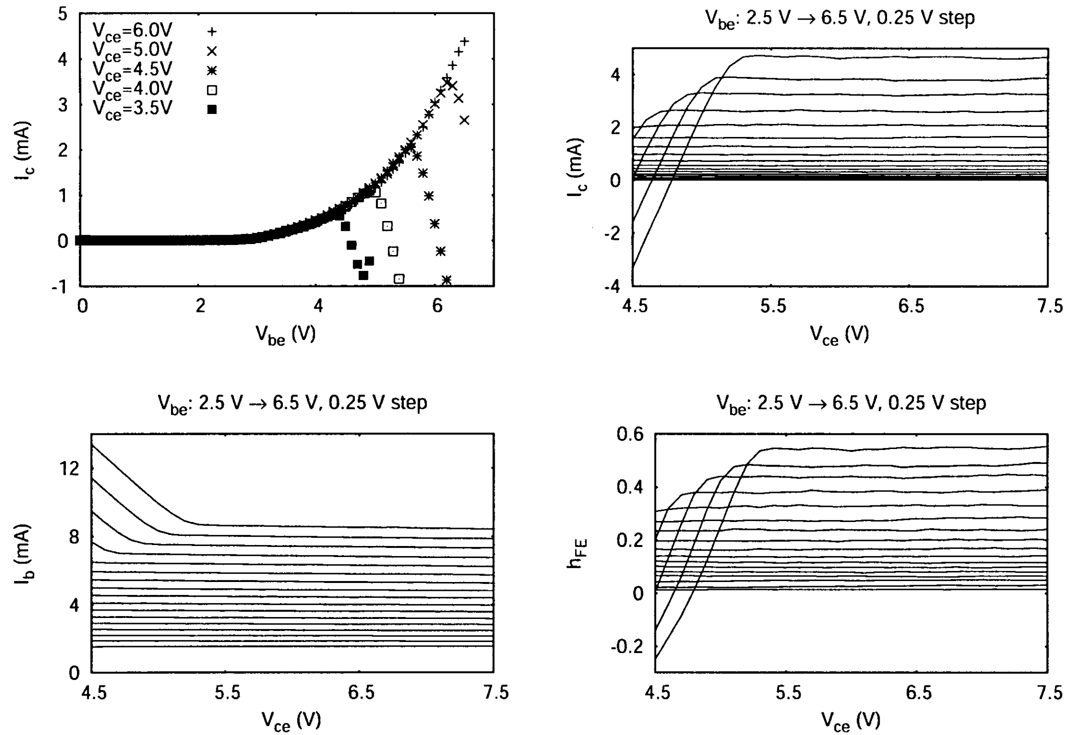

Figure 8-6: Transistor action of pn10mu_06; top left: Gummel plot of collector current, top-right: collector current for collector voltage sweep, bottom left: base current for collector voltage sweep, bottom right: corresponding current gain. The base width is 5.8 μm.

until the base-collector junction becomes forward biased, and the collector current reverses direction. The top right of Fig. 8-6 gives the collector current as a function of collector-emitter voltage V_{ce} and is clearly the expected output characteristic. The offsets in V_{ce} for increasing base-emitter voltages V_{be} are explained in Sec. 2.3. The

bottom row however, shows that the current gain of the transistor is very low. The low gain may be attributed to several reasons. For instance, there may be recombination happening inside the base which is rather thick, 6 μm for this transistor. Also, the contacts are quite far apart (100 μm) and the strips quite broad (200 μm), plus the base doping is very low (3×10^{15} cm^{-3}) which may cause current crowding and a lateral base current to flow. Also, there may be a surface current running between base and emitter contacts since the surface is not terminated with thermal oxide and may form a low-resistance leakage path; this was assumed in Sec. 7.1.4. Finally, the all-important tunnel barrier may be broken and of poor quality. For this transistor, it is likely to be a combination of all four causes and not a specific reason could be singled out easily.

In order to improve on the potential recombination inside the base, due to perpendicular or parallel transport through the base, the width of the base was thinned down much more, plus the base and emitter contacts were made narrower and brought closer together, as in the right of Fig. 6-3. Because of thinning down the base, the base-collector leakage current went up an order of magnitude (from 10 to 100 μA). Although by comparison with Fig. 6-1 the base should have been large enough to accommodate the depletion region, the RIE etch created some roughness resulting in variations in base widths across the device. Locally, the base width may therefore be less than the targeted value, inducing extra leakage. The transistor output characteristics of this device are shown in Fig. 8-7. Apart from the more erratic response as seen in Fig. 8-7, the gain is even lower than of the previous device. Clearly, recombination inside the base is not the main cause of the low gain. In order to find out the reason, the fabrication sequence had to be changed, as described in Sec. 6.2. Also the measurement set-up was improved significantly to enable much better and quicker device characterization.

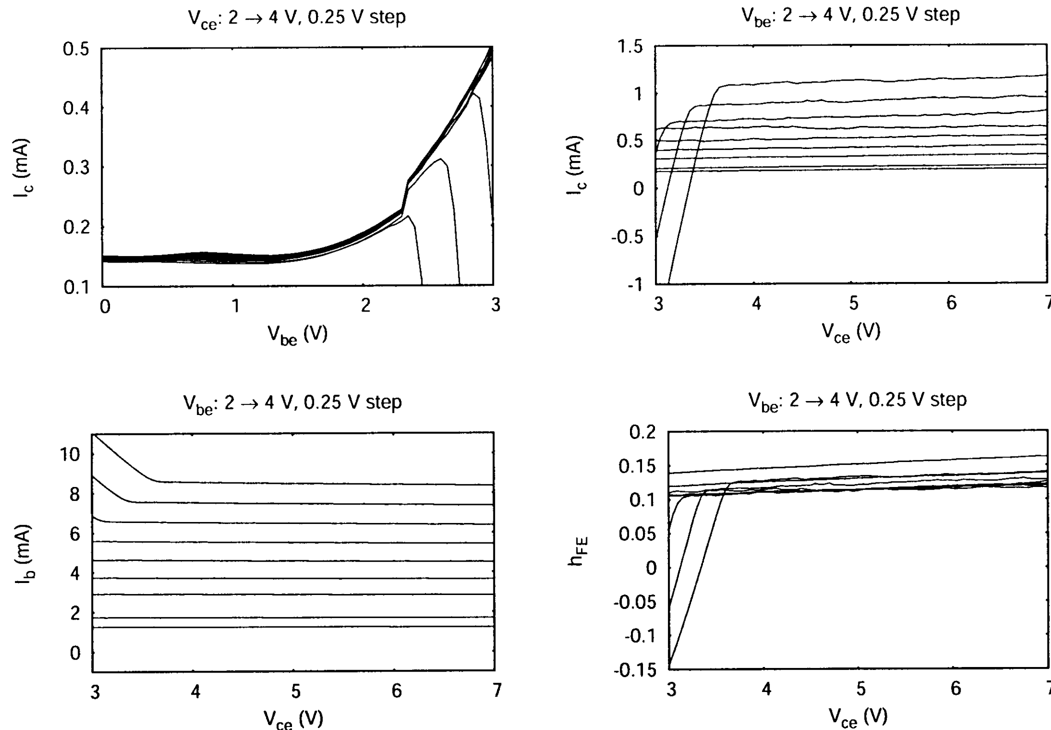

Figure 8-7: Transistor action of pn10mu_29; top left: Gummel plot of collector current, top-right: collector current for collector voltage sweep, bottom left: base current for collector voltage sweep, bottom right: corresponding current gain. The feature in the Gummel plot for low bias voltage is explained in Chapter 7; in fact, the NDTC feature of this device is shown in the top left of Fig. 7-5. The base width is 1.5 μm.

8.4 Implanted base transistors, emitter (1)

The implanted base fabrication steps have been described in Sec. 6.2. Here measurement results will be presented on those transistors with a similar emitter area and structure as the PN epiwafer transistors of Sec. 8.3. A schematic and image of the transistor are shown in Fig. 8-8. Measurements were performed with a home-built curve tracer[5] which is described in Appendix C.6. The measurements of three different devices are presented here in some detail since they offered the indirect proof that the tunnel barrier is the main cause of the low current gain, and also since they illustrate how the curve tracer enables one to readily extract the transistor parameters. These

[5]Designed by David Bono

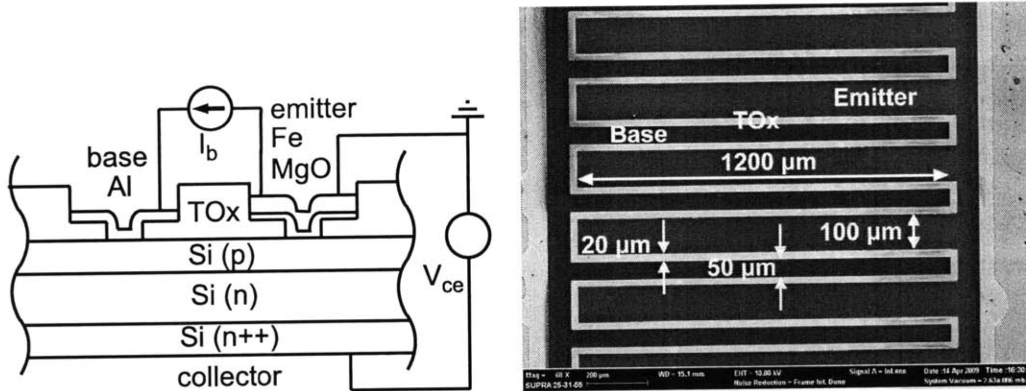

Figure 8-8: On the left is shown is a schematic of a cross-section of the tunneling emitter bipolar transistor on the wafer with the doping profiles and metal contacts indicated. In addition, the electrical connections are drawn. The right gives an SEM micrograph of device BJT_W06_P03_d02. The TOX in the image stands for thermal oxide and is the oxide through which ion implantation is done. At the very left and right side is the 1 μm thick thermal oxide. The whole back-side of the device forms the collector contact. A cross section of the device along the vertical axis of this image corresponds to the schematic shown on the left.

measurements were performed with the curve tracer and a room-temperature micro-probe station, see Appendix C.5 for a technical drawing of the latter. The devices differ only in implant oxide thickness with corresponding difference in base doping profile and base width W_b. The various doping profiles have been simulated with TSUPREM4, as described in Appendix A. The simulated base widths for the three devices are: BJT_W03_P03_d02 W_b = 2800 Å, BJT_W07_P01_bd01 W_b = 2350 Å, BJT_W06_P03_d02 W_b = 1000 Å.

The transistor actions were measured in the common emitter geometry with the emitter grounded[6], and the results for BJT_W03_P03_d02 and BJT_W07_P01_bd01 are shown in Fig. 8-9, and those for BJT_W06_P03_d02 in Fig. 8-10.

The gain h_{FE}, Eq. (8.4), of the transistors is very low, as observed from Figs. 8-9 and 8-10, and in the following it is argued that this is due to poor emitter injection efficiency and recombination inside the base.

Several parameters are readily extracted from the transistor action plots. The col-

[6]In reverse mode the transistors did not function, likely because of the leaky tunnel barrier.

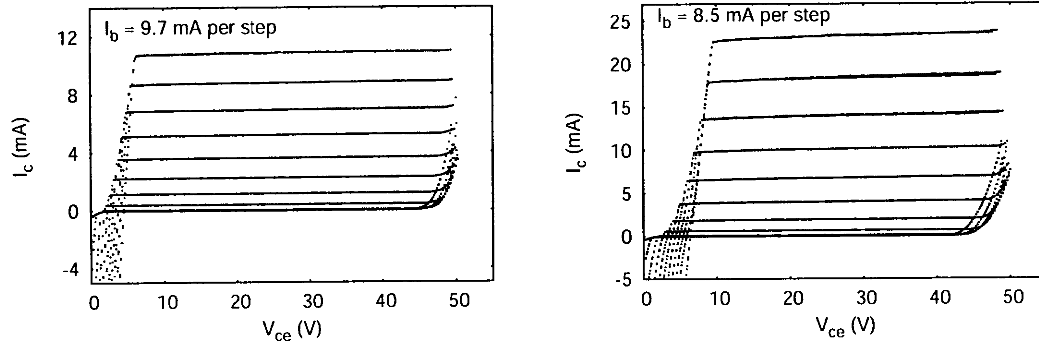

Figure 8-9: Transistor action of device BJT_W03_P03_d02 (left) and BJT_W07_P01_bd01 (right) in the common emitter geometry. Plotted is the collector current versus the collector-emitter voltage for different base currents with step-size 4.7 mA. The reason for the low current gain h_{FE} of approximately $0.1 - 0.2$ is explained in the text.

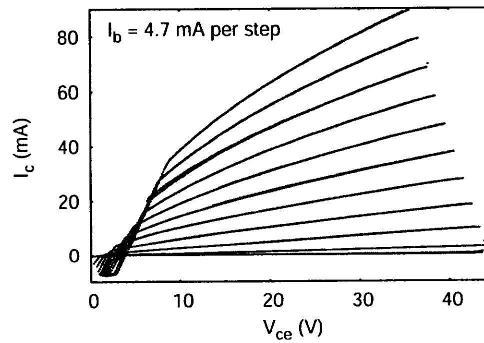

Figure 8-10: Transistor action of device W06P03d02 in the common emitter geometry. Shown is the collector current versus the collector-emitter voltage for different base currents with step-size 4.7 mA. The origin of the low current gain h_{FE}, only slightly above 1, is explained in the text.

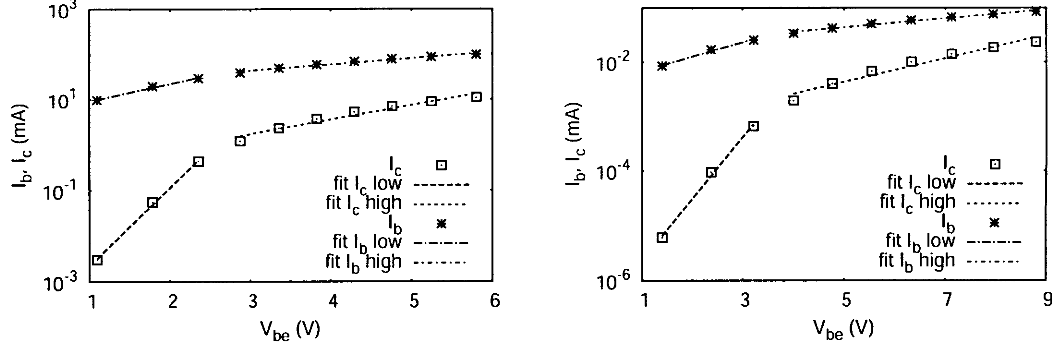

Figure 8-11: Collector and base current versus base-emitter voltage for device BJT_W03_P03_d02 (left) and BJT_W07_P01_bd01 (right) plotted on a semi-log scale. The median values of the currents are plotted to account for the variation with V_{ce}. A distinctive knee can be observed in the otherwise linear (on a log-scale) characteristics. The points below and above the knee are fitted separately which allows for the determination of the base resistance, as explained in the text.

lector resistance R_c is found from the initial slope and the Early voltage V_{early} from extrapolating the final slope to the crossing point with the negative V_{ce} axis. A handy feature of the curve tracer is that also the base voltage is being measured, and the current versus base-emitter voltage (V_{be}) characteristics are given in Figs. 8-11 and 8-12. The data in Figs. 8-11 and 8-12 reveal a distinctive knee in both the I_c and I_b versus V_{be} curves. Below and above the knee the data is well fitted with an exponential relation

$$
\begin{aligned}
I_c &= I_{c0} e^{\alpha_c V_{be}} \\
I_b &= I_{b0} e^{\alpha_b V_{be}}.
\end{aligned}
\tag{8.11}
$$

The point of inflection is a result of the finite base spreading resistance; I_b flows laterally and creates a voltage drop across the base. The base voltage measured therefore effectively increases for the same amount of I_b (since the base is hooked up to a current source). The knee therefore defines the onset of a significant lateral current flow. The base resistance (R_b) can be extracted by calculating the distance from the I_b data points to what the below-the-knee fit would give[113, 114], as plotted in Fig. 8-13 for BJT_W06_P03_d02. Since R_b introduces an extra voltage drop which

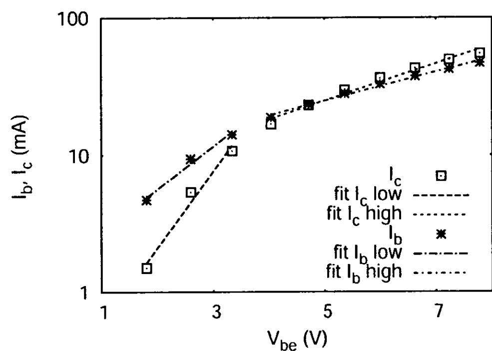

Figure 8-12: Collector and base current versus base-emitter voltage for device BJT_W06_P03_d02 plotted on a semi-log scale. The median values of the currents are plotted to account for the variation with V_{ce}. The points below and above the point of inflection are fitted separately from which the base resistance can be derived, as explained in the text.

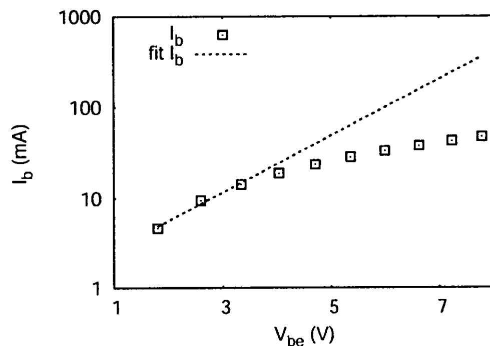

Figure 8-13: Base current versus base-emitter voltage for device BJT_W06_P03_d02 plotted on a semi-log scale, together with a fit to the data below the knee. The base resistance can be extracted from the difference between the fit and the data.

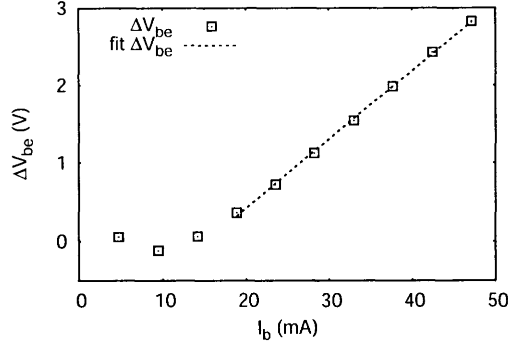

Figure 8-14: Base voltage drop against base current due to lateral current flow for device BJT_W06_P03_d02. The data is well fitted with a straight line and the slope equals the base resistance. The lowest three points that straddle around zero voltage were the ones used to generate the fit to the base current below the knee and are plotted here for completeness.

does not appear across the emitter-base junction, the effective V_{be} is reduced by

$$\Delta V_{be} = I_b R_b. \tag{8.12}$$

Hence the difference between the data and the fit of Fig. 8-13 gives R_b. ΔV_{be} has been plotted in Fig. 8-14. The plot in Fig. 8-14 is well fitted with a straight line whose slope equals R_b, for this device found to be $R_b = 88\ \Omega$. In principle, there is another contribution to ΔV_{be}, namely due to the finite emitter resistance (R_e), i.e.

$$\Delta V'_{be} = I_b R_b + I_e R_e. \tag{8.13}$$

Since the input resistance of the tunneling emitter bipolar transistor includes the MgO tunnel barrier, the contribution from the emitter resistance R_e may be significant. However, from Fig. 8-14 it is observed that the relationship between voltage and current is perfectly linear over a certain current range whereas a tunnel barrier would introduce a nonlinear component. It can therefore be concluded that the tunnel barrier is leaky and does not significantly impede current flow[7]. By the same token,

[7]The base-emitter IV characteristics, not shown here, are somewhat nonlinear, attributable to the Schottky barrier, but straighten out for the large biases (V_{be}) for which data is presented here.

Table 8.1: This table lists the extracted transistor parameters of the measured devices.

	BJT_W03_P03_d02	BJT_W07_P01_bd01	BJT_W06_P03_d02
W_b (Å)	2800	2350	1000
R_c (Ω)	172	254	247
V_{early} (V)	867	467	10
R_b (Ω)	32	65	88
α_{bl}	0.88	0.61	0.72
α_{bh}	0.31	0.19	0.24
α_{cl}	3.9	2.6	1.3
α_{ch}	0.74	0.50	0.40
α_{cl}/α_{bl}	4.4	4.3	1.8
α_{ch}/α_{bh}	2.4	2.6	1.7

also current crowding effects do not play a role since those would make R_b dependent on current[115].

Using exactly the same scheme also the data of the other devices are analysed and all the results are summarized in Table 8.1. The parameters in Table 8.1 can be understood from the influence of variation of W_b on the transistor action. First, as given in Table 8.1, the (average) V_{early} rapidly decreases with decreasing W_b as is evident from Fig. 8-10, because of base-width modulation. The (average) R_c also differs between devices but not due to differences in base width but most likely as a result of parasytic resistance differences. From Table 8.1 it can also be observed that R_b increases with decreasing W_b, again as expected since the spreading resistance component of R_b is inversely proportional to W_b. The slope of $\ln I_c$ (Eq. 8.11), α_c over the slope of $\ln I_b$, α_b, has been listed as well in Table 8.1, both for below (subscript l) and above (subscript h) the knee point. A dramatic change is observed for the devices BJT_W03_P03_d02 and BJT_W07_P01_bd01 whereas this ratio changes only slightly when crossing the knee for BJT_W06_P03_d02. The root cause of the difference in the change of the ratio is the lateral current flow in the base; above the knee the minority current inside the base has a lateral component and due to the relatively

heavily doped base and/or insufficient post-ion implantation annealing (to restore crystallinity), this current component recombines readily, consequently decreasing the amount of I_c compared to I_b. The lateral current for BJT_W06_P03_d02 is however much less because of the very thin base. It can then be concluded that this component of the lateral current flows through the bulk of the base, and not via the interface. The fact that above the knee also the slope of I_b is less than below is, as described earlier, due to the finite base voltage drop, decreasing the effective voltage seen across the base-emitter junction. Finally, one more observation can be made from Table 8.1, namely that the difference in current gain between the devices below the knee (approximately a factor of 10) is due to recombination in the base for perpendicular current flow[8], and moreover, that the large I_b below the knee for all the devices must be the result of recombination processes at the base-MgO interface.

The detailed analysis of the first round of implanted base transistors revealed that the main cause of the low current gain is recombination at the tunnel barrier-silicon interface. This may be due to defect states resulting from a damaged tunnel barrier or a contaminated surface that may induce trap assisted recombination. From these findings it was concluded to improve the fabrication sequence as described in Sec. 6.3.2. The changes that were made include: define the emitter before the base, reduce the emitter area, and switch to different tunnel barrier oxides. The emitter metal had to be changed as well in order to be compatible with cleanroom procedures since devices were now finished completely within the shared facilities.

These improvements worked out well and led to the first direct proof that the tunnel barrier is crucial for the making a working device and is vulnerable to damage. These improvements are described next.

[8]It could also result from the different surface doping concentrations with corresponding defect states. However, the behavior of BJT_W03_P03_d02 and BJT_W07_P01_bd01 is very similar whereas their surface concentration differs significantly; therefore the recombination inside the base is likely to be the main cause.

8.5 Implanted base transistors, emitter (2)

As described in Sec. 8.4, the implanted base transistors still suffered from a low current gain. The measurements revealed that the cause is recombination at the tunnel barrier-silicon interface. Hence the emphasis was placed on improving the tunnel barrier and emitter in general. The change in fabrication sth2.eps is described in Sec. 6.3.2. Here several measurements are presented that conclusively prove the cause of the low gain. Consider Fig. 8-15. For low base currents and low collector-emitter voltages (V_{ce}) the transistor displays a high gain, about 10 in the top row in Fig. 8-15. It is observed however that the collector current I_c has not saturated yet, reflected in the curves that bend upward, and I_c continues to rise with V_{ce}, as shown clearly in the 2nd row. In fact, for large enough V_{ce} the base current drops to 10 nA which is the leakage current of the curve tracer. At the same time, I_c shoots up indicated by the branches bending upward. Upon further increase of V_{ce} however, I_c collapses and the base-emitter voltage drops, which is depicted in the 3rd row. This is caused by breakdown of the tunnel barrier. For higher biases with the broken tunnel barrier as shown in the 4th row of Fig. 8-15, the output characteristics resemble the ones of Sec. 8.4. These figures give direct proof that the faulty tunnel barrier is the cause of the low gain[9]. Furthermore, it provides evidence of the working of the transistor, namely, that tunneling into the valence band is suppressed by the (intact) tunnel barrier. It does not result from the existence of an inversion layer, since at the applied base-emitter biases, the potential inversion layer has all but disappeared. This holds even more so considering the work function of the emitter metal WN, which is at least 4.6 eV.

The transistor output characteristics for an aluminum emitter are shown in Fig. 8-16. Again, the gain is so high that the full transistor action plot cannot be measured before the device breaks down[10]. Now the question of the low gain has been transformed

[9]It should be noticed this result was obtained by virtue of the home-built curve tracer which measures 50 × per sec the transistor output and is able to capture the high gain stage before the transistor breaks down.

[10]The home-built curve tracer can only measure the transistor in the common-emitter geometry. It is expected that in the common-base geometry the full transistor curve can be obtained. This limitation of the measurement setup does not prevent however from reaching the important conclusions

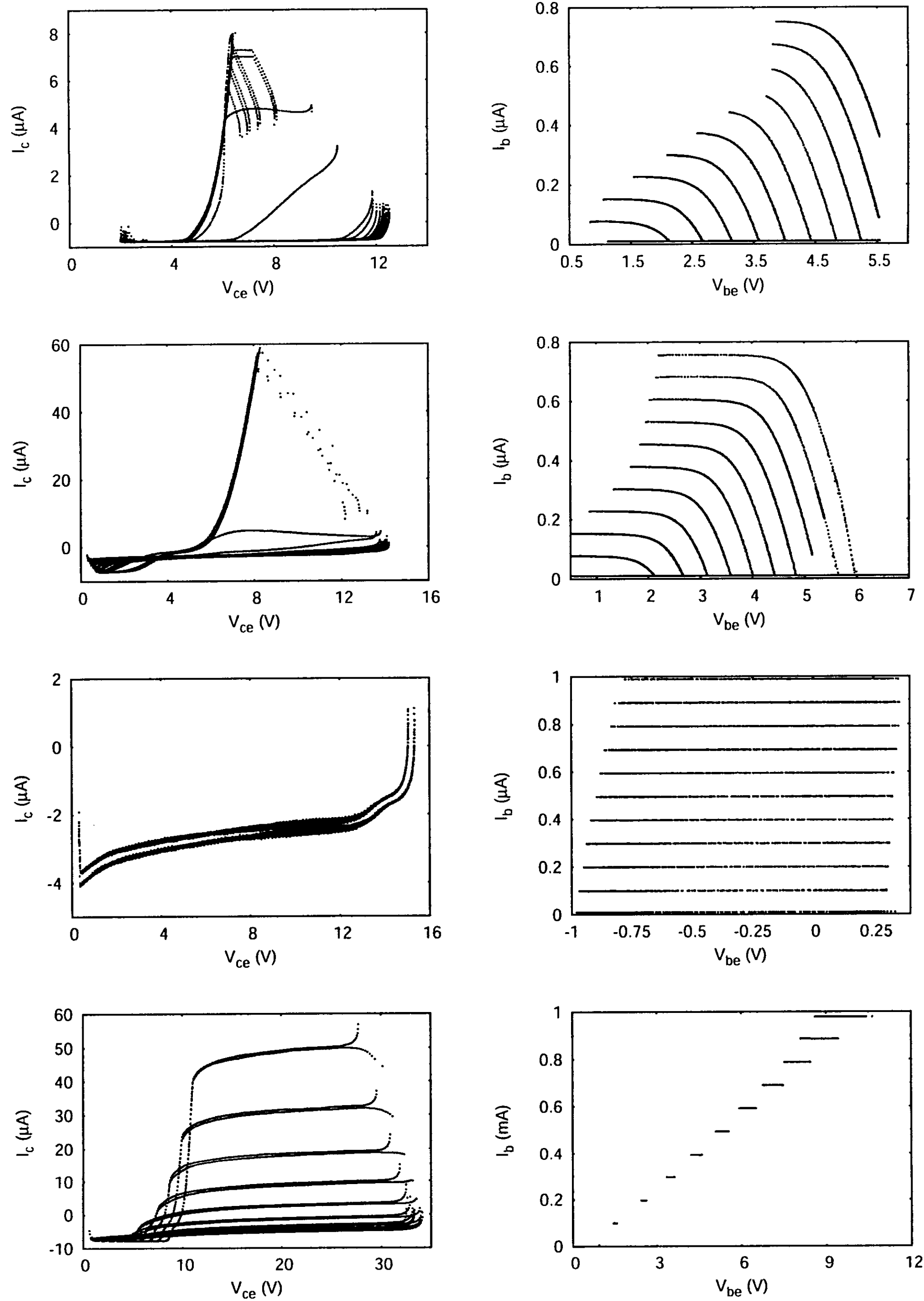

Figure 8-15: The collector (left) and base (right) current versus collector-emitter, respectively, base-emitter voltage for device BJT_W14_P04_j_d01_es02. The upper 2 rows are with the tunnel barrier intact, in the 3rd row the tunnel barrier is just broken, and the 4th row gives the output characteristics of the transistor with a broken tunnel barrier for higer biases. The tunnel barrier consists of 20 Å of dry thermal oxide, and the emitter of 500 Å WN, grown with ALD. The emitter area is 3.2×10^{-3} cm^2.

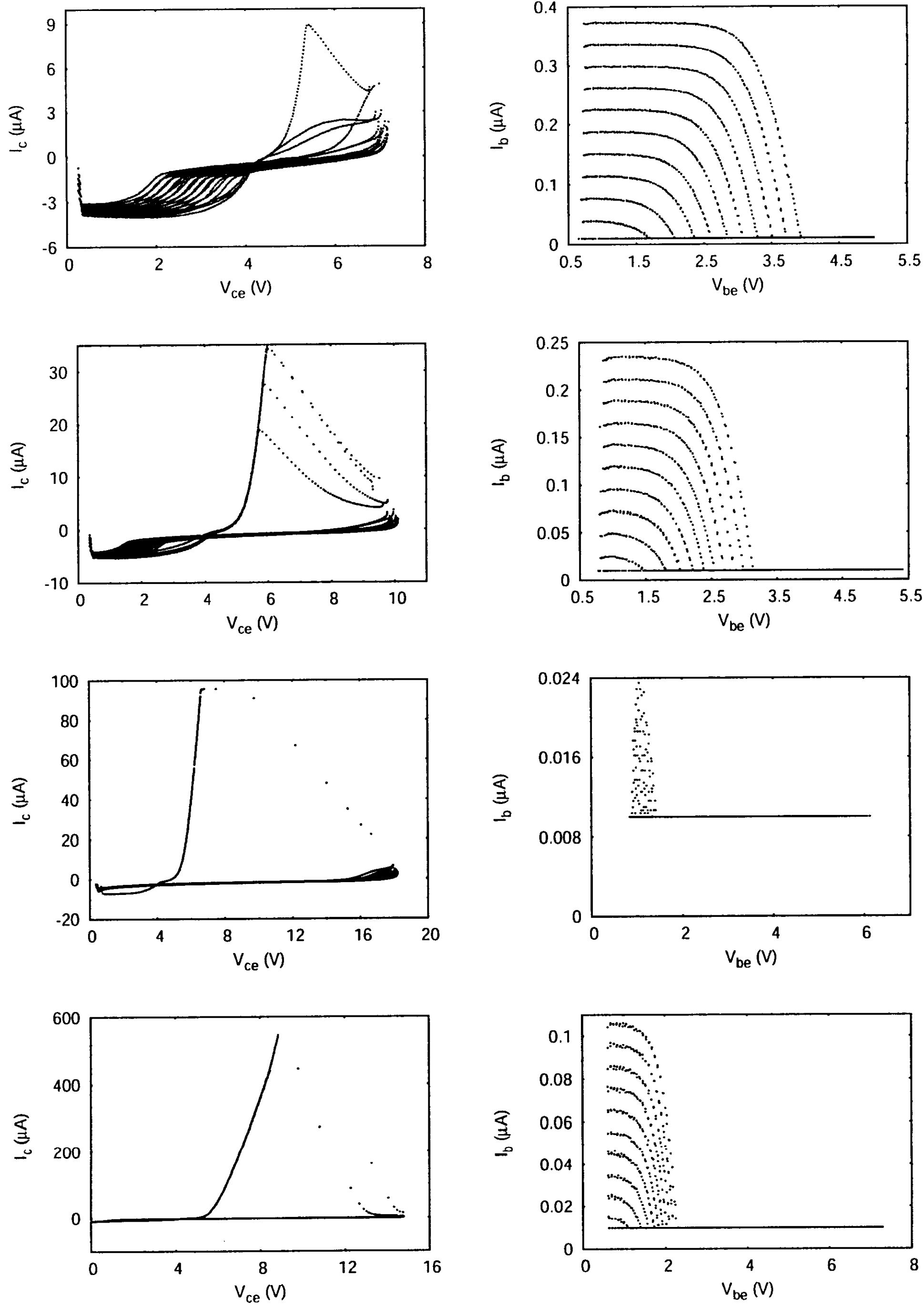

Figure 8-16: The collector (left) and base (right) current versus collector-emitter and base-emitter voltage, respectively, for device BJT_W15_P02_d_d03_ees01. The tunnel barrier consists of 20 Å dry thermal oxide, and the emitter of 900 Å Al, deposited with a thermal evaporator. The emitter area is 3.2×10^{-3} cm^2.

into what causes the collapse of the tunnel barrier. The maximum current density for this device would be 0.3 A/cm^2 which is much lower than expected to cause breakdown. Also, both the transistor action for the WN and the aluminum emitter display qualitatively the same features. Consequently, it is not likely that the breakdown is caused by the choice of emitter metal (because of interdiffusion) and also not by the deposition method since both ALD and thermal evaporation are low-energy deposition methods[11]. Therefore, the main reason for dielectric breakdown must be the dielectric itself. Apparently, the thermal oxide does not grow uniformly resulting in local hot-spots where the current is concentrated. At those places the current density may reach values above the critical density. The non-uniformity may stem from the growth conditions; the tunnel barrier was grown at 850°C for 6 min. It may be better to lower the temperature and increase the oxidation time in order to reach the square-root growth rate, see Fig. A-1, such that thickness variations will be more suppressed. Another solution is to switch to a different, more homogeneous oxide, for instance Al_2O_3 grown by ALD. Results for those transistors are given in Fig. 8-17. The ALD grown Al_2O_3 did not yield very high gain transistors, observable in Fig. 8-17, which is yet another proof though that the tunnel barrier really determines the transistor characteristics. Noticeable as well is that the transistor action looks much cleaner and stable than before. The tunnel barrier stills breaks down above a certain V_{be}, with accompanying loss in I_c, however, up to this breakdown the transistor behaves very stable, indicating that the tunnel barrier is intact. The maximum gain before breakdown hovers around 1.4 and is shown in Fig. 8-18. What then causes the low gain, or, by the same token, the large base current? It may be that the tunnel barrier height of ALD grown Al_2O_3 is not high enough to significantly impede valence band tunneling or, more likely, that there is trap assisted tunneling into the valence band. The latter cause may be mitigated by annealing the transistor in a hydrogen atmosphere in order to passivate the dangling bonds of the silicon surface atoms.

---

about the tunnel barrier.

[11]Sputtering of aluminum (which is a high-kinetic energy process) on top of thermal oxide was also tried yielding similarly working devices. Ebeam evaporation was not tried, considering the findings of Chapter 10, i.e. the charge built-up caused by the stray electrons may induce in-situ breakdown.

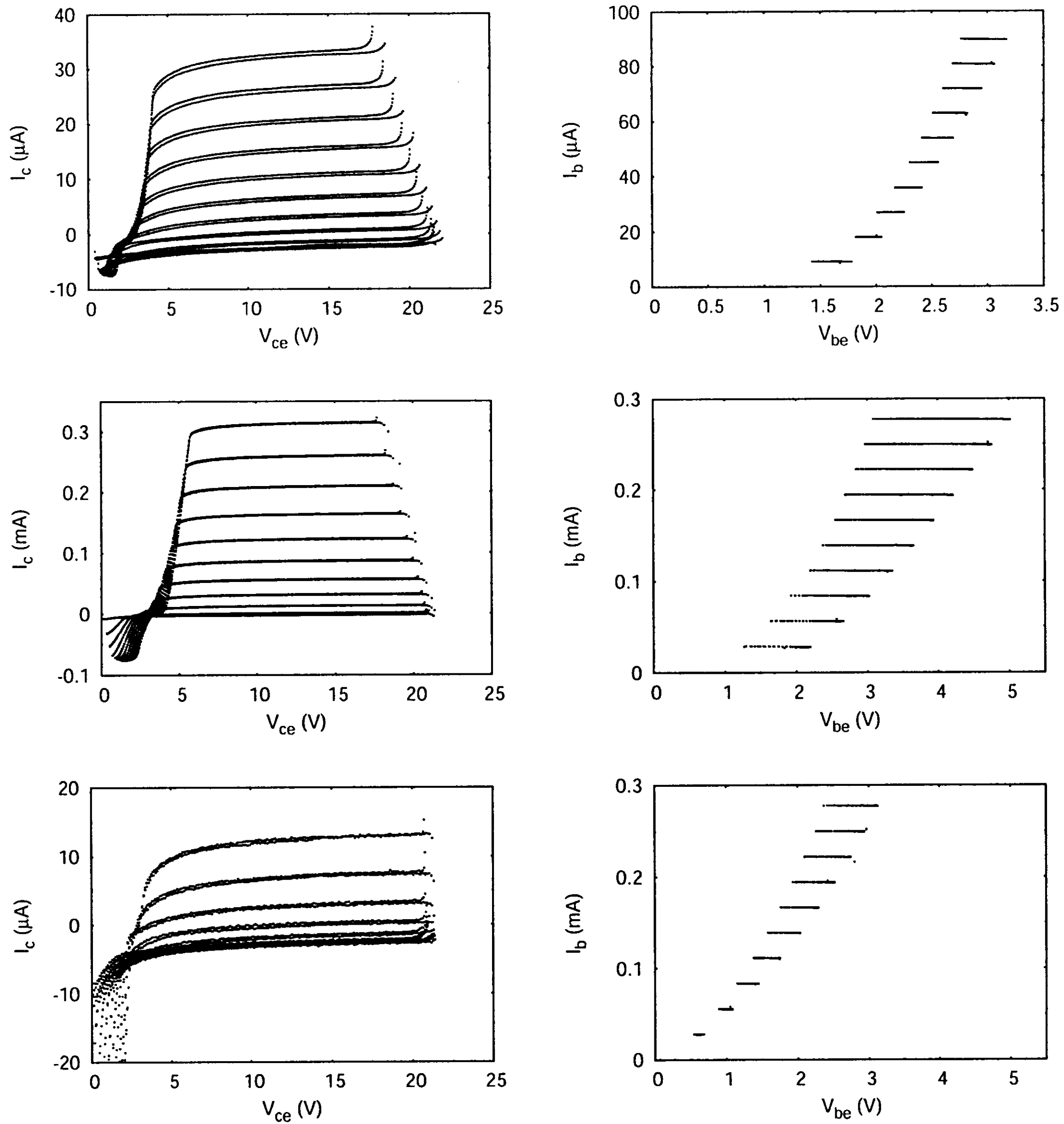

Figure 8-17: The collector (left) and base (right) current versus collector-emitter respectively base-emitter voltage for device BJT_W15_P03_i_d01_eep05. The upper 2 rows are with the tunnel barrier intact, in the 3rd row the tunnel barrier is just broken, although not completely as seen from the V_{be} value. The tunnel barrier consists of 18 Å Al_2O_3, and the emitter of 500 Å WN, both grown with ALD, in-situ. There is likely a very thin (3 AA) SiO_2 layer beneath the Al_2O_3 because of the time it takes to mount into the ALD after the RCA cleaning. The emitter area is 2.9×10^{-4} cm^2.

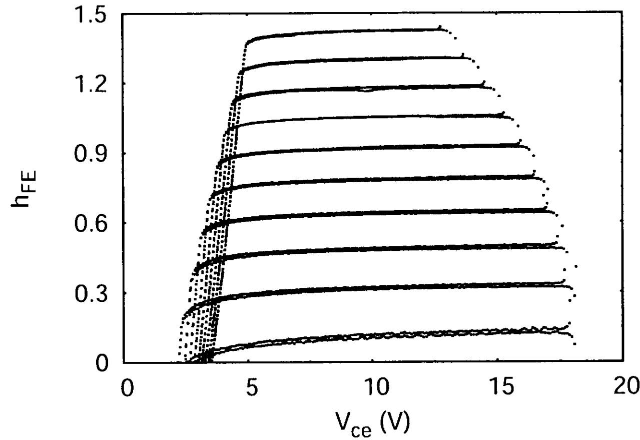

Figure 8-18: Current gain of device BJT_W15_P03_h_d02_eep03. The tunnel barrier consists of 18 Å Al_2O_3, and the emitter of 500 Å WN, both grown with ALD, in-situ. There is likely a very thin (3 AA) SiO_2 layer beneath the Al_2O_3 because of the time it takes to mount into the ALD after the RCA cleaning. The emitter area is 2.9×10^{-4} cm^2.

Despite the low gain, the transistor with the ALD grown Al_2O_3 barrier is stable and reproducible. In fact, the nonnegligible base current stabilizes the transistor; the little I_b in the case of the SiO_2 barrier made the device hard to control. This transistor is a clear improvement compared to the MgO based transistors of Sec. 8.4 (compare with Fig. 8-9), not only because of the higher gain, but also since the transistor operates with an intact tunnel barrier, see for instance Sec. D.2.3 where are given the base-emitter IV characteristics.

The Al_2O_3 transistor is also measured at cryogenic temperatures, with the outcome, together with room temperature measurements, given in Fig. 8-19. That the transistor works just as well at low temperatures is observable from Fig. 8-19. The gain at low temperatures still has the same order of magnitude, which is a clear indication that band gap narrowing, as described in Sec. 8.1.1, does not play a role for the tunneling emitter bipolar transistor, in agreement with the predictions in Sec. 8.2.1. The flat temperature dependence has also been observed before in tunnel emitter transistors [111]. Besides its good behavior at low temperatures, the device of Fig. 8-19 can also withstand a current density of 1 A/cm^2 which is enough to have a sig-

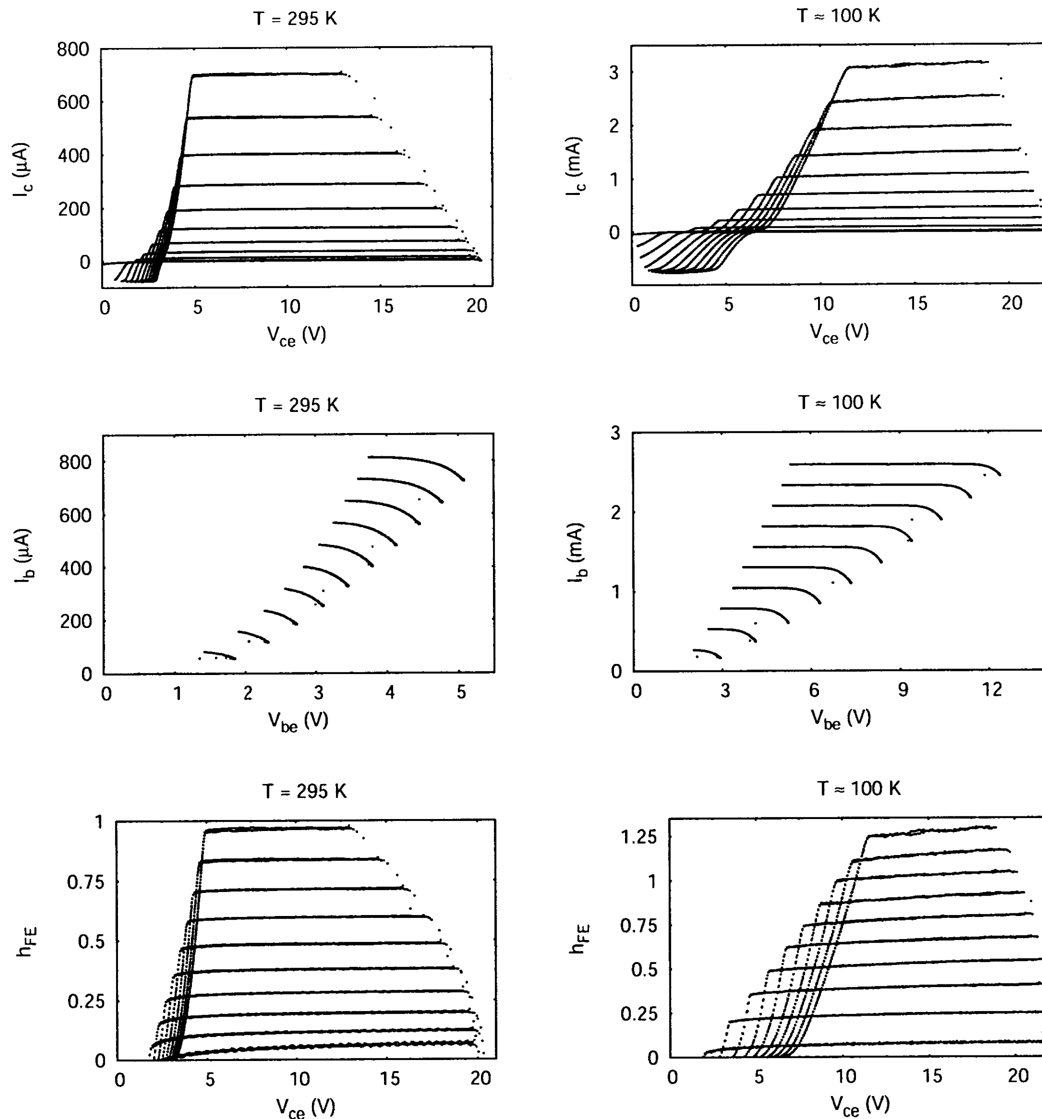

Figure 8-19: The collector current (top row), base current (middle row), and current gain (bottom row) for device BJT_W15_P03_g_d04. The left column is measured at room temperature (T = 295 K), the right column at approximately 100 K. The increase in collector resistance at low temperature, as seen from the initial slope of the I_c vs V_{ce} characteristic, causes the offset in V_{ce} for increasing V_{be}. The tunnel barrier consists of 18 Å Al_2O_3, and the emitter of 500 Å WN, both grown with ALD, in-situ. The emitter area is 3×10^{-3} cm^2.

nificant influence on the ESR signal (see Eq. (5.6)).

In conclusion, the tunneling emitter bipolar transistor exhibits a large current gain as long as valence band tunneling is suppressed. A good tunnel barrier will suppress valence band tunneling, yielding transistors with record-size gains. The gain of the transistor is largely independent of the temperature, making the device potentially useful for cryogenic applications, but which is important as well in light of the ESR measurements that are performed at T = 100 K. The emitter work function has little influence on the transistor characteristics and the transistor should therefore work equally well with a ferromagnetic emitter. If the tunnel barrier would block valence band tunneling completely, then the gain of the transistor would be directly correlated to the spin-injection efficiency since all the electrons from the emitter end up in the conduction band of the base of the transistor and are subsequently swept into the collector. The current densities that can be reached with the devices described in this Chapter are already large enough to have an effect on the ESR signal, when changed to a ferromagnetic emitter. Fine tuning of the tunnel barrier fabrication however, will allow the fabrication of much more robust devices with accompanying larger current densities and better device performance.

Chapter 9

The influence of spin-polarization on the $h/2e$ and h/e oscillations of ring-structures in the presence of the Rashba Spin-Orbit Interaction

In the study below it is shown that the spin-polarization of the current influences the $h/2e$ and h/e oscillations in the conductance of ring-structures in the presence of the Rashba Spin-Orbit Interaction (SOI). The spin-interference pattern of ring-structures is calculated for the combined effect of the Rashba SOI and applied magnetic field and the influence of the coupling of the spin to the applied magnetic field on the h/e oscillations for both unpolarized and polarized current is presented. It is argued that the $h/2e$ and h/e interference patterns can be used to probe the spin-polarization of the current. In addition, the coupling of the spin with the magnetic field is taken into account and shown to modulate the interference pattern differently for unpolarized and polarized current.

9.1 Introduction

The Rashba spin-orbit interaction (SOI) [38, 116] has a marked influence on the conductance of ring-structures fabricated out of the two-dimensional electron gas (2DEG) of a semiconductor quantum well structure. The self-interference of electrons travelling through a ring-structure in the presence of a perpendicular magnetic field gives rise to Aharonov-Bohm (AB) oscillations[117] in the conductance since the clockwise (cw) and counter-clockwise (ccw) travelling waves pick up different phases because of the encircled magnetic flux. Also the SOI may induce interference in ring-structures, known as the Aharonov-Casher (AC) effect[118], which results from the different spin-precessions of the cw and ccw travelling waves around the effective magnetic field whose direction depends on the travel direction. Recently, the AC effect in ring-structures has been observed in two independent experiments[119, 120] both of which demonstrate that the self-interference of electrons in ring-structures subject to the Rashba SOI can be manipulated with a gate-voltage, as shown theoretically in [121, 122, 123, 124, 125, 126, 127].

In this Chapter the influence of the spin-polarization of the current on the conductance interference patterns of ring-structures subject to the Rashba SOI is calculated and it is shown that the spin-polarization of the current changes the interference patterns considerably which can therefore be used to demonstrate the spin-polarization. The primary device structure corresponding to the calculations is shown in Fig. 9-1. It consists of a 1D ring connected to two leads aligned along the $\hat{x}$-direction. This

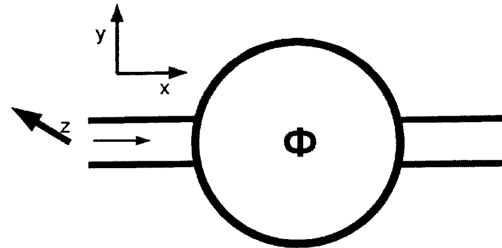

Figure 9-1: Ring with leads in the presence of the Rashba spin-orbit interaction and a perpendicular applied magnetic field. The magnetic field flux in the ring is ϕ. A spin wave polarized in the $\uparrow_z$ direction is shown entering the ring from the left.

ring-structure is fabricated out of the 2DEG of a semiconductor heterostructure and because of the asymmetric quantum well (induced for instance by an asymmetric doping profile) electrons inside the ring are subject to the Rashba SOI. The electronic current enters the ring from the left and results will be derived for the two cases that it is spin-unpolarized and spin-polarized with initial $\uparrow$ spin along the $\hat{z}$-direction, denoted by $\uparrow_z$. The precise results for the spin-polarized current obtained below will depend on the exact polarization direction of the initial current which has been chosen here somewhat arbitrarily as $\uparrow_z$. However, the main conclusions reached will be independent of the choice of polarization direction.

The two main oscillations in the conductance of ring-structures are the $h/2e$ and h/e AB oscillations corresponding, respectively, to electrons encircling the ring fully (round-trip) or only half before interfering [128, 129]. It is well understood and observed that the $h/2e$ oscillations will wash out rapidly with increasing applied magnetic field strength whereas the h/e oscillation will survive even for very large field [130]. The direct influence of the magnetic field on the spin via the Larmor precession has been treated perturbatively for weak magnetic fields in [131]. In [132] its influence was investigated numerically and it was shown that the Larmor precession contributes to the overall spin-precession for larger magnetic fields. Below, the spin-precession about the total effective magnetic field consisting of the Rashba effective magnetic field[1] and an applied magnetic field is calculated *analytically* for a 1D ring and the distinct h/e oscillations for an unpolarized and a polarized currents are presented over a large magnetic field range and can be used as well to clearly demonstrate the polarization of the current.

9.2 Rashba induced interference in ring-structures

The conductance of ring-structures in the presence of the Rashba SOI has been the subject of extensive research [121, 122, 124, 133, 134, 135, 136]. A common approach

[1]Only the Rashba SOI will be considered which is valid for the samples as used in the experiments of [119, 120]. However, the case for solely a Dresselhaus SOI is identical by making a suitable transformation.

taken to solve for the ring-conductance is to derive the eigenfunctions of the ring which are then connected via scattering matrices to the eigenfunctions in the external leads [124, 125]. In this way the conductance for rings with a tunnel-barrier inside an arm of the ring, i.e. a weakly broken ring, was derived[126] and shown to be able to yield a spin-polarized current. Rings subject to the Rashba SOI have also been shown to manipulate spin and can be used to change the polarization of the initial current[122, 127]. However, the connection of the initial polarization of the current to the $h/2e$ and h/e interference patterns has not been investigated until the present work. Making such a connection below, it will be shown that the ring can be used as a spin-*detector*, i.e. the conductance oscillations of the ring can probe the spin-polarization of the current.

The approach taken to calculate the interference patterns for spin-(un)polarized current is to derive the full quantum-mechanical rotation a spin undergoes while traversing the ring. Then, the interference intensity of the spin-wave function can be calculated from the coherent superposition of the counterclockwise (ccw) and clockwise (cw) travelling parts. An AB phase difference between the ccw and cw parts is included, then the modulation of the AB oscillations by the Rashba SOI induced interference can be used to measure the interference patterns. To first order, the $h/2e$ AB conductance oscillation (corresponding to round-trip traversal of the ring) will be inversely proportional to the backscattered interference intensity, whereas the h/e AB conductance oscillation (i.e. half-way traversal of the ring) will be proportional to the interference intensity half-way. The approach taken in this Chapter has been employed previously in [123]. Here, however, it is generalized for an initial spin-polarization. Furthermore, the direct coupling of the spin to a finite perpendicular magnetic field is explicitly taken into account and its effect on the h/e oscillations will be investigated. This has not yet been calculated analytically in literature. The motional plane will be chosen to be the $\hat{x} - \hat{y}$ plane, the 2DEG of a semiconductor heterostructure. The entrance and exit leads of the ring will be taken along the $\hat{x}$-direction.

9.2.1 Counter-clockwise rotation for the circle

Previously[123] the rotation of the spin around the Rashba effective magnetic field while travelling along any regular polygon, including the circle, was calculated analytically. The effect of the magnetic field on the spin was however neglected. To take into account the influence of the applied magnetic field on the spin, the direction of the total effective magnetic field $\vec{B}_{eff}$ about which the spin precesses when travelling along a polygon-side should be written as

$$\begin{aligned} \vec{B}_{eff} &= s_R \begin{pmatrix} \sin\beta_k \\ -\cos\beta_k \\ 0 \end{pmatrix} + s_H \begin{pmatrix} 0 \\ 0 \\ 1 \end{pmatrix} \\ s &= |\vec{B}_{eff}| = \sqrt{s_R^2 + s_H^2} \\ \beta_k &= \frac{2\pi k}{n} \end{aligned} \tag{9.1}$$

with s_R the precession angle due to the Rashba SOI, s_H the precession angle due to the applied magnetic field $\vec{H} = H_z$, s the total precession angle about the direction $\vec{B}_{eff}$, and β_k the angle which defines the side k of the n-sided regular polygon. The precession angles s_R and s_H in the expression Eq. (9.1) for the rotation direction $\vec{B}_{eff}$ serve as weight values that determine the relative importance of the Rashba and Larmor contribution to $\vec{B}_{eff}$. In Eq. (9.1) the Rashba effective magnetic field has been chosen in-plane which is the case for a [001] oriented two-dimensional electron gas (2DEG) as for instance the InAlAs/InGaAs heterostructures of Ref. [120]. The exact results obtained below for the rotation matrices will be different for other 2DEG orientations, but qualitatively the derived conclusions will continue to hold.

While traversing the polygon, the spin will precess about the effective magnetic field of Eq. (9.1), whereas the latter will change direction with changing polygon sides. Because of the continuous spin-precession, the orientation of the spin will in general be different after a full traversal of the polygon, even though the effective magnetic field returns to its original direction. Also, the final spin-direction will depend on whether the polygon is traversed counterclockwise or clockwise since the correspond-

ing precessions differ in general, which is the very reason for the interference patterns derived below.

The rotation of the spin along a polygon-side k, formally written as R_k, can be decomposed into Euler rotations about the $\hat{z}$- and $\hat{y}$-directions: $R_k = R_z(\varphi)R_y(\theta)R_z(\psi)$ with the Euler angles given by

$$\begin{aligned}\varphi &= \beta_k + \varepsilon \\ \psi &= -\beta_k + \varepsilon \\ \theta &= 2\arccos\left(\frac{\cos\frac{s}{2}}{|\cos\varepsilon|}\right) \\ \varepsilon &= \arctan\left(\frac{s_H}{s}\tan\frac{s}{2}\right).\end{aligned} \tag{9.2}$$

Rotations along successive polygon-sides partially cancel each other and the total counter-clockwise rotation along the complete polygon takes the form

$$\begin{aligned}A &= R_{n-1}\cdots R_0 \\ &= -R_z(-\varepsilon)\left[R_z(-\beta_1 + 2\varepsilon)R_y(\theta)\right]^n R_z(\varepsilon).\end{aligned} \tag{9.3}$$

The precession angles s_R and s_H can be expressed in terms of physical parameters as follows

$$\begin{aligned}s_R &= \frac{2\alpha_R m^* L}{\hbar^2} \\ s_H &= \frac{\omega_L L}{v_F}\end{aligned} \tag{9.4}$$

with L the sidelength of the polygon, ω_L the Larmor frequency, and v_F the Fermi velocity[2]. The expression for s_R follows from [45]. The sidelength L can be written in terms of the circumradius R of the polygon

$$L = 2R\sin\frac{\pi}{n}. \tag{9.5}$$

[2]The spin rotates about the Rashba effective magnetic field $\vec{B}_{eff}$ as a function of distance travelled, but about the applied magnetic field as a function of time, hence the incorporation of the Fermi velocity.

Subsequently, the limit to a circle is taken by letting n go to infinity. The following result for the total rotation A of the spin travelling one complete circle counter-clockwise is obtained

$$
\begin{aligned}
A &= -R_{\hat{\boldsymbol{\xi}}}(\eta) = -\begin{pmatrix} e_0 + ie_3 & e_2 + ie_1 \\ -e_2 + ie_1 & e_0 - ie_3 \end{pmatrix} \\
e_0(A) &= \cos\frac{\eta}{2},\ \boldsymbol{e}(A) = \hat{\boldsymbol{\xi}} \sin\frac{\eta}{2} \\
\eta &= 2\pi\alpha \\
\alpha &= \sqrt{1 - 2c_H + c^2} \\
\hat{\boldsymbol{\xi}} &= \frac{1}{\alpha}\begin{pmatrix} 0 \\ c_R \\ -(1 - c_H) \end{pmatrix} \\
c_R &= \frac{2\alpha_R m^* R}{\hbar^2} \\
c_H &= \frac{\omega_L R}{v_F} \\
c &= \sqrt{c_R^2 + c_H^2}
\end{aligned}
\tag{9.6}
$$

where $R_{\hat{\boldsymbol{\xi}}}(\eta)$ is the quantum-mechanical rotation operator expressed in terms of the Euler parameters e_0 and $\boldsymbol{e}$, the rotation direction is $\hat{\boldsymbol{\xi}}$, η is the precession angle, and R is the radius of the ring. Only the result for η in the limit of zero applied magnetic field had been derived previously in Ref. [123]. Next, the various interference patterns which will play a role in ring-structures will be calculated using the total rotation A.

9.2.2 Interference intensity round-trip

The spin wave function will travel simultaneously both ccw and cw along the circle. Consequently, the initial spin wave function $|\nearrow m\rangle$ will be transformed into

$$
|\psi_{\mathrm{rt}}\rangle = e^{i\delta}\frac{1}{2}A\,|\nearrow m\rangle + \frac{1}{2}\tilde{A}\,|\nearrow m\rangle \tag{9.7}
$$

where A describes the rotation of the spin for a full ccw rotation along the circle[3], δ is an AB phase difference, and the subscript $_{\rm rt}$ stands for round-trip, i.e. $h/2e$ oscillations. $\tilde{A}$ would be the inverse of A if the spin precession about the applied magnetic field is ignored, i.e. $c_H = 0$. It is given by

$$\begin{aligned}
\tilde{A} &= -R_{\tilde{\boldsymbol{\xi}}}(\tilde{\eta}) \\
\tilde{\eta} &= 2\pi\tilde{\alpha} \\
\tilde{\alpha} &= \sqrt{1 + 2c_H + c^2} \\
\tilde{\boldsymbol{\xi}} &= \frac{1}{\tilde{\alpha}} \begin{pmatrix} 0 \\ -c_R \\ (1 + c_H) \end{pmatrix} .
\end{aligned} \tag{9.8}$$

The round-trip interference intensity for an initially polarized $\uparrow_z$ spin is then found from Eqs. (9.7, 9.6, 9.8) and is given by

$$\begin{aligned}
|\psi_{\rm rt}(\uparrow_z)|^2 = \frac{1}{2} \Bigg(&\frac{1}{\alpha} \sin\delta \cos\frac{\tilde{\eta}}{2} \sin\frac{\eta}{2}(1 - c_H) + \frac{1}{\tilde{\alpha}} \sin\delta \cos\frac{\eta}{2} \sin\frac{\tilde{\eta}}{2}(1 + c_H) \\
&+ \cos\delta \cos\frac{\eta}{2} \cos\frac{\tilde{\eta}}{2} - \frac{1}{\alpha\tilde{\alpha}} \cos\delta \sin\frac{\eta}{2} \sin\frac{\tilde{\eta}}{2}(1 + c_R^2 - c_H^2) + 1 \Bigg) .
\end{aligned} \tag{9.9}$$

The interference intensity for an unpolarized initial beam is

$$|\psi_{\rm rt}(0)|^2 = \frac{1}{2} \left(\cos\delta \cos\frac{\eta}{2} \cos\frac{\tilde{\eta}}{2} - \frac{1}{\alpha\tilde{\alpha}} \cos\delta \sin\frac{\eta}{2} \sin\frac{\tilde{\eta}}{2}(1 + c_R^2 - c_H^2) + 1 \right) \tag{9.10}$$

which reduces to the well-known equation for the conductance (see for instance Ref. [123]) for $c_H = 0$.

9.2.3 Interference intensity half-way

The interference intensity half-way corresponding to the h/e oscillations can be derived by considering the spin wave function after travelling half of the circle both ccw

[3]Notice the $\frac{1}{2}$ since if $A = I$, i.e. no rotation, the initial wave-function should result. The $\frac{1}{\sqrt{2}}$ in Ref. [123] is incorrect and all the interference intensities in that work should therefore be divided by 2.

and cw

$$\begin{aligned}|\psi_{\rm hw}\rangle &= \frac{1}{2}e^{i\delta'}A_1\,|\nearrow m\rangle + \frac{1}{2}\tilde{A}_2\,|\nearrow m\rangle \\ A &= A_2A_1 \\ \delta' &= \frac{\delta}{2}.\end{aligned} \tag{9.11}$$

The half-way rotations are readily derived to be

$$\begin{aligned}A_1 &= R_z(\pi)R_{\boldsymbol{\xi}}\left(\frac{\eta}{2}\right) \\ A_2 &= -R_{\hat{\boldsymbol{\xi}}}\left(\frac{\eta}{2}\right)R_z(-\pi) \\ \tilde{A}_2 &= R_z(-\pi)R_{\hat{\tilde{\boldsymbol{\xi}}}}\left(\frac{\tilde{\eta}}{2}\right).\end{aligned} \tag{9.12}$$

From Eqs. (9.11, 9.12), the half-way interference intensity for an initially polarized $\uparrow_z$ spin is found to be

$$\begin{aligned}|\psi_{\rm hw}(\uparrow_z)|^2 = \frac{1}{2}\Bigg(&-\frac{1}{\alpha}\sin\delta'\cos\frac{\tilde{\eta}}{4}\sin\frac{\eta}{4}(1-c_H) - \frac{1}{\tilde{\alpha}}\sin\delta'\cos\frac{\eta}{4}\sin\frac{\tilde{\eta}}{4}(1+c_H) \\ &-\cos\delta'\cos\frac{\eta}{4}\cos\frac{\tilde{\eta}}{4} + \frac{1}{\alpha\tilde{\alpha}}\cos\delta'\sin\frac{\eta}{4}\sin\frac{\tilde{\eta}}{4}(1+c_R^2-c_H^2)+1\Bigg).\end{aligned} \tag{9.13}$$

The interference intensity for an unpolarized initial beam is

$$|\psi_{\rm hw}(0)|^2 = \frac{1}{2}\left(-\cos\delta'\cos\frac{\eta}{4}\cos\frac{\tilde{\eta}}{4} + \frac{1}{\alpha\tilde{\alpha}}\cos\delta'\sin\frac{\eta}{4}\sin\frac{\tilde{\eta}}{4}(1+c_R^2-c_H^2)+1\right). \tag{9.14}$$

9.3 Aharonov-Bohm oscillation amplitude modulations

The spin interference modulates the amplitude of the AB oscillations which may therefore be used to observe the interference patterns, as done in Refs. [119, 120]. The two main oscillations correspond to the full traversal of the ring before interfering with an AB oscillation period $h/2e$ and to the interference halfway around the ring which has an AB period h/e. Both have been observed experimentally. In the following

the interference patterns for a polarized current will be compared to that for an unpolarized current for both the $h/2e$ and h/e oscillations. The zero applied magnetic field limit $c_H = 0$ (but nonzero magnetic flux) will first be discussed; in Section 9.3.3 the influence of spin-precession about the magnetic field on the spin interference patterns will be presented.

9.3.1 $\frac{h}{2e}$ oscillations

The interference intensity as a function of both the AB phase δ and SOI strength c_R has been plotted in Fig. 9-2 for an unpolarized and polarized initial current. The interference pattern for a polarized initial current is asymmetric with respect

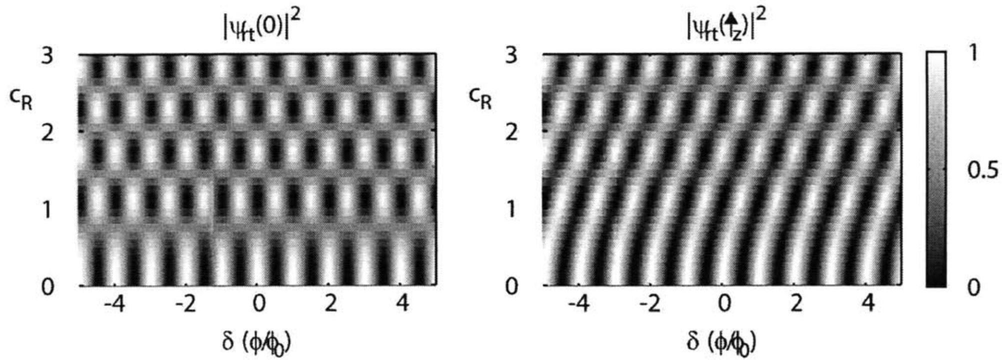

Figure 9-2: Round-trip interference intensity as a function of δ and c_R for unpolarized initial beam (left, Eq. (9.10)) and a polarized initial beam (right, Eq. (9.9)). Notice that a maximum interference intensity corresponds to a minimum in conductance. The applied magnetic field influence on the spin has been neglected, i.e. $c_H = 0$. The flux unit is $\phi_0 = h/2e$.

to magnetic flux, whereas for an unpolarized initial current it is symmetric. Any asymmetry detected would therefore be a clear demonstration of the current being spin-polarized. If the current is only partially polarized then the interference pattern will be a weighted sum of the unpolarized and 100% polarized patterns as shown for instance in Fig. 9-3 for a 25% initial polarization and $c_R = 2.0$. For a ring of

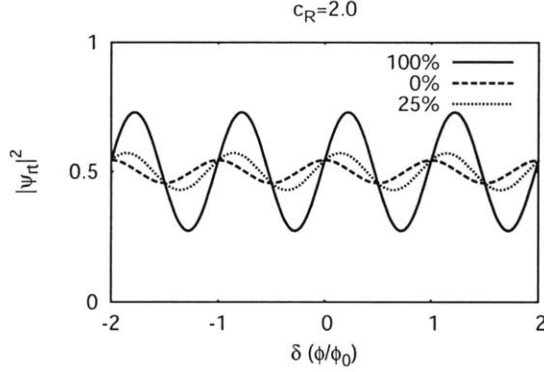

Figure 9-3: Round-trip interference intensity as a function of magnetic flux δ for Rashba field strength $c_R = 2.0$ for polarized, unpolarized and partially polarized current. This Figure corresponds to crossections of the interference patterns in Fig. 9-2 along $c_R = 2.0$ and to a weighted sum of the two (25% polarized, 75% unpolarized).

radius $R = 1\ \mu$m, $c_R = 2.0$ corresponds to a Rashba value $\alpha_R = 1.5$ peVm which is a typical value for InGaAs/InAlAs quantum wells (the effective mass used is given in Eq. (9.15) and is representative for InGaAs/InAlAs heterostructures). From Fig. 9-3 it can be observed that the influence of the partial polarization can still be discerned. The initial polarization has been assumed to be in the $\uparrow_z$ direction and for a different initial polarization direction the exact interference pattern will be different from Fig. 9-2. However, it will still be the case that for a polarized current the interference pattern is asymmetric with respect to magnetic flux. Hence the main conclusion that the asymmetry can be used to probe the spin-polarization will continue to hold.

9.3.2 $\frac{h}{e}$ oscillations

The half-way interference intensities have been plotted in Fig. 9-4 and look qualitatively similar to the round-trip interference patterns given in Fig. 9-2 with as obvious difference that the pattern in Fig. 9-2 is twice as large as the oscillation periods in Fig. 9-4. Again, for the spin-(un)polarized initial current the resulting interference pattern is (a)symmetric with respect to the magnetic flux. Hence the h/e interference pattern can also be used to probe the spin-polarization of the current.

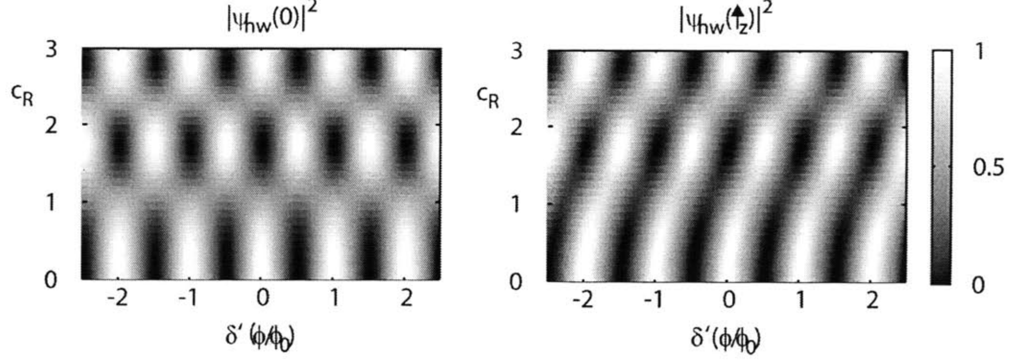

Figure 9-4: Half-way interference intensity as a function of δ and c_R for an unpolarized initial beam (left, Eq. (9.14)) and a polarized initial beam (right, Eq. (9.13)). A maximum interference intensity corresponds in this case to a maximum in conductance. Spin precession about the applied magnetic field has again been neglected, i.e. $c_H = 0$. The flux unit is $\phi_0 = h/e$.

9.3.3 Influence of Larmor precession

Different time reversal symmetric paths in ring-structures enclose different amounts of magnetic flux. As a result, the $h/2e$ oscillations will be washed out for larger applied magnetic fields. On the contrary, the h/e oscillations survive because of the many different paths contributing to those oscillations. For larger magnetic fields, it is however necessary to take into account the precession of the spin around the applied magnetic field. An estimate of the spin-magnetic field coupling strength c_H can be obtained using physical parameters relevant for InGaAs/InAlAs quantum

well-structures (effective mass from [43], g-factor and Fermi energy from [137])

$$\begin{aligned}
\omega_L &= \frac{egH}{2m^*} \\
g &= 4 \\
E_F &= 75 \text{ meV} = \frac{1}{2}\mathrm{m^* v_F^2} \\
m^* &= 0.05 m_e \\
v_F &= 7 \times 10^5 \mathrm{m/s} \\
R &= 1\ \mu\mathrm{m} \\
c_H &= \frac{\omega_L}{v_F} R = 10H \text{ rad} \\
\phi_0 &= \frac{hc}{e} = H_0 \pi R^2 = 4.2 \times 10^{-15}\ \mathrm{Tm}^2 \\
c_H &= 1.4 \times 10^{-2} \frac{\phi}{\phi_0} \text{ rad.}
\end{aligned} \tag{9.15}$$

The resulting h/e oscillations as a function of magnetic flux δ for $c_R = 1.0$ for both polarized (Eq. 9.13)) and unpolarized current (Eq. (9.14)) are given in Fig. 9-5. For $c_R = 0$ the polarized and unpolarized current give the same result and there is no modification of the interference pattern caused by spin-precession about the applied magnetic field since spins travelling in both arms of the ring undergo the same precession. For $c_R \neq 0$ the precession of the spin about the applied magnetic field modulates the interference caused by the SOI. This is clearly observed in Fig. 9-5 where the Larmor precession induces a beating pattern in the interference intensity. In [132] a similar trend was observed[4]. It is important to notice that the effect of the Larmor precession is different for the case of an unpolarized initial beam (top of Fig. 9-5) and a polarized initial beam (bottom of Fig. 9-5). For a small magnetic field the difference in the interference strength is mainly caused by the Rashba SOI but for an increasing magnetic field, the effect of the Larmor precession causes the behavior of the interference patterns for the unpolarized and polarized currents to diverge. Especially beyond the beating node its effect becomes obvious, see Fig. 9-5.

[4]Notice though that the ring-geometry in [132] has a 10× smaller radius. Hence only a few AB oscillations were observed making the beating node more difficult to discern.

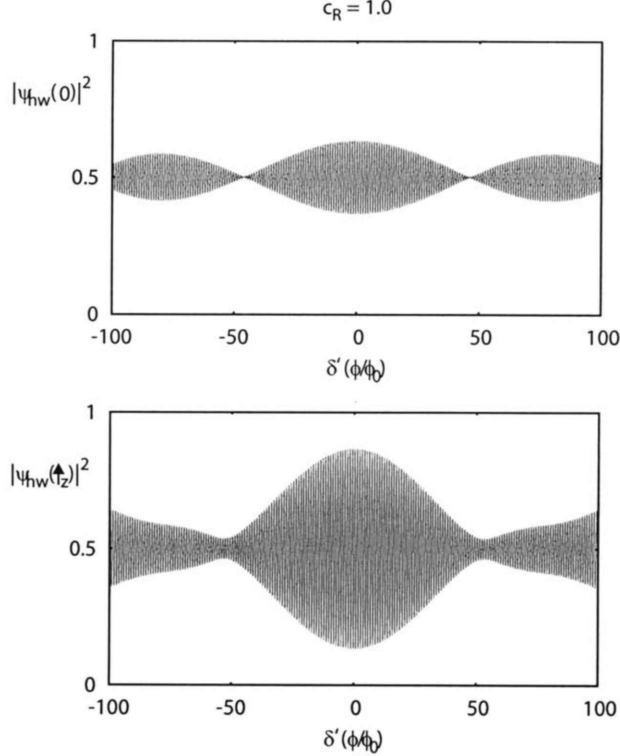

Figure 9-5: Half-way interference intensity as a function of the enclosed magnetic flux for $c_R = 1.0$. The top Figure shows the interference intensity for an initially unpolarized beam and the bottom Figure for an unpolarized initial beam. The rapid oscillations are the h/e oscillations stemming from the magnetic flux inside the ring, the modulation of these oscillations arises from the precession of the spin around the applied magnetic field. Notice that a maximum interference intensity corresponds to a maximum in the conductance. The flux unit is $\phi_0 = h/e$.

Hence the h/e spin-polarized and unpolarized interference patterns will also deviate for large magnetic field strengths.

9.3.4 Experimental observability

In this Chapter the ring-structure was assumed to be 1-dimensional. Ring-structures fabricated using lithographic tools as for instance in [119, 120] will however have a finite width and the question arises as to what the resulting influence on the conductance oscillations will be. In [123] it was shown that if both the width and Rashba

SOI are small, then the correction will only be third-order and numerically it was found that the distinctive oscillation patterns survive the finite width induced averaging over many different paths. In fact, [120] actually employs a formula for the zeros in the conductance for a 1D ring to make a quantitative comparison with experiment. Therefore, it is to be expected that the interference patterns as derived in this Chapter for 1D-rings are similar to those of experimental quasi-1D rings, and hence that rings can indeed be used to demonstrate the spin-polarization of the current. In addition, the calculated results of the conductance taking the precession around the applied magnetic field into account, derived here analytically for the first time, may be used to quantitatively analyze future experiments on rings subjected to non-vanishing magnetic fields.

In conclusion, the interference patterns of ring-shaped conductors for spin-polarized electrons have been derived for a 1D ring and it is found that the spin-polarization has a marked influence on the conductance oscillations which can therefore be employed to probe the spin-polarization of the electronic current. Furthermore, the effect of the precession of the spin around the applied magnetic field on the h/e oscillations has been discussed and found to differ as well for spin-unpolarized and polarized currents.

9.4 Multiple rings

In order to suppress the h/e oscillations, a matrix of rings is usually used, as in [120]. However, multiple rings in series will allow for many more different paths which will alter the conductance oscillations significantly, as shown for linear arrays of rings in Ref. [138] and for rectangular arrays of rings in Refs. [139, 140]. Here the spectral density of paths traversing multiple rings is analyzed. The coupling of the spin to the magnetic field will be neglected, i.e. $c_H = 0$, and only the results for an initially spin-unpolarized current will be derived.

In general, if the spin traverses the (same) ring n times before self-interfering it will give a contribution to the conductance oscillations that has an oscillation frequency

of $n \times \eta$ with η as in Eq. (9.6). However, if the path traverses multiple rings, additional oscillation frequencies result. In Fig. 9-6 are shown two different paths corresponding with a double ring traversal, and the evolution of the amplitudes of different frequency components present in their interference patterns. For a triple ring traversal, the results are shown in Figs. 9-7, 9-8, 9-9, 9-10.

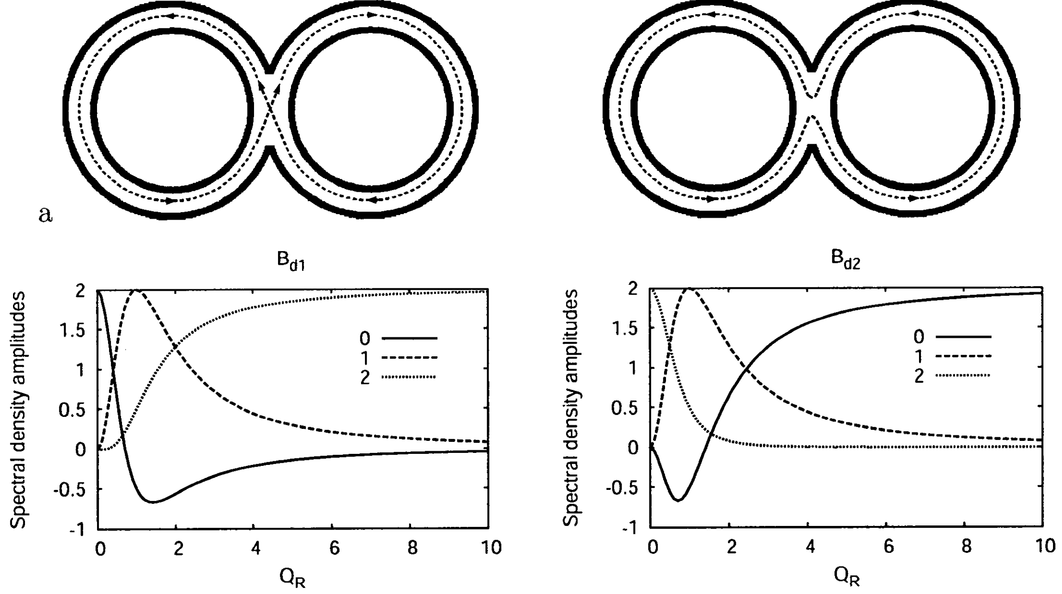

Figure 9-6: Interference path (top) and corresponding spectral density (bottom). The spectral density amplitudes are those of the oscillation frequencies $n \times \eta$ with η as in Eq. (9.6) and $n = 0, 1, 2$.

Although multiple ring traversals (before interfering) may be weaker, it is necessary to take them into account in the analysis of conductance oscillations of multi-ring structures. Individual oscillation frequencies can be discerned by taking the Fourier transform. This in combination with the observation that, for different spin-orbit strengths, different amplitudes result, may reveal which paths contribute to the conductance oscillations.

In summary, spin-interference of ring-structures subject to the Rashba spin-orbit interaction is sensitive to the spin-polarization of the electronic current. Ring-structures may therefore be used to probe whether the current is spin-polarized, i.e. they can serve as spin-detectors. One advantage of such a spin-detector would be that the spin-

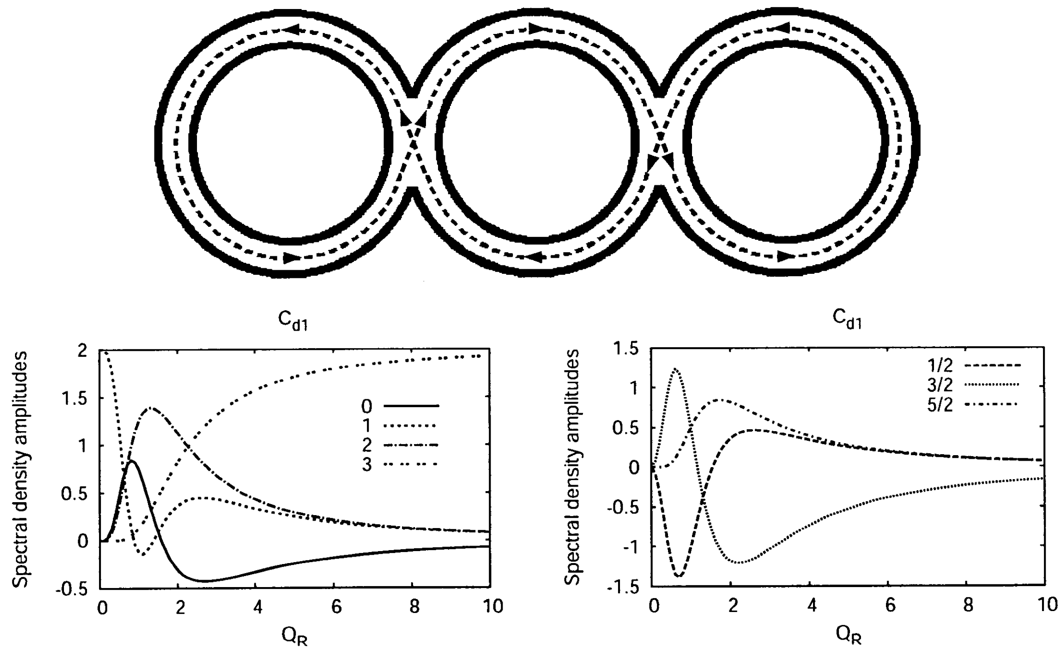

Figure 9-7: Interference path (top) and corresponding spectral density (bottom).

polarization does not have to cross any material interface in order to be detected. The spin-polarization can be discerned from both the $h/2e$ and the h/e oscillation patterns, the latter of which can be probed over a wide magnetic field range. It is also shown that the experimental suppression of the h/e oscillations by using an array of rings, will induce additional oscillation patterns due to multiple ring traversals.

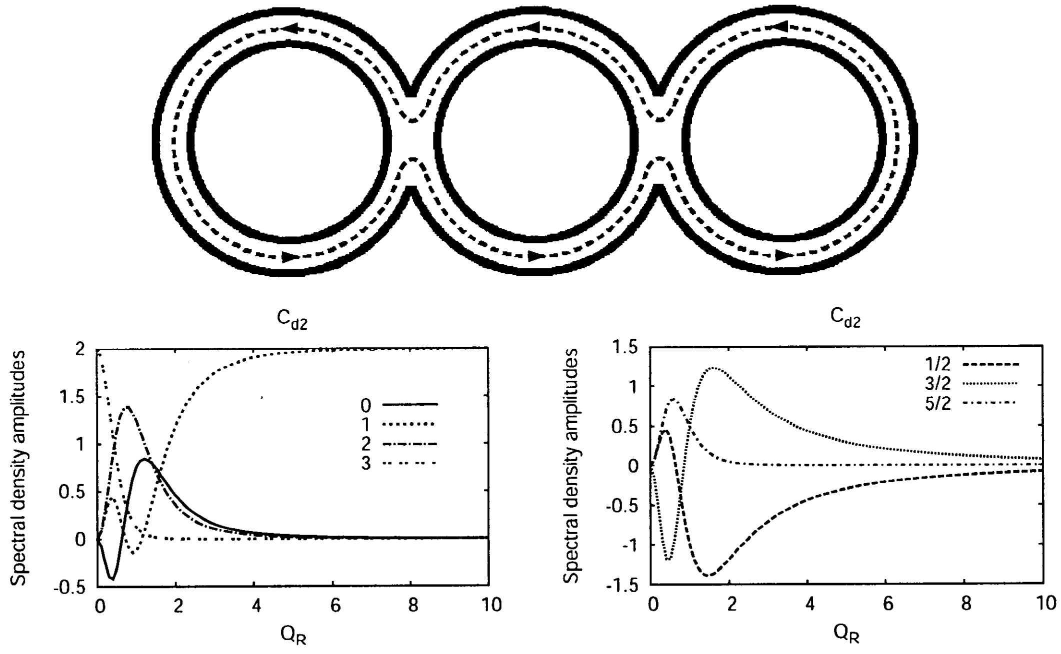

Figure 9-8: Interference path (top) and corresponding spectral density (bottom).

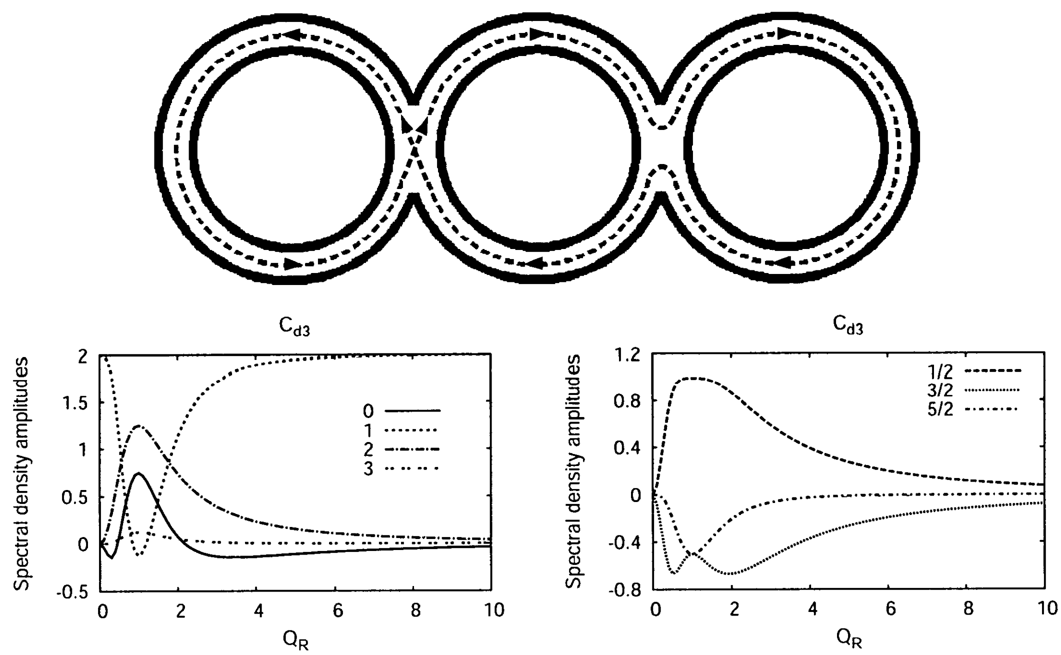

Figure 9-9: Interference path (top) and corresponding spectral density (bottom).

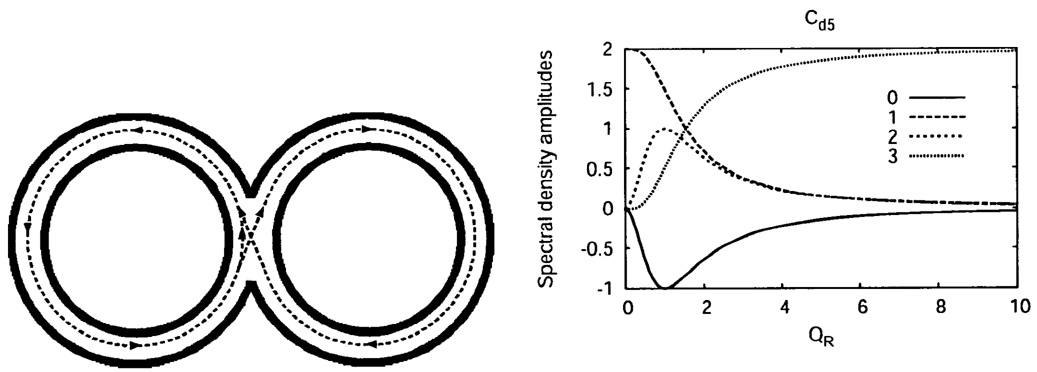

Figure 9-10: Interference path (left) and corresponding spectral density (right).

Chapter 10

Electron deflector in UHV system: scattered electrons in e-beam evaporation

The evaporating electron gun in UHV systems has as a side-effect that it gives rise to large quantities of scattered and secondary electrons. These electrons may cause damage to sensitive samples, and may yield lift-off problems of resist defined patterns. An electron deflector has been fabricated that can deflect the electrons and measure the electronic current. The result of this study appeared in [141] and is repeated below.

10.1 Introduction

A common evaporation method in ultra-high vacuum (UHV) systems uses an electron gun (egun) which generates a beam of electrons by running a current through a filament. The electrons are accelerated and directed onto a material source and heat the source up to the point where it starts to evaporate. The evaporated atoms (or molecules) subsequently land on the sample in a line of sight deposition.

A disadvantage of using electron-beam (e-beam) evaporation is that the sample will be bombarded by electrons which may cause damage to for instance pat-

terned photo- and e-beam-resist. These electrons can be divided into three categories, namely, backscattered electrons which are incident electrons reflected off the evaporation source, secondary electrons which are electrons that undergo multiple scattering events before reemerging from the evaporation surface, and thermionically emitted electrons from the source. The kinetic energies of the three categories of electrons are different; the backscattered electrons can have an energy anywhere in the range $E = 0 \ldots eV_{acc}$ (with V_{acc} the acceleration voltage of the e-gun), the energy of the secondary electrons is $E \leq 50$ eV, and the thermionic emission electrons have an energy $E \leq 1$ eV[142]. These electrons may give rise to lift-off problems of the patterned resist[1]. Therefore a deflector was machined to intercept the scattered electrons before they reach the sample, the design of which is sketched in Fig. 10-1.

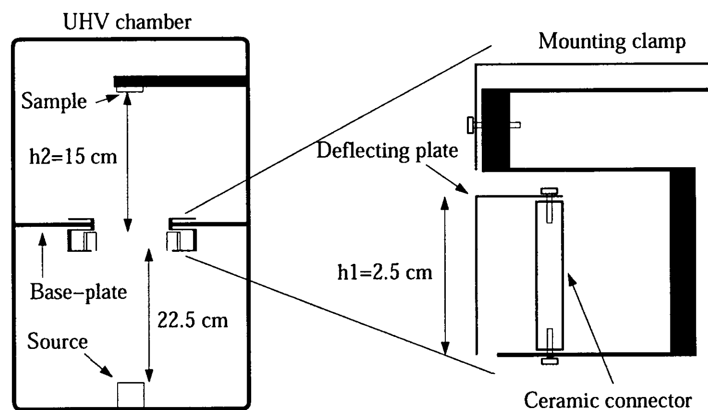

Figure 10-1: The left schematic shows the UHV chamber with the deflector position relative to the source and sample position indicated. On the right is a side-view schematic of the deflector used. The deflector consists entirely of aluminum (including the screws) except for the ceramic connector used to isolate the deflecting plate from the S-shaped hanging. The copper wires connecting the deflecting plates to the electrical vacuum feedthrough are not shown. The mounting clamp can be tightened using a screw in a tapped through-hole (through the left thick black bar, the right thick black bar serves as counterweight). The S-shape of the hanging creates an evaporation shadow on the ceramic connector such that material deposition on the connector is discontinuous and will not short the deflecting plate to the hanging.

[1]Radiative heating of the sample by X-rays in the form of bremsstrahlung of electrons incident on the material source or due to decay of excited evaporant atoms to the ground-state may also cause lift-off problems but can easily be minimized in our UHV system by cooling the substrate with liquid nitrogen.

10.2 Electron deflector

The deflector, shown in Fig. 10-1, consists of two aluminum deflecting plates, separated by 7.5 cm onto which a potential difference (between the two opposite plates) is applied. The plates hang somewhat halfway between the source and sample and are attached to a base-plate with a square hole cut in it (7.5×7.5 cm^2) which allows the evaporated material to reach the sample. The dimensions of the deflecting plates are 7.5×2.5 cm^2. A technical drawing is shown in Appendix C.4.
Electrons passing in between the deflecting plates experience the electric field and will be deflected and hence obstructed to reach the sample. Even more, the current caused by the electrons landing on the deflecting plates can be measured, examples of which are shown below. Each deflecting plate is connected to the base-plate using an S-shaped clamp connection but is isolated from it by a ceramic connector. Instead, the plates are connected by bare copper wires to an electrical vacuum feedthrough allowing for external voltage control.

10.3 Measurements: Iron

First the scattered electrons during the evaporation of iron will be analyzed. In Sec. 10.4 the results for MgO will be presented.

10.3.1 $V_{sample} = 0$ V

The electronic current as a function of applied plate voltage is measured during the evaporation of iron. The e-gun power supply is a Thermionics 150-0040 (3 kW) with a maximal acceleration voltage of 4 kV. The voltage between the deflecting plates is swept and the current between the deflecting plates (caused by charges reaching the plates) is recorded. In addition, an isolated sample plate is mounted at the sample position and is used to measure the current reaching the sample[2]. The current-voltage

[2]A decoupled substrate heater wire is used to make an electrical connection to the sample plate.

characteristics are shown in Fig. 10-2. The deflector current and sample current are

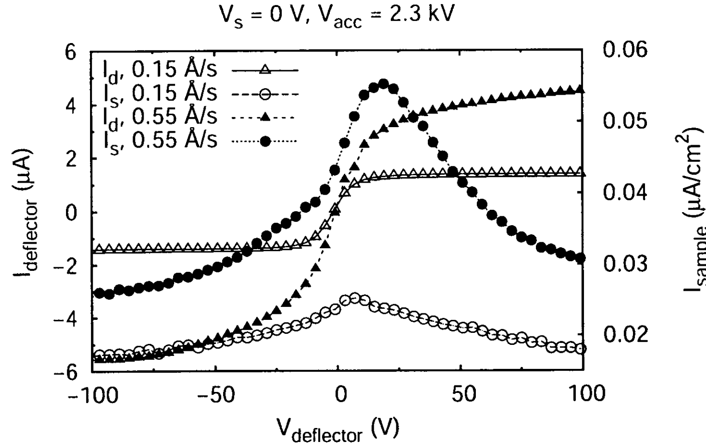

Figure 10-2: The deflector current $I_{deflector}$ (I_d, triangular symbols, left y-axis) and sample current I_{sample} (I_s, circular symbols, right y-axis) as a function of deflector voltage $V_{deflector}$ for rate of iron evaporation 0.2 Å/s and 0.6 Å/s. The sample voltage (V_{sample}) is zero. The sample current is divided by the sample plate area ($1'' \times 1''$) and therefore corresponds to dose/sec. The e-gun acceleration voltage is 2.3 kV and the pressure during evaporation is about 2×10^{-8} Torr.

plotted in Fig. 10-2 as a function of the deflector plate voltage ($V_{deflector}$) for two different rates of evaporation. The sample plate voltage is kept zero. For low rate (0.2 Å/s) the deflector current saturates at about $\pm$ 20 V which means that from that voltage on the plates hardly catch any additional electrons. The sample current reaches its maximum when the deflector current is (close to) minimal[3] which is a direct proof that the deflector intercepts electrons that would otherwise land on the sample. Although the deflector current saturates above $|V_{deflector}| = 20$ V, the sample current continues to fall off with increasing $|V_{deflector}|$ which implies that energetic electrons contribute significantly to the sample current. An estimate of the kinetic energy of the electrons can be obtained by calculating the deflection of the electrons while passing in between the deflecting plates as a function of deflector voltage for

[3]The slight difference in deflector voltage between minimum in deflector current ($V_{deflector} = 0$) and maximum in sample current ($V_{deflector} = 8$ V) can be explained by the asymmetric positioning of the sample plate with respect to the left and right deflector plate. The deflector plates are positioned symmetrically with respect to the source as can be seen from the symmetry of the $I_{deflector} - V_{deflector}$ characteristics.

different kinetic energies. The result of the calculation is shown in Fig. 10-3. The

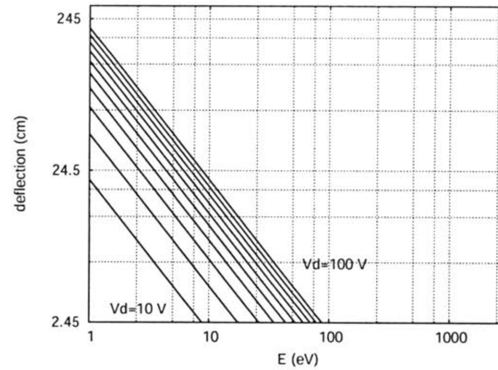

Figure 10-3: Deflection of the electrons as a function of their kinetic energy for various voltages on the deflecting plates.

sample area is 1 inch^2. Hence the minimal deflection required is at least 1 inch. As shown in Fig. 10-3, for a maximal deflecting plate voltage of 100 V only electrons with a maximal kinetic energy of approximately 100 eV are deflected enough not to reach the sample. That includes all of the thermionic emission and secondary electrons but not all of the backscattered electrons which can have an energy up to the acceleration voltage.

If the evaporation rate is increased to 0.6 Å/s then the deflector current does not saturate for $V_{\text{deflector}} = \pm$ 20 V but continues to increase with increasing deflector voltage. The sample current is much larger for high evaporation rate but otherwise shows the same features as for low rate of evaporation. Since from the above model the tail of the sample current can be identified with energetic backscattered electrons, the number of such electrons is increased significantly compared with the low evaporation rate which explains the nonsaturation of the deflector current. The peak in sample current at high rate is much larger than the peak at low rate which implies that especially the number of low-energy electrons increases with rate.

The dose delivered by the electrons to the sample can be estimated from the maximum sample current: 1/2 hour exposure at 0.2 Å/s (36 nm) gives a dose 45 μC/cm^{2}s which is significant. Typical low-energy electron-beam lithography (EBL) doses for instance are of the order of 30 μC/cm^2[143]. It should be noticed though that the energy of

the electrons is distributed below the acceleration voltage of the e-gun. The estimated dose delivered however is an average over the sample area and some areas may be much more exposed to the electrons than others yielding locally much higher doses.

10.3.2 $V_{sample} = -100$ V

Previously, the sample voltage had been kept zero. If instead a negative voltage is applied to the sample the measured current-voltage characteristics of Fig. 10-4 are obtained. The behavior of the deflector current is the same as in Fig. 10-2. However,

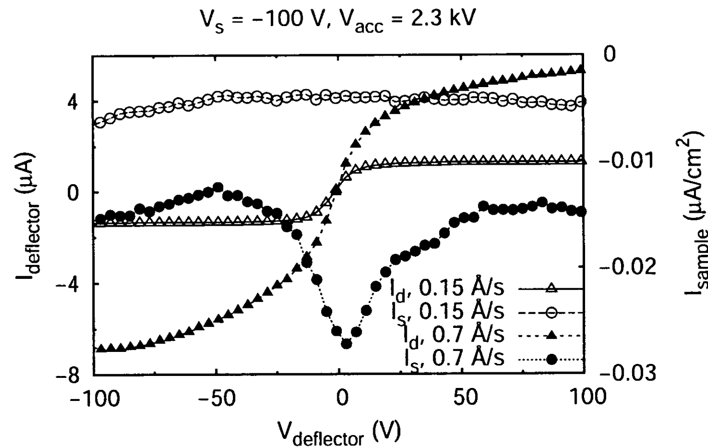

Figure 10-4: The deflector current $I_{deflector}$ (I_d, triangular symbols, left y-axis) and sample current I_{sample} (I_s, circular symbols, right y-axis) as a function of deflector voltage $V_{deflector}$ for rate of iron evaporation 0.2 Å/s and 0.7 Å/s. The sample voltage (V_{sample}) is -100 V. The sample current is divided by the sample plate area ($1'' \times 1''$) and therefore corresponds to dose/sec. The e-gun acceleration voltage is 2.3 kV and the pressure during evaporation is about 2×10^{-8} Torr.

concerning the sample current there are two things to observe from Fig. 10-4. First, the sample current is negative which in the measurement setup used corresponds to a positive charge landing on the sample. At zero deflector voltage the magnitude of the sample current is minimal which can be understood from the fact that incoming electrons give a positive contribution to the sample current (the negative sample voltage will deflect only the low-energy electrons, in a simple model electrons with

$E \leq 1/2eV_{sample}$). The second thing to notice from Fig. 10-4 is that by increasing the evaporation rate the sample current develth2.ps a dip around zero deflector current for which however the number of electrons heading toward the sample is maximal. This can be understood by arguing that the positive charge reaching the sample consists of atoms or molecules ionized by the electrons. Since the dip vanishes for higher deflector voltage it can be argued that the ionizing electrons have low kinetic energy which compares well with the maxima in ionization cross sections typically being found below 50 eV[142] (notice that the deflector voltage will not deflect significantly ionized atoms or molecules because of their much larger mass compared to electrons). A candidate for the ionized molecules is the background gas in the UHV chamber. A rough estimation of the fraction of electrons that ionizes the background gas before reaching the sample can be obtained as follows. A base-pressure of 2×10^{-8} Torr gives according to the ideal gas law (which is an excellent description of the UHV environment) a molecule number density of $\rho = 7 \times 10^{14}$ m^{-3}. The source to sample length is $z = 40$ cm. Mass spectroscopy on the UHV residue gas reveals that it mainly consists of molecular hydrogen, carbon-monoxide and molecular nitrogen. The electron-impact ionization cross section for molecular hydrogen is maximally $\sigma = 1$ Å^2[144], which is also representative for the other two gases, and the strong dependence on electron energy is neglected. Then from the Lambert-Beer law the fraction of the electrons that ionizes the background gas is $1 - 10^{-\sigma z \rho} = 6 \times 10^{-4}\%$, hence the number of ionized background gas molecules is far too small to explain the measured negative sample current.

The only other candidate for the positive sample current is ionized iron. The collision probability of electrons with iron atoms is considerable since both emerge from the evaporation source in the same stream. Furthermore, the maximum in ionization cross section for iron occurs at an electron kinetic energy $E = 25$ eV[145] which is comparable to the width of the dip in sample current. At high deflector voltage the sample current is still negative. This should be due to iron atoms that are ionized already before passing in between the deflector plates; the magnitude of the dip is comparable to the sample current at high deflector voltage which agrees with the de-

flector plates being located approximately half-way between source and sample. The absence of a dip at low evaporation rates can be explained by smaller electron-iron collision probability and, by inference from the measurement at zero sample voltage, the much smaller number of low-energy electrons at low rate. The rather broad peak in sample current for low rate is then mostly due to energetic electrons. Interestingly, at zero sample voltage both electrons and ionized iron atoms will contribute to the sample current but in opposite ways. The effective dose delivered to the sample may therefore be much larger than concluded from the measured sample current. This is further illustrated in Fig. 10-5 which gives the results for a higher acceleration voltage of the e-gun. In Fig. 10-5 the net charge reaching the sample is always negative,

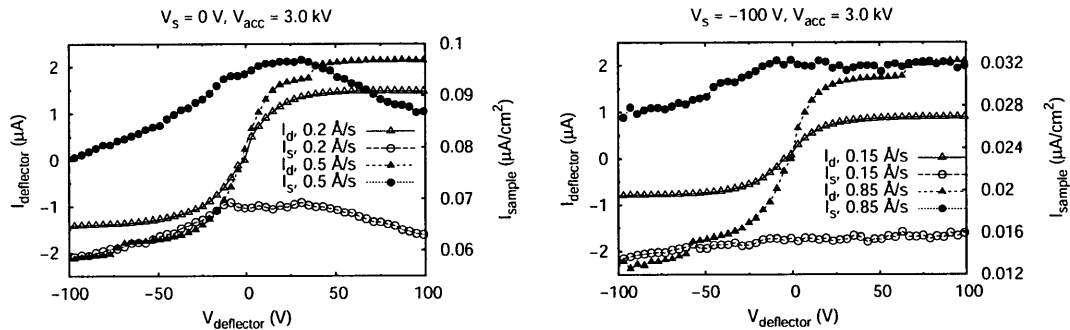

Figure 10-5: The deflector current $I_{deflector}$ (I_d, triangular symbols, left y-axis) and sample current I_{sample} (I_s, circular symbols, right y-axis) as a function of deflector voltage $V_{deflector}$ for low and high rate of iron evaporation. The sample voltage (V_{sample}) is 0 V (left) and -100 V (right). The sample current is divided by the sample plate area ($1'' \times 1''$) and therefore corresponds to dose/sec. The e-gun acceleration voltage is 3.0 kV and the pressure during evaporation is about 2×10^{-8} Torr.

despite the same negative potential on the sample plate as in Fig. 10-4. The higher e-gun acceleration voltage just produces a larger quantity of high-energy electrons that neither the electron deflector nor the negative sample voltage are able to deflect. Hence the electrons out-compete the positively charged ionized iron atoms.

In addition to ionization, the electrons may also cause excitation of the evaporated iron atoms. The subsequent decay of the iron atoms to the ground state will give rise to emitted X-rays which may inflict damage as well to the sample. The deflector can

significantly reduce the excitation of the iron atoms by intercepting the low-energy electrons which again have the highest excitation cross-section.

10.3.3 $V_{sample} = 100$ V

For completeness, also the results for a positive sample voltage are given; they are shown in Fig. 10-6. A positive voltage on the sample plate yields a large sample

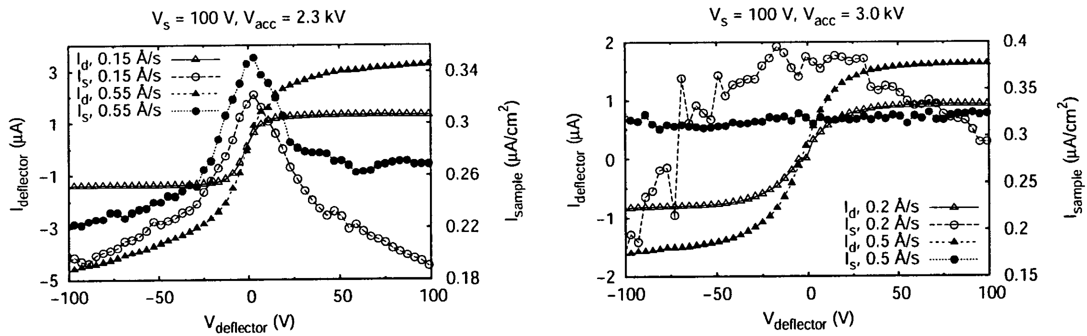

Figure 10-6: The deflector current $I_{deflector}$ (I_d, triangular symbols, left y-axis) and sample current I_{sample} (I_s, circular symbols, right y-axis) as a function of deflector voltage $V_{deflector}$ for rate of iron evaporation ≈ 0.2 Å/s and ≈ 0.5 Å/s. The sample voltage (V_{sample}) 100 V. The sample current is divided by the sample plate area ($1'' \times 1''$) and therefore corresponds to dose/sec. The e-gun acceleration voltage is 2.3 kV (left) and 3.0 kV (right) and the pressure during evaporation is about 2×10^{-8} Torr.

current. Again, for low enough acceleration voltage the electrons can be deflected; however, increasing the voltage yields higher energy electrons that are more difficult to deflect.

10.4 Measurements: MgO

During the evaporation of MgO the same measurements as during Fe evaporation have been performed. All the results are shown in Fig. 10-7. As observed in Fig. 10-7, the deflector current for $V_{acc} = 2.2$ kV is an order of magnitude larger compared to $V_{acc} = 1.5$ kV. Furthermore, since the deflector catches those electrons, they must

have low kinetic energy. Surprisingly enough though, the sample current stays flat throughout, and is negative for $V_{sample} = 0$ or -100 kV. Consequently, the MgO deposited must be charged, positively. In addition, there is no dip in the sample current for $V_{sample} = -100$ kV, contrary to what was observed in Fig. 10-4. It therefore seems that the MgO leaves the source already charged without any further ionization by the scattered electrons. Therefore, it seems that the MgO may be broken up into Mg^{2+} and O^{2-} and the resulting MgO film may be oxygen deficient. Lastly, a positive sample voltage yields a large peak of positive sample current arising from scattered electrons attracted to the sample plate.

10.5 Conclusion

During e-beam evaporation a large quantity of electrons are ejected into the deposition chamber. These electrons can have a kinetic energy anywhere between 0 and the acceleration voltage of the e-gun. The electrons may cause damage to sensitive samples in several ways. The electrons may impact on the sample and inflict physical damage or cause heating by the dissipation of kinetic energy as heat. Also, the electrons may excite the evaporated atoms with as consequence the generation of X-rays which may also cause heating of the sample. Finally, the charge itself may cause damage, for instance to tunnel barriers where a charge pile-up may cause dielectric break-down. In fact, it was found that the electrons may ionize evaporated atoms, yet another way in which charge may build up on the sample.

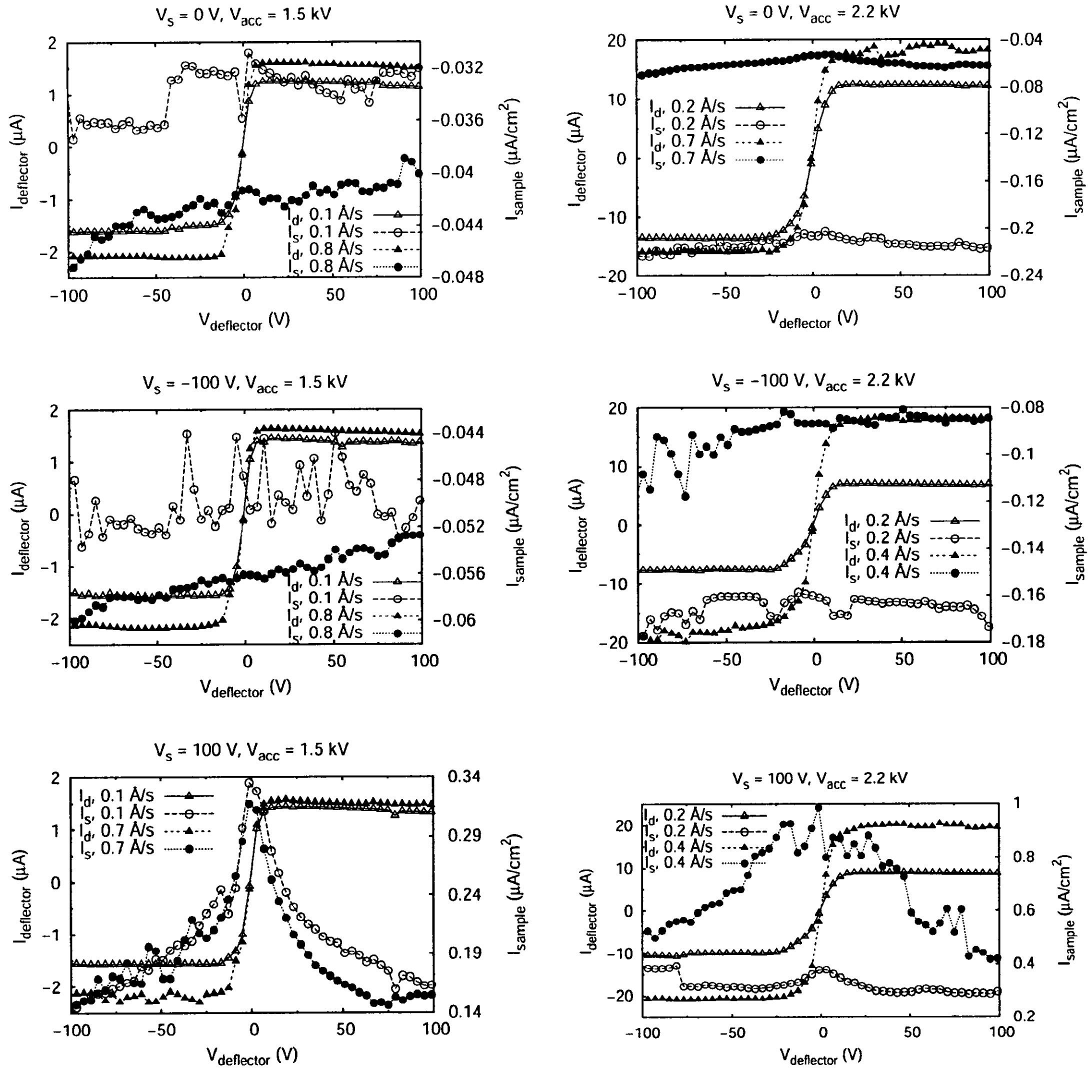

Figure 10-7: The deflector current $I_{deflector}$ (I_d, triangular symbols, left y-axis) and sample current I_{sample} (I_s, circular symbols, right y-axis) as a function of deflector voltage $V_{deflector}$ for MgO evaporation. The sample voltages are $V_{sample} = 0$ V (top), $V_{sample} = -100$ V (middle), $V_{sample} = 100$ V (bottom). The sample current is divided by the sample plate area ($1'' \times 1''$) and therefore corresponds to dose/sec. The e-gun acceleration voltage is 1.5 kV (left) and 2.2 kV (right) and the pressure during evaporation is about 2×10^{-8} Torr.

Chapter 11

Conclusion

In this work the different facets of using the tunneling emitter bipolar transistor as a spin-injector into silicon have been described. This approach to electrical spin-injection is a new technique and although not yet proven successful, it has been shown to be at least very promising. Most importantly, the working of the tunneling emitter bipolar transistor has been fully clarified using simulations and measurements, with findings for instance that ferromagnets can be used as an emitter and that the transistor works well at cryogenic temperatures. The device characteristics have been shown to be sensitively dependent on the tunnel barrier. Namely, a good tunnel barrier prefers tunneling from the emitter into the conduction band of the base above tunneling into the base valence band because of the higher barrier height for the latter. It is this property that allows the transistor to reach large values of current gain. The problem of making a good working transistor has therefore been reduced to the definition of a high-quality tunnel barrier.

Completed results have been obtained in the form of observation of negative differential transconductance, a consequence of tunneling into an inversion layer at the tunnel barrier-silicon interface. The epitaxial growth of MgO on silicon using e-beam evaporation has been realized. E-beam evaporation itself has been analyzed and the amount of scattered and secondary electrons that may damage sensitive samples has been quantified. The IV characteristics of the emitter-base junction have been fitted and it was shown that the tunnel barrier dominates the transport in the spin-injection

regime which is an important requirement to overcome the conductivity mismatch. The next step in this research can be to optimize the tunnel barrier and fabricate a high gain transistor. However, the ALD grown Al_2O_3 transistor is already good enough to be used as spin-injector in that it is stable and the current densities obtained are likely to be large enough to be probed by ESR. Therefore, a transistor based on this tunnel barrier but with a ferromagnet as an emitter may offer the ultimate proof that this new approach to electrical spin-injection is a viable one.

Appendix A

Modelling with TSUPREM4

The process simulator TSUPREM4 is employed in this Chapter to determine the oxidation and ion implantation parameters.

A.1 The growth of silicon-oxide

Silicon-oxide is grown by oxidation of the silicon, using either dry or wet oxidation. The difference between the two is that in dry oxidation the oxidizing agent is oxygen gas, whereas wet oxidation uses water vapor which is produced inside the oxidation tube by the pyrogenic reaction of hydrogen and oxygen, i.e. the water results from the combustion of hydrogen. Dry oxidation produces a denser, more perfect oxide and is therefore the method of choice for growing gate oxides or tunnel barriers. The advantage of wet oxidation is the much faster rate since the water vapor readily penetrates the already grown oxide downto the silicon. In this work wet oxidation is used to isolate individual transistors from each other.
It is straightforward to simulate with TSUPREM4 how the resulting oxide thickness depends on the temperature and annealing time of the oxidation step. Using the FOREACH statement it is possible to step through a variable temperature and save the results to a single file. The results for both dry and wet oxidation are plotted in Fig. A-1. As observable from Fig. A-1, the resulting oxide thickness differs by an order of magnitude between dry and wet oxidation. For both growth conditions,

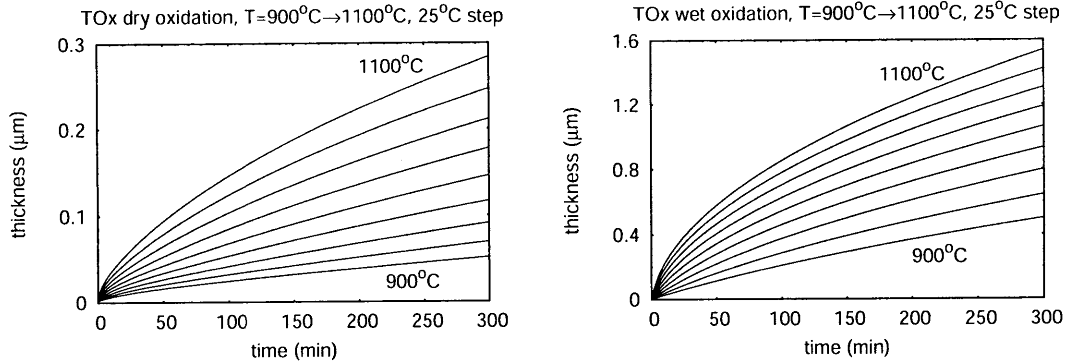

Figure A-1: Oxide thickness versus oxidation time for several different oxidation temperatures. On the left is shown the result for dry oxidation, and on the right the result for wet oxidation.

initially the oxide thickness increases linearly with time, but then the growth slows down to a square-root dependence on time. This results from the build-up of oxide through which the oxidizing agent must diffuse in order to reach the silicon surface. TSUPREM4 uses the Deal-Grove algorithm to simulate the oxidation process. By comparison with experimental results it was found that TSUPREM4 significantly underestimates the resulting oxide. The results shown in Fig. A-1 are therefore only approximately correct and merely serve as an illustration of the oxidation conditions. For the real devices, simulations were performed using the simulator [146] which uses the Massoud model and was found to yield accurate oxide thicknesses.

Two more observations concerning thermal oxide need to be made, namely, the amount of silicon consumed in the process is 46% and the resulting oxide is amorphous.

A.2 Ion implantation

One of the attractive features of semiconductors is that their properties can be changed over a wide range of scale by the introduction of donor or acceptor atoms. There are several ways to introduce doping atoms into a semiconductor. For instance, during the growth of the semiconductor, impurity atoms can be added. Another tech-

nique is the diffusion of impurity atoms into the semiconductor resulting from exposing the semiconductor surface, heated to elevated temperatures, to a gas of impurity atoms which will then diffuse into the semiconductor driven by the concentration gradient. The technique used in this work to define the base for the 2nd generation transistors is ion implantation. In ion implantation, the dopant atoms are accelerated and subsequently impinge on the semiconductor at high velocities and penetrate the semiconductor a certain distance before running out of kinetic energy. By varying the implant dose and the implant kinetic energy, a precise doping profile can be obtained. In practise the ion beam is directed on to the wafer under a slight angle, typically 7°, to minimize ion channelling, that is, deep penetration of the dopant atoms along preferred crystallographic directions[147]. In addition, the wafer is rotated at high velocity.

For the transistors in this work, the base was implanted through a thermal oxide as grown by dry oxidation. Since the ion implantation company charged the same price upto 13 wafers, that quantity of wafers was used. Variation was achieved by varying the implant oxide thickness. Boron was implanted from the top at an energy of 26 keV and concentration 2×10^{14} cm^{-2} (under an angle of 7°). The results of the obtained doping profile as simulated with TSUPREM4 are shown in Fig. A-2. Hence by using 3 different implant oxide thicknesses, transistors with different base widths are obtained without having to resort to multiple implant runs. The backside of the wafer is also implanted, with phosphorus with a concentration 5×10^{15} cm^{-2} and an energy of 180 keV. This creates an ohmic contact to the collector region.

Since ion implantation is a high energy process, it inflicts a lot of damage to the semiconductor, knocking silicon atoms out of place and disrupting the crystallinity. In order to restore crystallinity, the wafers are annealed after ion implantation. For the devices in this work the annealing temperature and time were 950°C and 10 min, respectively. This short anneal at moderate temperature has modest influence on the doping profile. Nevertheless, it has been included in the TSUPREM4 model used to generate the doping profiles as imported in the MEDICI simulations.

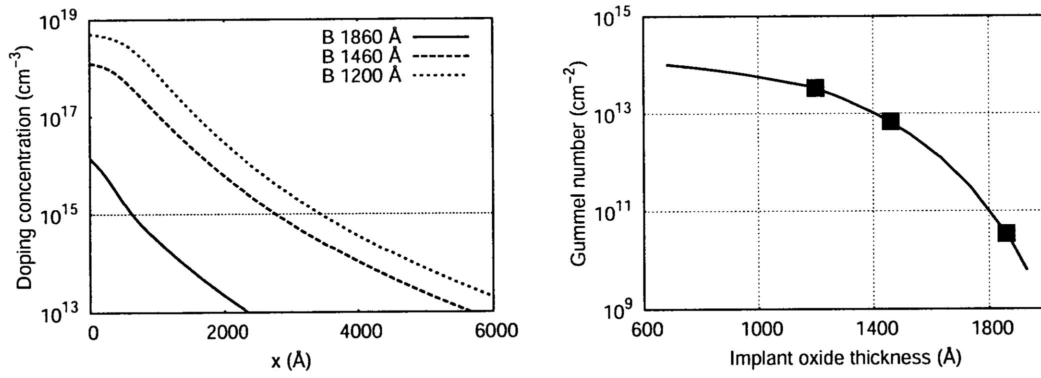

Figure A-2: Resulting doping profile after ion implantation of boron with concentration 2×10^{14} cm^{-2} and energy 26 keV under and angle of 7° into a $< 100 >$ silicon wafer with phosphorus concentration of 1×10^{15} cm^{-3}, as simulated with TSUPREM4 using the analytic model. On the right is shown the resulting Gummel numbers as found by integrating the boron concentration inside the base region (using the trapezoidal approximation and EXCEL).

Appendix B

MEDICI simulation model and additional results

B.1 Import from TSUPREM4

The doping profile of the transistor is simulated with TSUPREM4, as described in Ch. A, and imported into MEDICI using the PROFILE statement. The reason to only import the doping profile and not the whole device structure is because the mesh has to be chosen fine enough to cover the tunnel barrier. Since in the TSUPREM4 simulation the oxidation steps will transform part of the silicon into oxide, the fine mesh would have needed to extend over a large region to make sure that the ultimate thin tunnel barrier is covered by it, which would produce too many node points.

B.2 Setting up the grid

Since the tunnel barrier is chosen very thin, in order to allow for direct tunneling, the grid has to be chosen very carefully. Namely, grid points should clearly be fine enough to cover the tunnel barrier. However, this fine grid cannot be maintained across the whole device since there is an upper limit on the number of nodes. The strategy is then adopted to start with a very fine mesh and to let the spacing increase after the definition of the tunnel barrier. The maximum in number of nodes also

places a restriction on the lateral dimensions of the device which have accordingly been chosen roughly to be a factor 10 smaller than the real transistor. After the mesh specification, the various regions of the transistor are defined, followed by an import of the doping profile. Then the mesh is further refined by several REGRID statements based on the doping profile. The ultimate grid is shown in Fig. B-1. From Fig. B-1

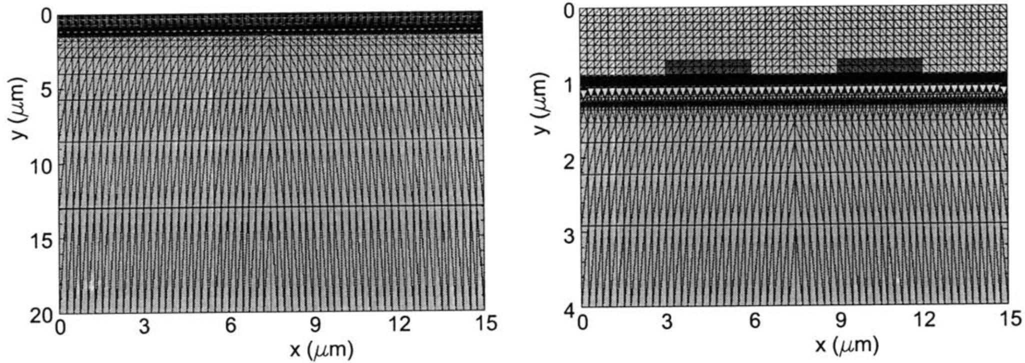

Figure B-1: Shown is the device structure together with refined, overlayed grid as used in the simulations. The left shows the total device, and the right only the top part. The light-blue material is silicon-oxide, the dark-blue blocks are the base (left) and emitter (right) contacts, the base region is yellow and the collector green.

it is observed that the refinement both removes some nodepoints between the tunnel barrier and PN-junction and introduces additional nodes at the PN-junction. Notice that the width of the collector has been chosen quite large in the simulation, first of all to be in approximate scale with the other device dimensions, but also to nullify the influence of the collector contact on the transistor simulations. Also, all over the device a silicon-oxide layer has been defined, the reason being that in MEDICI the surface has to start everywhere with the same height.

After the device geometry has been set up, it is a matter of simply applying biases to the different contacts and saving the output. The connections are made in the common-emitter geometry with the emitter contact grounded. Both Gummel plots and collector-emitter sweeps are simulated, the results of which will be presented below. All the 1-dimensional plots are along the crossection $x = 10.5$ μm of Fig. B-1 which intersects the emitter contact midway.

B.3 Tunneling model

There are several tunneling models available in MEDICI. All the simulations of Chapter 2 were performed with the Gundlach method. In addition, only direct tunneling from the *conduction band* was considered. Here it is shown that this is a valid assumption.

In general valence band electrons and holes can tunnel through the barrier as well. It is therefore imperative to consider the effect of each of these tunneling modes on the transistor performance. This has been simulated in Fig. B-2 for the modes and their combinations. Clearly observable in Fig. B-2 is that both valence band electron and valence band hole tunneling are negligible compared to conduction band tunneling. Even in the absence of conduction band tunneling they hardly play a role; the increase in base current in Fig. B-2 comes from forward biasing of the base-collector junction. The little influence of valence band tunneling stems from the much higher tunnel barrier for valence band electrons and holes. This is the fundamental reason why the tunneling emitter bipolar transistor can have a very large gain; the suppression of valence band tunneling by the tunnel barrier enhances the emitter injection efficiency. Consequently, for the simulations the base current in the active region results from carrier recombination inside the base.

B.4 Transistor action plots for varying base currents

In Fig. B-3 are shown the transistor action plots over 9 decades of base currents. These plots are obtained by choosing the CURRENT boundary condition in MEDICI.

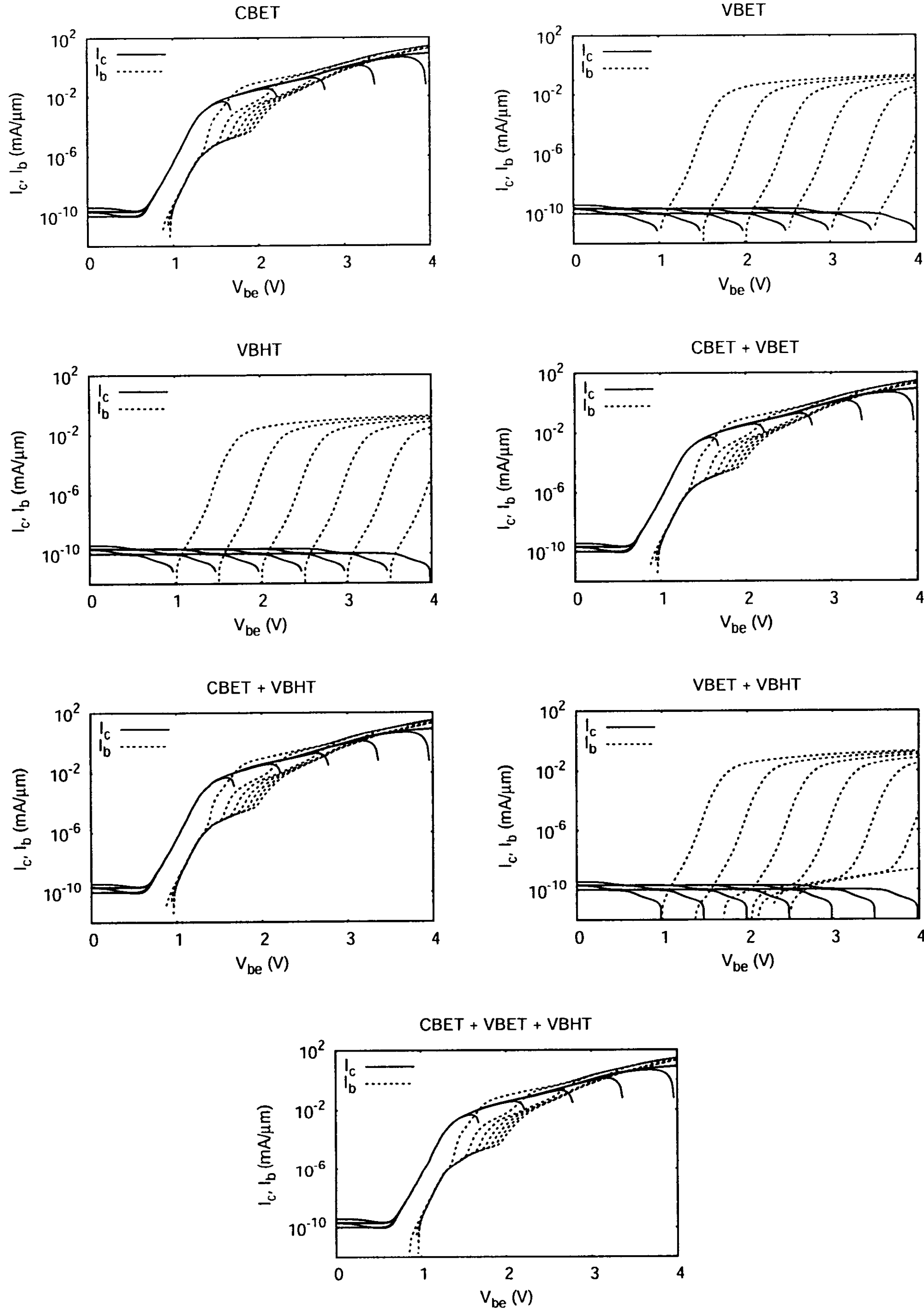

Figure B-2: Gummel plots for different modes of tunneling; conduction band (CBET), valence band electron (VBET), and valence band hole (VBHT). The tunneling model is the WKB method; the Gundlach method did not work well with valence band tunneling. The transistor corresponds to the implant oxide thickness 120 nm. The work function is 4.5 eV, the tunnel barrier affinity is 3.0 V and the tunnel barrier width is 20 Å.

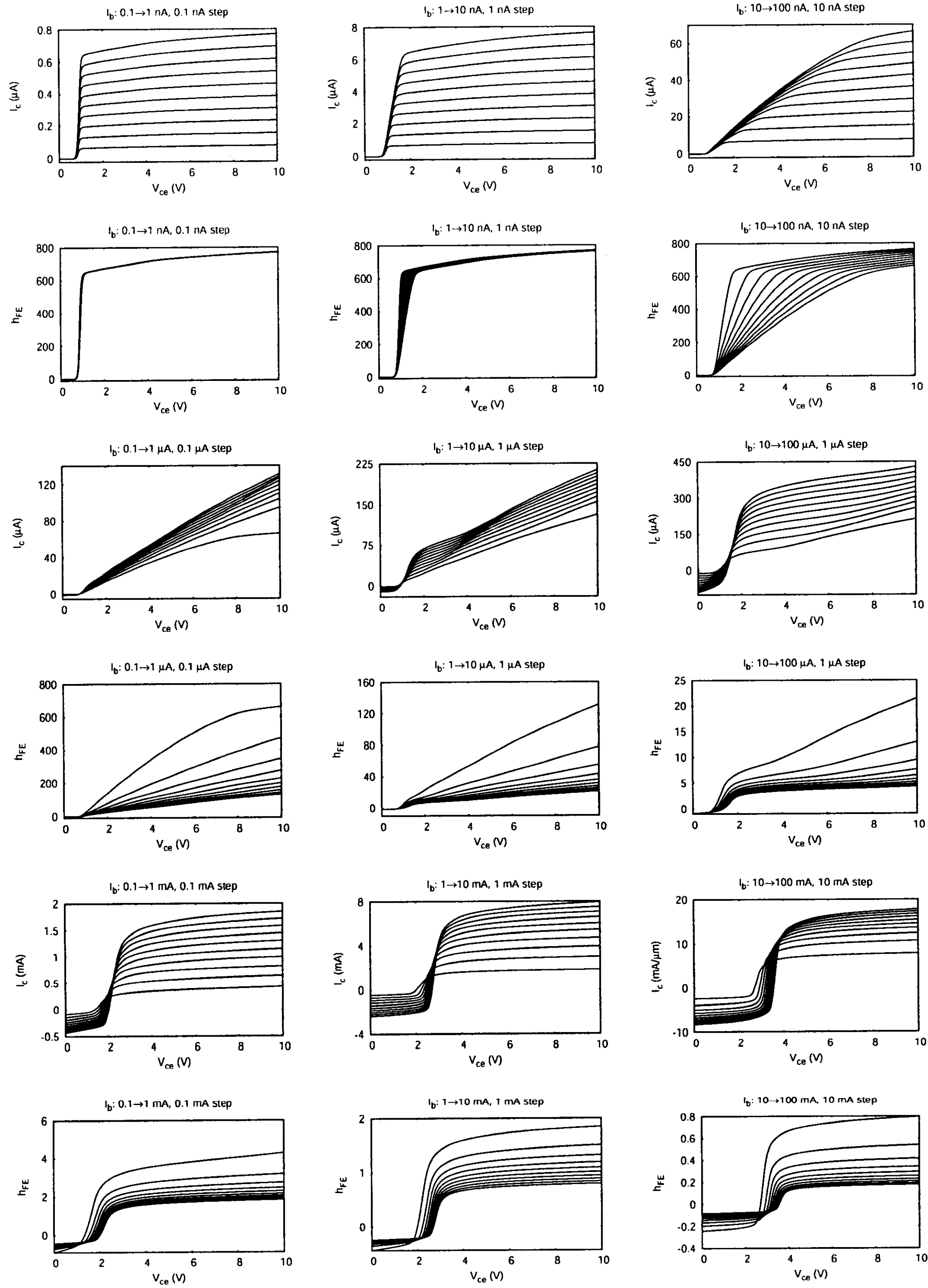

Figure B-3: Transistor action plots for implant oxide thickness 120 nm over a wide range of base currents I_b. The odd rows depict the collector current I_c and the even rows the corresponding current gain h_{FE}. The work function is 4.5 eV, the tunnel barrier affinity is 3.0 V and the tunnel barrier width is 20 Å.

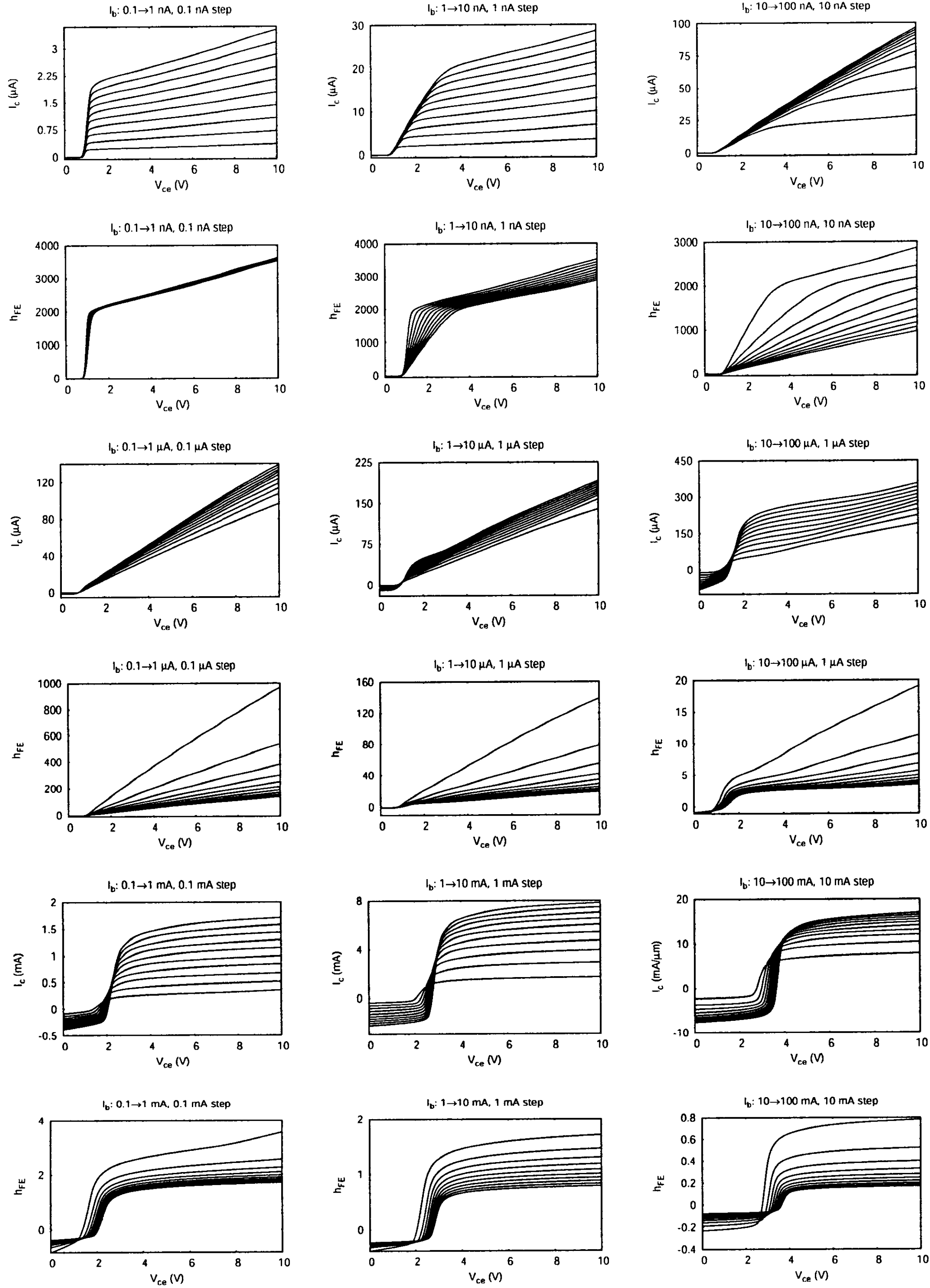

Figure B-4: Transistor action plots for implant oxide thickness 146 nm over a wide range of base currents I_b. The odd rows depict the collector current I_c and the even rows the corresponding current gain h_{FE}. The work function is 4.5 eV, the tunnel barrier affinity is 3.0 V and the tunnel barrier width is 20 Å.

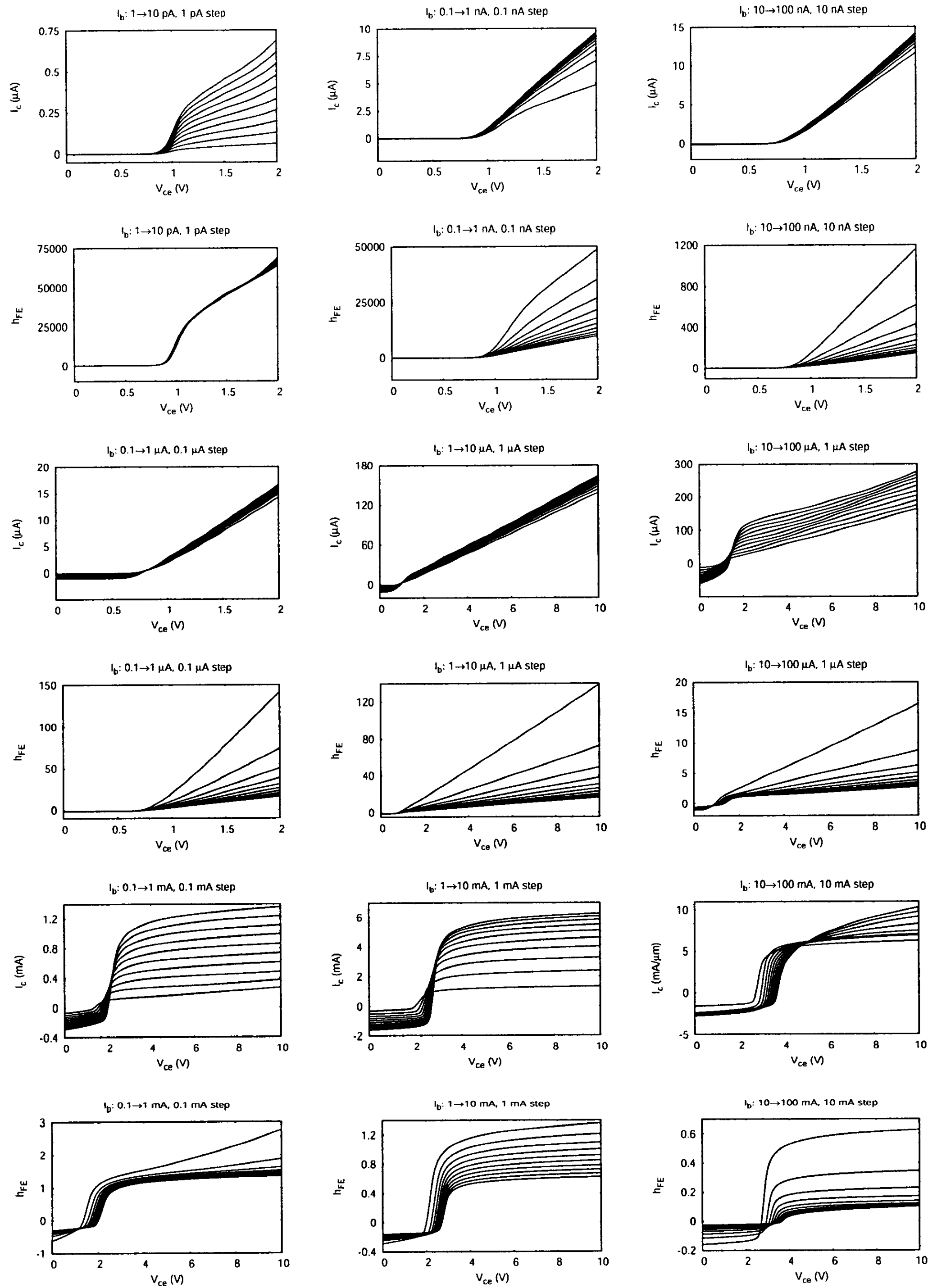

Figure B-5: Transistor action plots for implant oxide thickness 180 nm over a wide range of base currents I_b. The odd rows depict the collector current I_c and the even rows the corresponding current gain h_{FE}. The work function is 4.5 eV, the tunnel barrier affinity is 3.0 V and the tunnel barrier width is 20 Å.

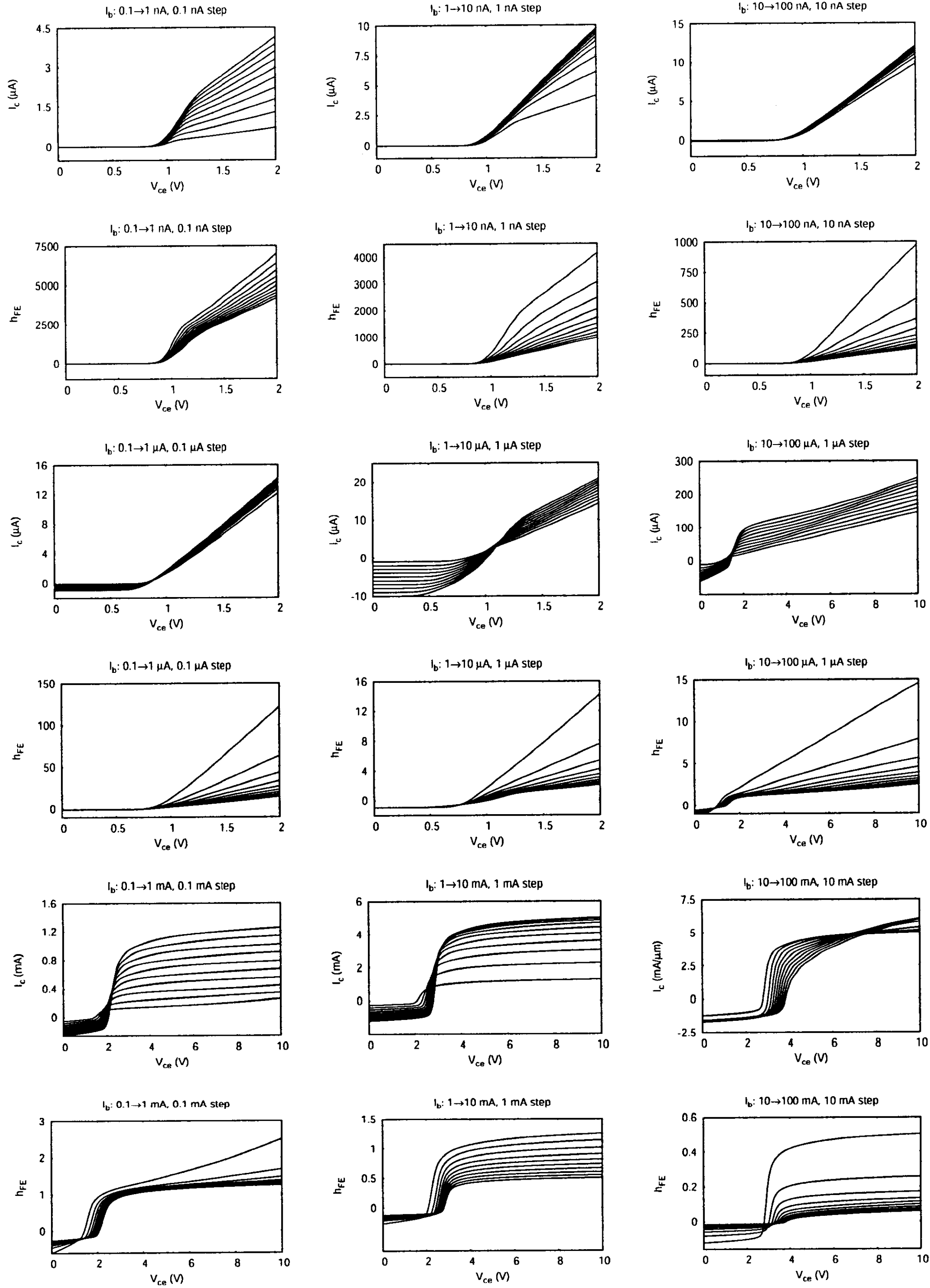

Figure B-6: Transistor action plots for PN-epiwafer with base thickness of 1 μm over a wide range of base currents I_b. The odd rows depict the collector current I_c and the even rows the corresponding current gain h_{FE}. The work function is 4.5 eV, the tunnel barrier affinity is 3.0 V and the tunnel barrier width is 20 Å.

Appendix C

Machining and electronics

Several tools have been developed to aid in device fabrication and measurements. This Appendix presents the most interesting of them.

C.1 Measurement probes

Several measurement probes have been made, each with a different socket to hold the sample. An image of one such probe is shown in Fig. C-1. The top part of the

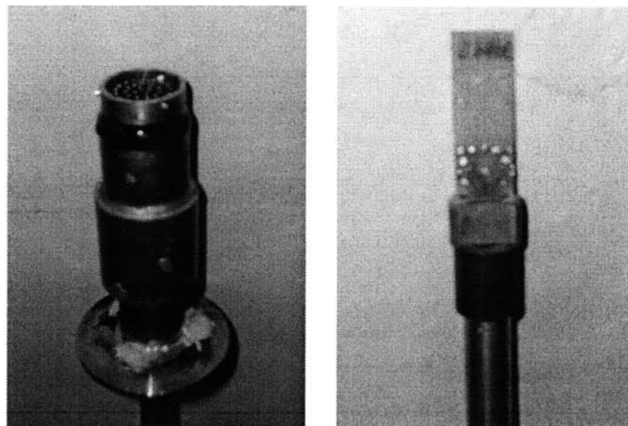

Figure C-1: Top (left) and bottom (right) of measurement probe. This probe was used to measure the PN-epiwafer samples as well as the DMR samples.

probe, shown in Fig. C-1 on the left, consists of an aluminum tube to which are soldered a sealing flange that connects to the cryostat with an o-ring, and a couple of

pipe fittings which are used to bring the diameter to that of the hermetically sealed 32-pin connector (from the company Deteronics) on top. The connector is epoxied to a pipe fitting (using stycast, black in image); standard soldering would damage the coax cables inside the tube whereas low-temperature soldering with indium does not provide enough mechanical strength. The bottom part shown on the right consists of a socket made of isolating phenolic which holds a standard card socket for the probe in Fig. C-1. The wires inside the measurement probes are coaxial cables (Harbour RG178); the same wire is used in the probestation described below in Section C.5. The shielding of the wires is connected together at one end and fed through to a pin of the connector.

C.2 Spin-coater head

For small sample processing, such as the silicon-germanium devices, a small-style sample holder head for the spin-coater needed to be developed. The technical drawing is shown in Fig. C-2. As the material stainless steel is chosen; stainless does not wear

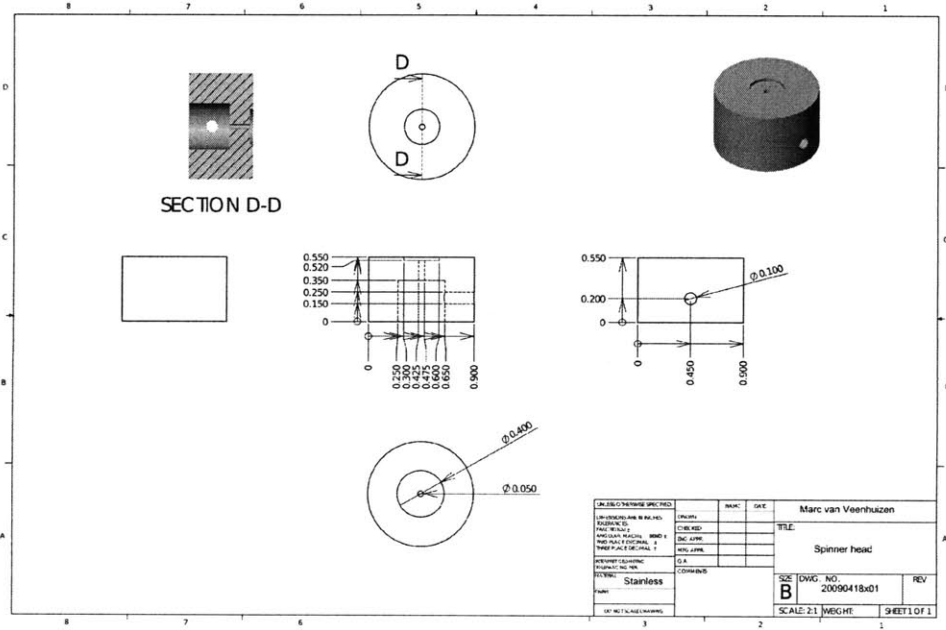

Figure C-2: Sample holder for spin-coater

out easily which is especially relevant for the set-screw (hole in the side, see Fig. C-2) with which to mount the spinner head onto the spin-coater. On top of the spinner head is placed a rubber O-ring on top of which is placed the sample. This simple construction works well, and the sample is held in place up to very high speeds.

C.3 Annealing boat

For in-house ohmic contact fabrication, an annealing station had been developed. It basically consists of a quartz tube with inner diameter 28 mm, embedded in a thermally isolated cylinder that contains a heater wire. Heater currents are controlled with a variac. Samples are mounted on a boat whose technical drawing is given in Fig. C-3. The boat is made of aluminum which is easy to machine. The nose-like

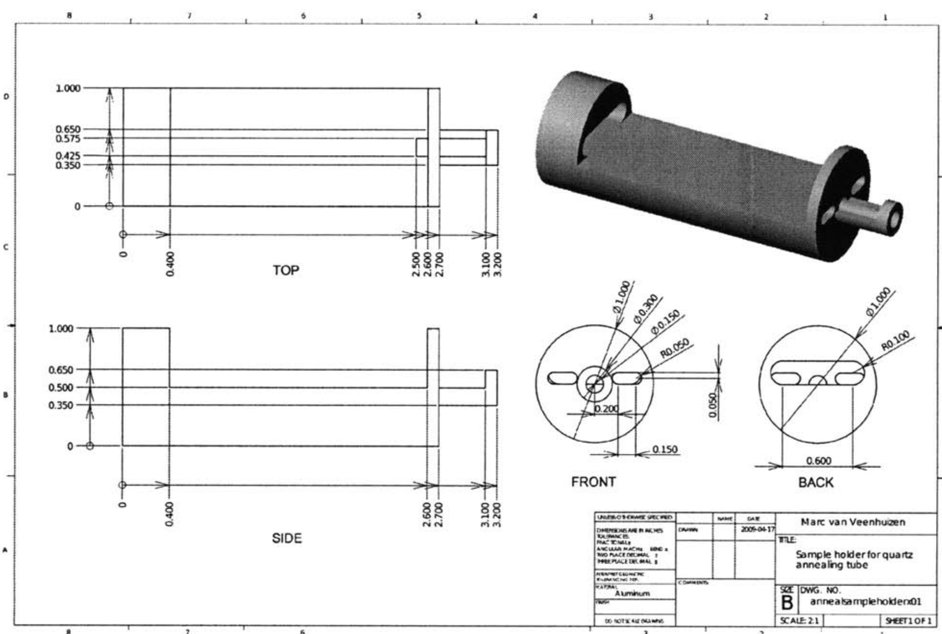

Figure C-3: Annealing boat that fits into a quartz tube.

feature on the boat is designed to hook a mounting rod (metal with isolated handle) to with which the boat is pushed or pulled into or out of the quartz tube. The thick part on the opposite end serves as a counterweight when the boat is pulled half-way out of the tube to retrieve the samples. Without it, the boat would tumble out of the

tube while doing so. The holes at the front, and the sleeve at the back serve as air channels; annealing is commonly done in a forming gas atmosphere (5%H_2, 95%N_2) and these passways make sure that there is no vent shadow over the samples.

C.4 Electron deflector

The electron deflector has been described in Chapter 10. The technical drawing is given in Fig. C-4.

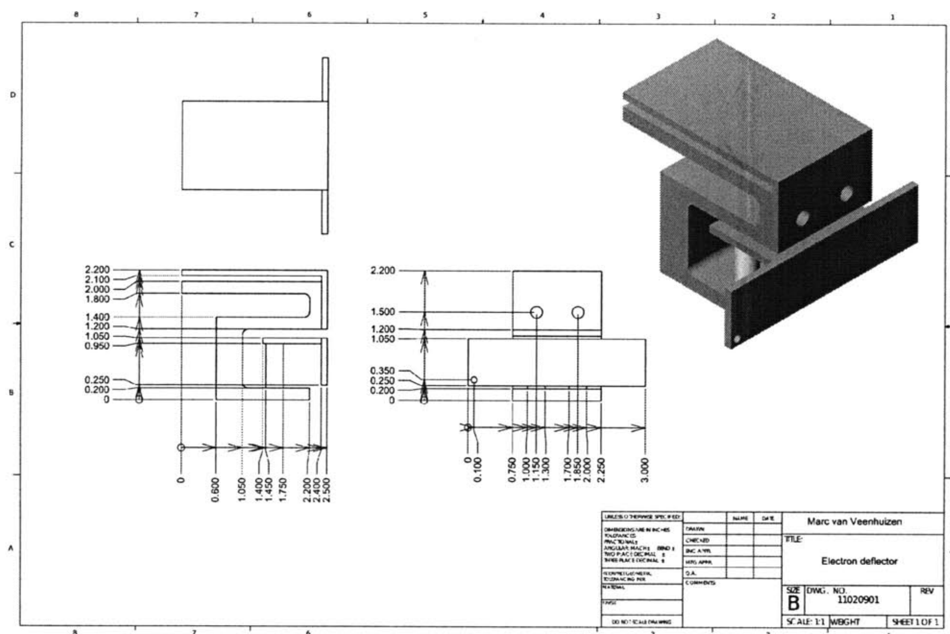

Figure C-4: Electron deflector used to deflect scattered electrons from electron beam evaporation. Here is shown only the left deflector; the right deflector is a mirror image.

C.5 Probe station

In order to contact the small transistor contacts as well as to speed up device characterization, a room-temperature probe station has been developed. It consists of 4 XYZ micropositioners on which the probes are mounted plus an XY positioner

that holds the sample stage. The micropositioners are bought from the company Optosigma. The other parts are hand-made.

C.5.1 Base plate

As base plate is chosen a $24 \times 24 \times 0.25$ inch^3 aluminum plate into which holes are drilled and tapped. It is shown in Fig. C-5.

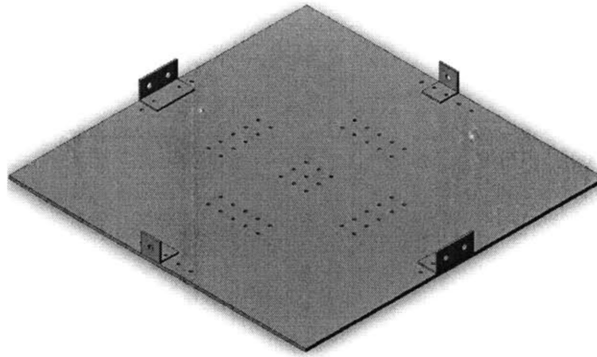

Figure C-5: Base plate of probe station made of aluminum. The angles are made of plastic and serve as mounts for the bnc connectors.

C.5.2 Sample stage

The sample stage also serves as a back contact to the collector of the transistor. Therefore it needs to be isolated from the rest of the world. This is done by the construction shown in the technical drawing Fig. C-6. The sample plate is separated from the footing (and the rest of the probe station) by an isolating piece of plastic. The 4 holes in the center of the footing are then used to attach to the sample plate, with plastic screws, and the 4 outer holes are for mounting on top of the XY manipulator. The additional hole in the sample plate in the corner is used to attach a coax cable to, i.e. to make an electrical connection to the sample plate.

Figure C-6: Sample stage of probe station consisting of three parts: the sample plate (top left), the plate footing (right), both of aluminum, and a plastic isolator that goes between the footing and plate (bottom left).

C.5.3 Probe holder

The probe holder connects the probe needles to the XYZ micropositioners. It consists of 4 parts which are shown in Fig. C-7. The assembly is shown in Fig. C-8. The connector to the micropositioner is formed by the angle shown in the lower left of Fig. C-7. On top of the angle is screwed an aluminum block (top left same Fig.). A 30° hole is drilled through the block through which a hollow plastic rod slides. The rod contains the coax cable that connects to the probe needle. It is held in place inside the block by 2 set-screws in the block that are under an angle of 90° with respect to each other. The fourth part of the probe holder is a teflon piece that holds the needle, shown in bottom right of Fig. C-7. Teflon is an excellent electrical insulator hence this connector isolates the needle from the rest. With everything put together, the probe holder looks like Fig. C-8.

Figure C-7: Individual parts of the probe holder of the probe station.

C.6 Curve tracer

Measurements on the 2nd generation transistors were performed with a home-built curve tracer, designed by David Bono. The analog part of the curve tracer consists of a 50 Hz triangle wave voltage source that ramps up and down the collector-emitter voltage and a base current step generator that outputs 10 steps in base current, as illustrated in the schematics Fig. C-9. The curve tracer also monitors the collector current (I_c), collector-emitter voltage (V_{ve}), base current (I_b) and base-emitter voltage (V_{be}) which allows for extraction of the transistor parameters, as demonstrated in Sec. 8.4. The analog signals are digitized and controlled using a 16 bit general purpose data-acquisition system (NI PCI-6052E) turning the curve tracer effectively into a digital curve tracer. An image of the curve tracer and probe station is shown in Fig. C-10.

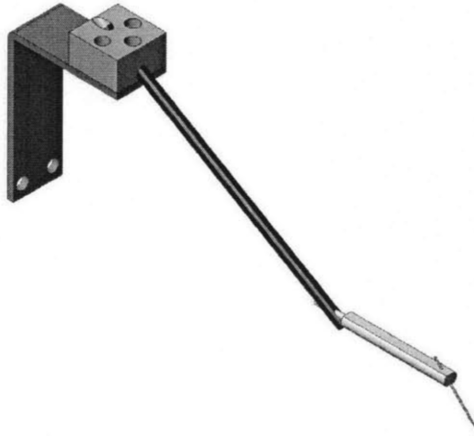

Figure C-8: The assembled probe holder of the probe station.

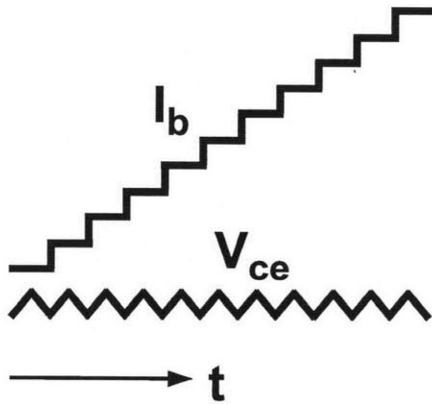

Figure C-9: Base current (I_b) steps and collector-emitter voltage (V_{ce}) triangular wave output of the curve tracer. The shown output is repeated 50× a sec.

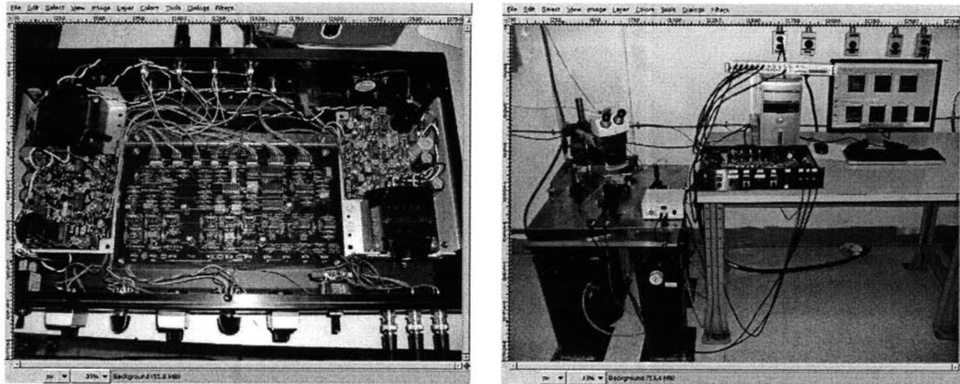

Figure C-10: On the left a close-up image of the analog part of the curve tracer, on the right an image of the complete transistor measurement setup.

Appendix D

Current-voltage characteristics and curve fitting

The emitter-silicon contact forms a metal-insulator-semiconductor (MIS) tunnel diode[87]. The diode consists of a series combination of a tunnel barrier and a Schottky barrier. In order to solve the conductivity mismatch, it is desired that the tunnel barrier dominates the transport, as described in Chapter 1. It is therefore interesting to consider the relative values of resistances of the two barriers. The applied voltage across the diode will appear partly across the tunnel barrier and partly across the Schottky barrier. Both barriers are bias-dependent, that is, their resistances change as a function of voltage. In order to extract from the current-voltage (IV) characteristics of the diode which barrier dominates, it is necessary to solve for the barrier resistances self-consistently. An IV fitting program has been written using the GNU scientific library that can do just that.

D.1 Modelling the MIS tunnel diode

In general both the tunnel barrier and Schottky barrier can be represented by a parallel combination of a resistor and a capacitor. Since here only dc currents will be considered, the barrier capacitance is ignored. The tunnel diode is then schematically given by Fig. D-1.

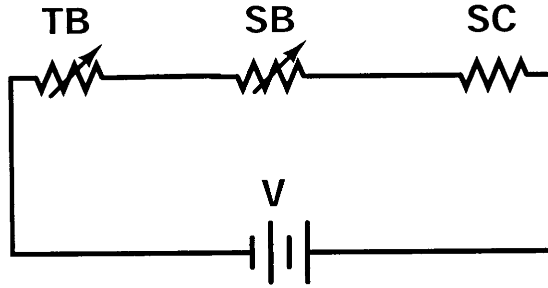

Figure D-1: Schematic of series combination of tunnel barrier (TB), Schottky barrier (SB), both bias dependent, and a series resistance modelling the bulk and contact resistance of the semiconductor (SC).

D.1.1 Tunnel barrier

Tunneling through a tunnel barrier is well described by the Simmons model [148, 149] and this model is used for the IV fitting. The input parameters are the tunnel barrier height, width, and asymmetry. The tunnel barrier asymmetry accounts for the dissimilarity of the electrodes, yielding different tunnel barrier heights on opposite ends of the barrier [149]. The resistance of the tunnel barrier is a strong function of the thickness, as illustrated in the simulation Fig. D-2.

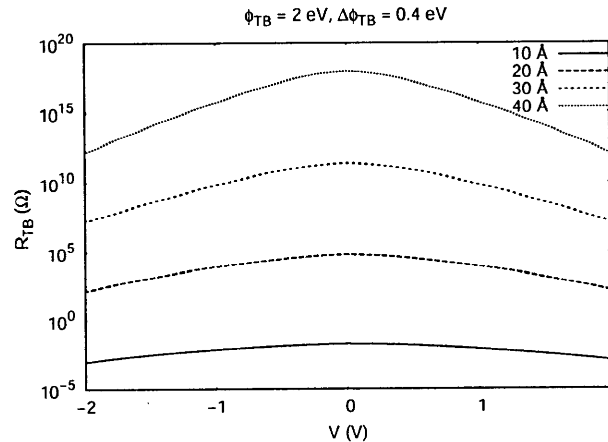

Figure D-2: Simulated tunnel barrier resistance for 4 different tunnel barrier thicknesses $10-40$ $\AA$. The barrier height $\phi_{TB} = 2$ eV and the asymmetry $\Delta\phi_{TB} = 0.4$ eV. The junction area is 120×240 μm^2.

D.1.2 Schottky barrier

Transport through the Schottky barrier is given by a combination of thermionic emission, diffusion, and tunneling. The resulting equations for all three have a similar form, however, and the total current can effectively be modeled as[150]

$$J = A^{**}T^2 \exp\left(-\frac{\phi_{SB}}{kT}\right) \exp\left(\frac{V}{\eta kT}\right) \left(1 - \exp\left(-\frac{V}{kT}\right)\right), \tag{D.1}$$

with ϕ_{SB} the Schottky barrier height, A^{**} the Richardson constant, and η the dimensionless ideality factor. The bias dependence of the corresponding Schottky resistance (inversely proportional to Eq. (D.1) is illustrated in the simulation shown in Fig. D-3. Apparent from Fig. D-3 is that the Schottky resistance is a very asymmetric function

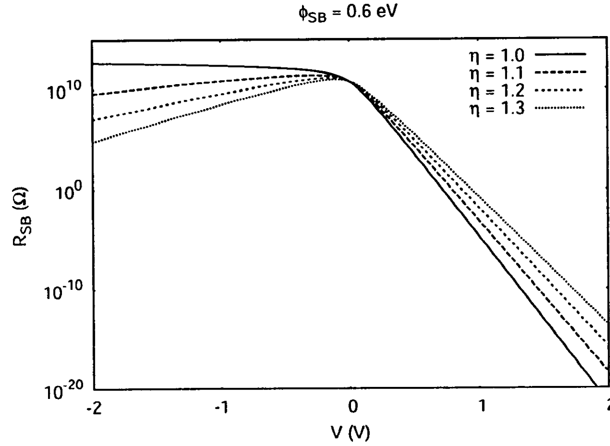

Figure D-3: Simulated Schottky barrier resistance for 4 different ideality factors. The barrier height $\phi_{TB} = 0.6$ eV. The junction area is 120×240 μm^2.

of applied bias. Ideality factors larger than one reduce the asymmetry somewhat. The Schottky barrier height will vary in general with voltage. In the case of both a tunnel and Schottky barrier, the relative capacitances of the barriers determine this variation. In general there will be interface states present at the tunnel barrier-silicon interface. These interface states tend to pin the Schottky barrier height. The bias

dependence of the Schottky barrier height is given by[151]

$$\phi_{SB} = \phi_{SB0} - \frac{C_t V_{TB} - C_s V_{SB}}{C_t + C_s + e^2 D_{ss}}, \tag{D.2}$$

where V_x and C_x denote the voltage and capacitance of barrier x, and D_{ss} is the density of interface states.

D.1.3 Tunnel and Schottky barriers together

Putting everything together, the parameters determining the series combination of a tunnel barrier and Schottky barrier are ϕ_{TB}, $\Delta\phi_{TB}$, the tunnel barrier thickness s, dielectric constant K_{TB}, ϕ_{SB0}, η, C_{TB}, C_{SB}, D_{ss}, R_{SC}. Although the IV fitting will extract values for each of them, considering the large number of parameters limited importance should be addressed to the results, since they may act in an equivalent way on the resulting shape of the IV curve. The influence of each of the parameters on the IV curve is plotted in Sec. D.2.5. Although the resulting individual parameters may be of little value, the conspicuously different bias dependence of the tunnel barrier and the Schottky barrier resistance allows for the extraction of the individual resistance values for each bias point, and that is what matters in determining the regime where tunneling through the tunnel barrier dominates the transport.

D.2 IV fitting of data

Using the nonlinear least squares fitting of the GNU scientific library, a fitting program has been written. The convergence is in general quite poor and often requires manually choosing the right size of the initial parameters before the program can make a good fit. Nonetheless, the obtained fits are reasonable.

D.2.1 MgO on epiwafer

The base-emitter IV of the epiwafer samples of Sec. 8.3 turned out to be difficult to fit, likely a result of the large emitter area with accompanying large spread in tunnel-barrier characteristics. It is shown in Fig. D-4. The extracted tunnel and

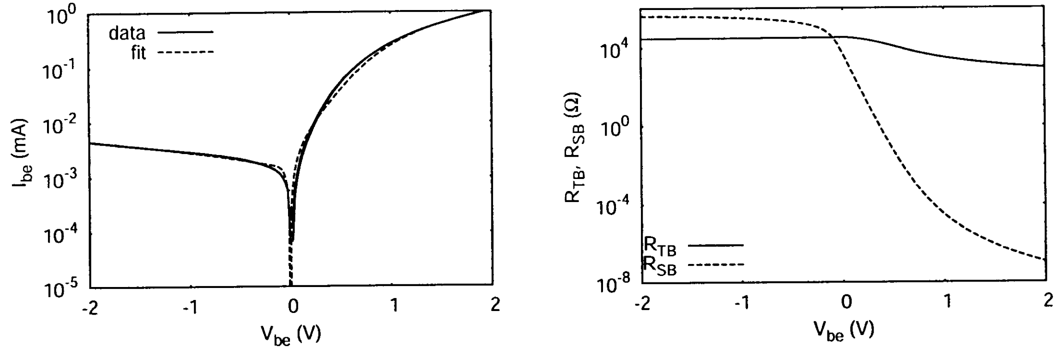

Figure D-4: IV characteristics of pn10mu_06. The tunnel barrier consists of 40 Å MgO. On the left: base-emitter plus fit. The extracted Schottky and tunnel-barrier resistances are shown on the right.

Schottky resistances in Fig. D-4 predict that the tunnel barrier dominates in forward bias, which is important to overcome the conductivity mismatch, see Sec. 1.1.

D.2.2 Thermal oxide tunnel barrier

An example of fitting the emitter-base junction of a 2nd generation transistor is shown in Fig. D-5. The tunnel barrier in Fig. D-5 consists of a 20 Å dry thermal oxide. In Fig. D-5 are also given the tunnel and Schottky resistances. Observed is that in forward bias (negative voltage on the emitter), the tunnel barrier dominates. Hence the fit predicts that the tunnel barrier dominates in the spin-injection regime. From the transistor action plots of Fig. 8-15, it is seen that the tunnel barrier sustains a reasonable voltage drop but will break down above a critical current density. It may be that the thickness of the barrier is not homogeneous, yielding a local concentration of current.

Although thermal silicon-oxide is a very good oxide for silicon, there are several

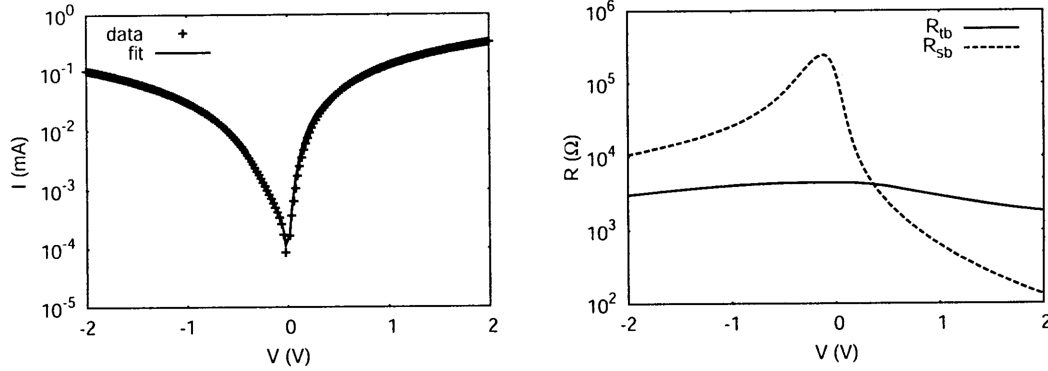

Figure D-5: Experimental IV curve of sample BJT_W14_P04_j_d01_eep21 (with an implant oxide thickness of 146 nm) and fit (left). This sample has a 20 Å thick thermal SiO_2 barrier and a WN emitter electrode. On the right is shown the extracted tunnel barrier and Schottky barrier resistance. The emitter area is 2.9×10^{-4} cm^{-2}.

practical issues involved with using it as a tunnel barrier. For instance, after growth the tunnel barrier is momentarily exposed to air while transferring to a deposition chamber for the emitter deposition. Another characteristic is described below in Sec. D.2.4.

D.2.3 Al_2O_3 tunneling barrier grown with ALD

Here the tunnel barrier characteristics of an Al_2O_3 barrier grown with atomic layer deposition (ALD) is discussed. There is likely as well a thin 3 Å thick SiO_2 barrier beneath the Al_2O_3 resulting from the time delay between the RCA clean and mounting in the ALD. The IV characteristics, together with the fit and the extracted tunnel and Schottky resistances are shown in Fig. D-6.

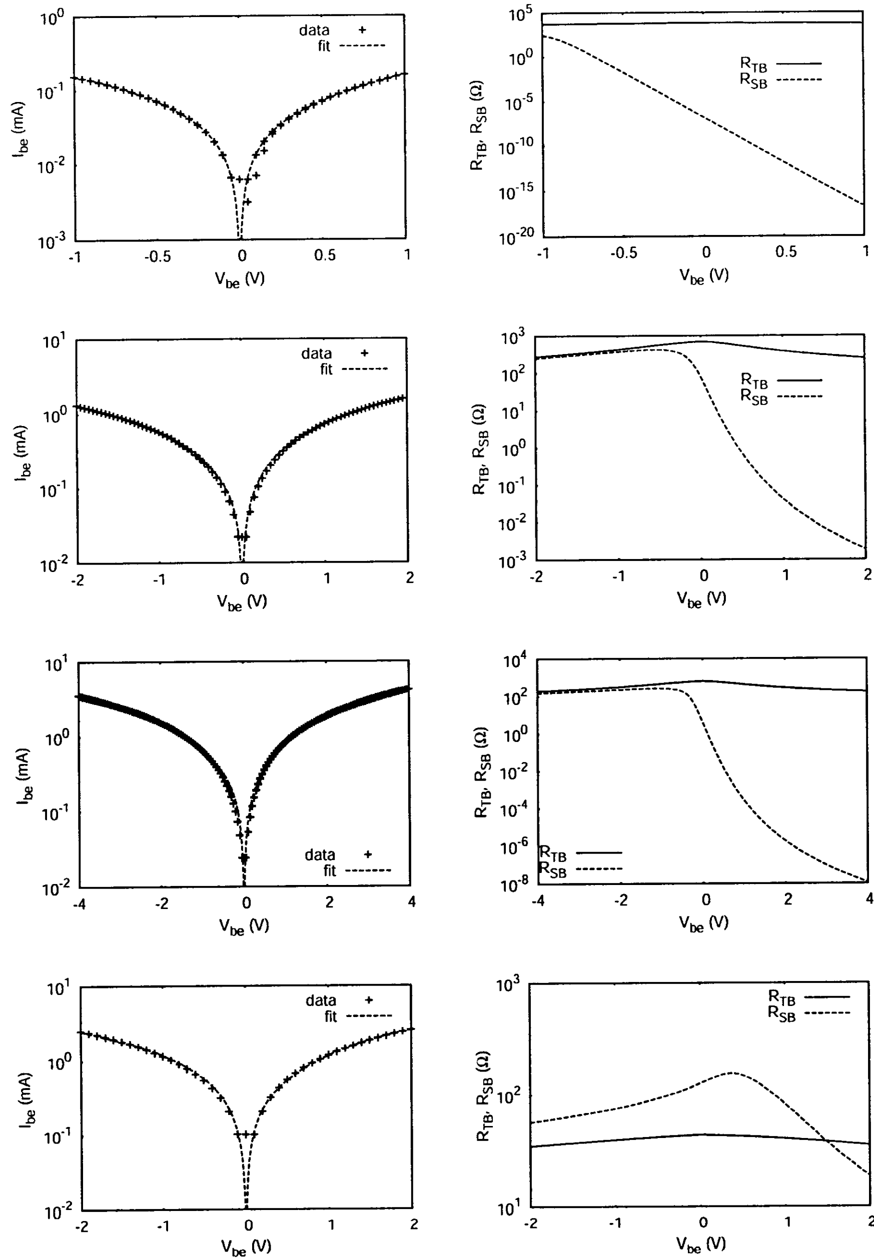

Figure D-6: Experimental IV of sample BJT_W15_P03_h_d02_eep15 (with an implant oxide thickness of 120 nm) and fit. This sample has an 18 Å thick Al_2O_3 barrier and a WN emitter electrode, deposited both with ALD and in-situ. The left side shows the IV and fit, the right the extracted tunnel barrier and Schottky barrier resistances. The curves shown are for three different stages in the tunnel barrier break down; top row: before any break down, 2nd and 3rd row: after 1st break down, 4th row: after final break down.

The IV characteristics reveal different stages in the break down of the tunnel barrier. For small bias voltages (< 2 V) the tunnel barrier is robust and dominates. Then, a first break down sets in and the tunnel barrier resistance decreases. For higher biases (> 4 V), another break down happens with a further decrease in tunnel barrier height. This two-step break down is illustrated in Fig. D-7 which shows the IV characteristics of the 2 break downs and the changing tunnel barrier resistance. This

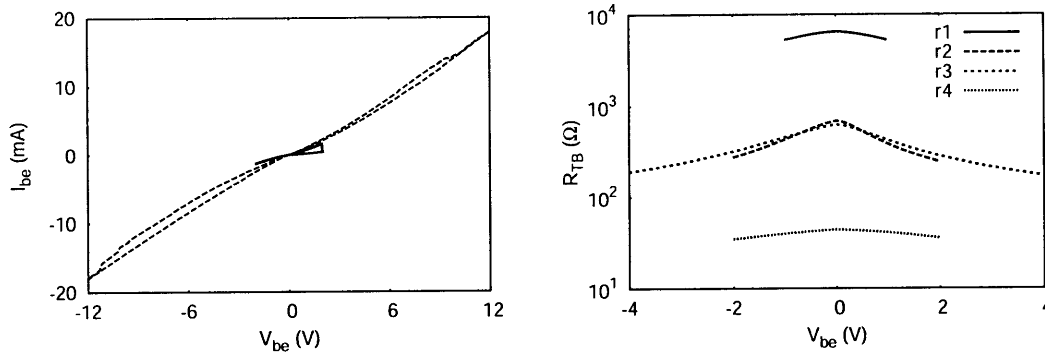

Figure D-7: IV's displaying the two stages of break down for sample BJT_W15_P03_h_d02_eep15. On the right is given the tunnel barrier resistance from each row (r) of Fig. D-6.

multistage break down may be a result of the thin native oxide present. This oxide may break down first because of a higher barrier height than the aluminum-oxide. The final break down would then correspond to that of the Al_2O_3. For the tunneling emitter bipolar transistor with this tunnel barrier, there is a significant base current, as shown in Fig. 8-17, implying that the tunnel barrier does not block valence band tunneling sufficiently (for instance because of a low barrier height) or that there are interface states that assist in recombination.

D.2.4 Resonant tunneling via an inversion layer

Some of the IV characteristics of the thermal oxide tunnel barrier display hysteretic effects. This is demonstrated in Fig. D-8. Current bistability is a feature seen in double-barrier resonant-tunneling structures [152] which consist of a quantum well

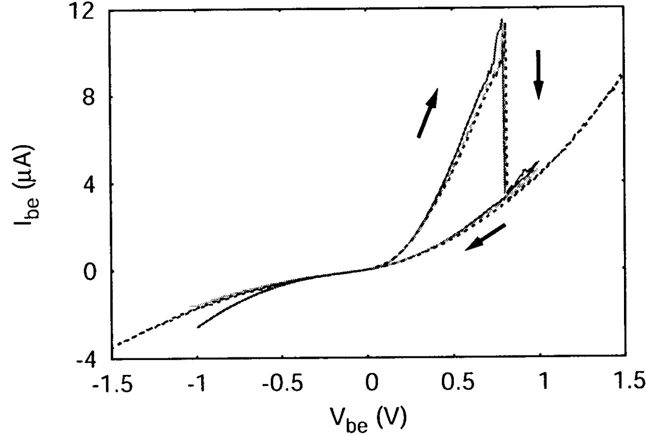

Figure D-8: Experimental IV of sample BJT_W14_P04_j_d02_eep35 (with an implant oxide thickness of 146 nm) and fit. This sample has a 20 Å thick thermal SiO_2 barrier and a WN emitter electrode. The current bistability is reproducible as shown for 3 different sweeps. The emitter area is 2.9×10^{-4} cm^{-2}.

separated by tunnel barriers on both sides. Resonant tunneling happens via the quantized states in the well; the hysteresis results from the build-up of charge inside the quantum well [153, 154]. The system of Fig. D-8 can also be a double-barrier resonant-tunneling structure, in case an inversion layer forms at the tunnel barrier-silicon interface. The double barrier then consists of the tunnel barrier and the Schottky barrier, and the inversion layer forms the quantum well. Current bistability for this system has been observed in [155] and was attributed to the filling of the quantum well states for negative voltages, that are then emptied under forward bias. For the system here, it is believed that the inversion layer itself disappears above a threshold voltage of 0.8 V. The bistability would then result from hysteresis in the formation of the inversion layer. Positive charge inside the oxide may cause such a hysteresis. Namely, postitive charge inside the tunnel barrier will assist in the formation of the inversion layer. The hysteresis then comes from the trapping of electrons at these positive charge centers for voltages above the threshold voltage for which the inversion layer disappears. Then on the downward sweep, the positive charge inside the tunnel barrier is effectively neutralized and the formation of the

inversion layer is suppressed. The negative bias then serves as the reset yielding the release of the trapped electrons and the tunnel barrier becoming positively charged again. A likely candidate for the positive charge is the dopant boron. Since the thermal oxide is grown on boron doped silicon and the silicon consumed in the process is 46%, see Sec. A.1, boron will be incorporated into the tunnel barrier. In [156] it is shown that the boron inside the oxide will be positively charged, and this charge should attract electrons to the tunnel barrier-silicon interface, hence assisting in the inversion layer formation. Therefore, the IV curve of Fig. D-8 is likely the result of resonant tunneling via an inversion layer whose formation is induced by positively charged boron trapped inside the tunnel barrier.

D.2.5 Fitting parameter influence on IV

In Figs. D-9 and D-10 is plotted the effect of changing the various fitting parameters of Sec. D.1.3 on the IV characteristics.

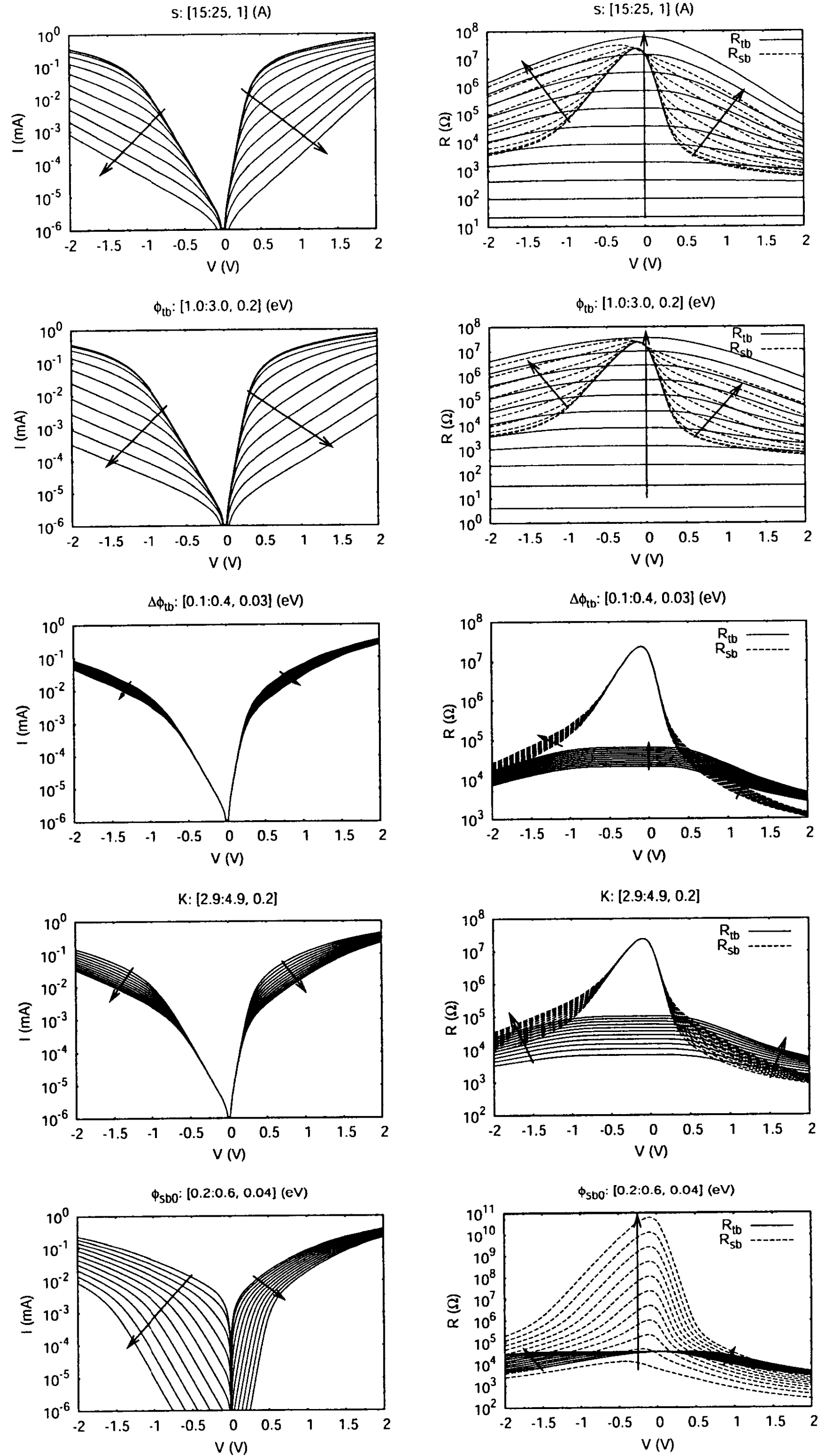

Figure D-9: 1st row: TB thickness, 2nd row: TB height, 3rd row: TB asymmetry, 4th row: TB dielectric constant, 5th row: SB height. The arrows indicate the direction of increase of the parameter (indicated in the figure heading). The junction area is $120 \times 240\ \mu\text{m}^2$.

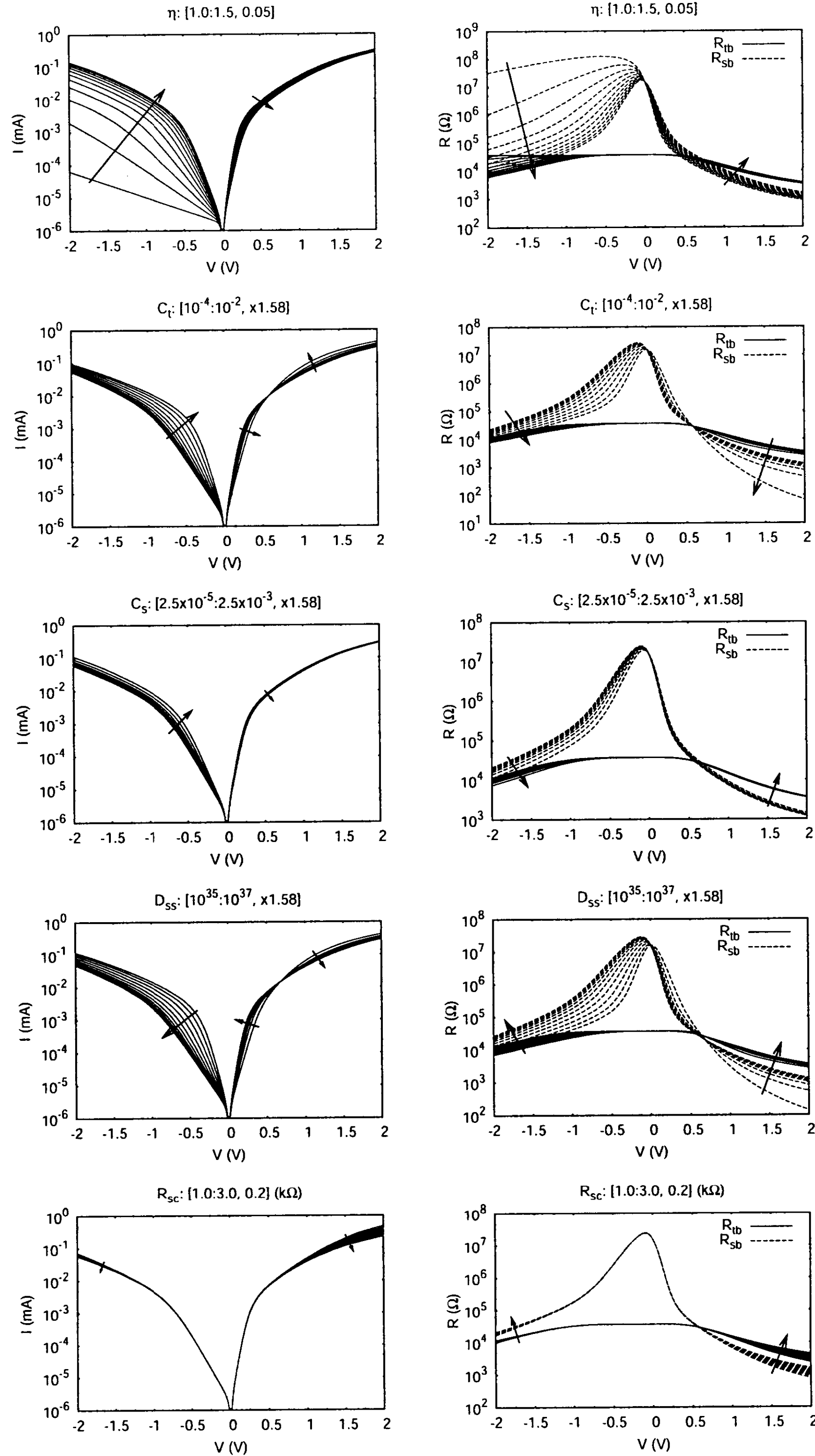

Figure D-10: 1st row: SB ideality factor, 2nd row: TB capacitance, 3rd row: SB capacitance, 4th row: SB interface states, 5th row: semiconductor series resistance. The arrows indicate the direction of increase of the parameter. The junction area is $120 \times 240\ \mu m^2$.

Appendix E

Differential magnetoresistance (DMR)

The magnetic layers of magnetic tunnel junctions consist in general of multiple magnetic domains. When such a layer changes orientation, for instance under the influence of a magnetic field, it is expected that the individual domains switch incoherently, that is one-by-one. Therefore, the magnetic state in the middle of the total magnetization reversal is in an undefined state which should have an influence on the magnetoresistance. Here an experiment will be proposed that can be used to probe this effect.

E.1 Previous results and new proposal on DMR

There are some previous results on measuring the resistance noise induced by the magnetic switching of MTJ's [157] and GMR devices[158]. The theory relating the switching to resistance noise has been developed in [158]. It basically comes down to the following. The fluctuation-dissipation theorem relates the magnetic noise spectrum to the magnetic susceptibility

$$fS_M(f) \propto \chi'', \tag{E.1}$$

where f is the frequency. The resistance noise is again correlated to the magnetic noise via the magnetoresistance

$$S_R(f) = S_M(f)(dR/dM)^2. \tag{E.2}$$

The standard noise parameter can then be expressed in terms of magnetic changes

$$\begin{aligned} \alpha(f, H) &= f S_R(f)/R^2 \propto \chi_R''(f)(dR/dM)/R^2 \\ \chi_R''(f) &= \chi(f)(dR/dM). \end{aligned} \tag{E.3}$$

$\chi_R''(f)$ is the out-of-phase component of the differential magnetoresistance, differentiated with respect to the magnetic field. In general this quantity is expected to be bias dependent since bias currents will be spin-polarized which may assist in magnetic domain switching. Hence it is sensible to consider the derivative of the quantity with respect to bias voltage as well, which in turn should be proportional to the out-of-phase component of

$$\frac{\partial^2 R}{\partial H \partial V}. \tag{E.4}$$

Hence the goal is to measure (both in- and out-of-phase components of) Eq. (E.4) to learn more about the switching behavior.

E.2 Electronics

As described in Sec. E.1, it is interesting to consider the 2$^{\text{nd}}$ derivative of the magnetoresistance (given in Eq. (E.4)) since it relates to the bias-dependent domain switching. Experimentally the derivative of a signal is measured by detecting with a lockin amplifier the response to a small ac ripple applied on top of a dc bias. The second derivative of Eq. (E.4) is then measured by looking at the combined effect of a ripple on the bias voltage and a ripple on the magnetic field. This can be done by measuring the sum-frequency of the two ripples (each with its own frequency) only. In this Section, the electronics used to single out the sum-frequency will be discussed

solely.

E.2.1 AC current source

In order to apply a ripple on top of the magnetic field, an ac current source has been built. A voltage controlled current source can of course apply both a dc and ac current simultaneously using a bias-tee setup for the input voltage. Hence the current source is designed keeping in mind the resistance of the magnet at liquid nitrogen temperatures. The target maximum output current is 1 A which gives a reasonable magnetic field range; higher currents produce too much heat.

The current source is based on the power opamp APEX PA12. The design is from David Bono and the schematic is shown in Fig. E-1.

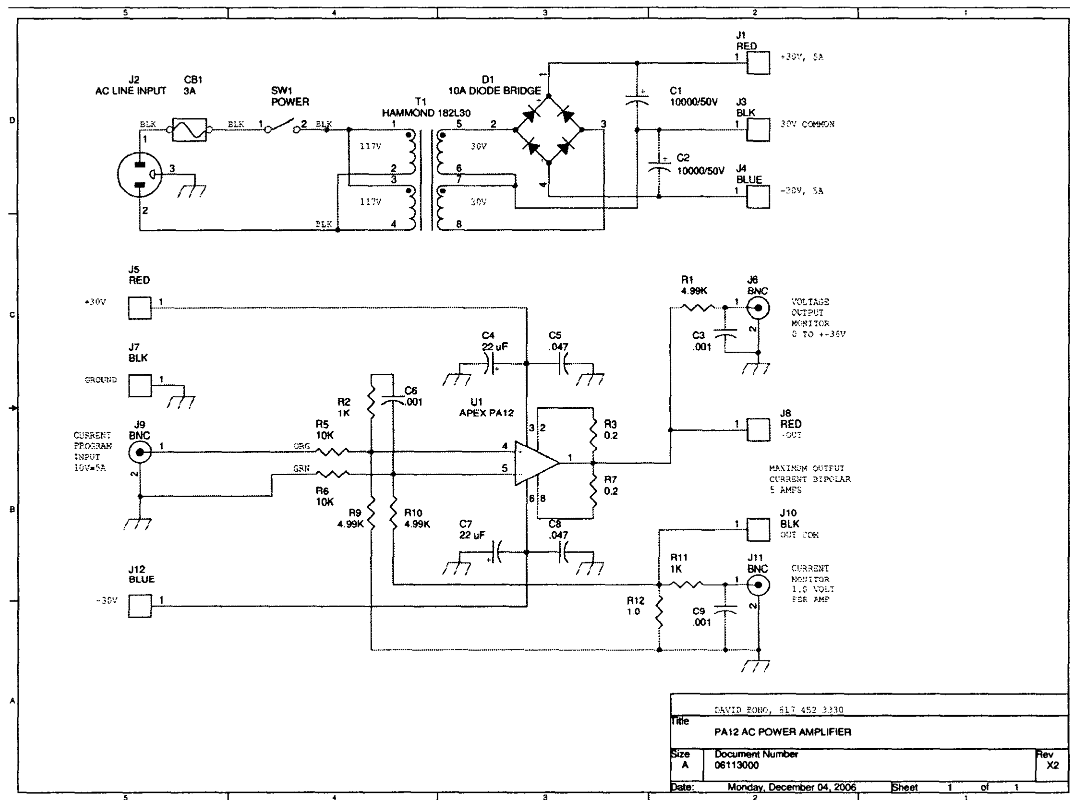

Figure E-1: AC current source based on the power opamp PA12. Designed by David Bono. It turned out to have very low noise.

E.2.2 Band-pass filter

The key is to feed a reference signal to the lockin that has the frequency *and* phase of the response to the sum-frequency. Reference signals with the sum-frequency are readily obtained with an analog multiplier which has been chosen to be the AD633 which has an excellent response over the frequency range 10 – 1000 Hz. The output signal of the multiplier will contain several frequencies, namely, the sum- and difference-frequency as well as the individual input frequencies. The task is then to single out only the sum-frequency without destroying the phase information. This can be done with a bandpass filter[1] which, if tuned at resonance, produces zero phase shift. As a bandpass filter is chosen the state-variable filter [159] depicted in Fig. E-2. The state-variable filter acts simultaneously as a high-pass, band-pass, and low-pass

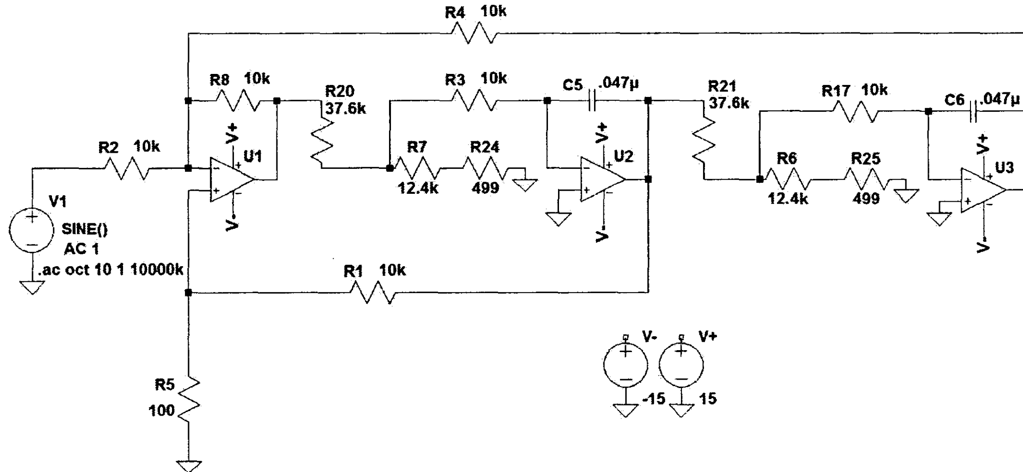

Figure E-2: State-variable filter circuit made with LTspice.

filter, depending on which output is taken (in Fig. E-2: output of left, middle, and right opamp [160], respectively). Here, only the band-pass output is relevant. The resonance frequency of the filter can be tuned by introducing a dual-ganged potentiometer, for the two 12.4 kΩ resistances of Fig. E-2, which form potential dividers with the 499 Ω resistors. An additional frequency tuning can be obtained by adding another dual-ganged potentiometer in a potential divider setup, but now with a 1 MΩ

[1]Suggested by David Bono

resistor instead of the 499 Ω resistor[2]. In this way the resonance frequency can be tuned accurately. An example of the simulated output of the band-pass filter is shown in Fig. E-3, together with the measured frequency spectrum as obtained with a spectrum analyzer (HP35670A). It can be observed from Fig. E-3 that the built

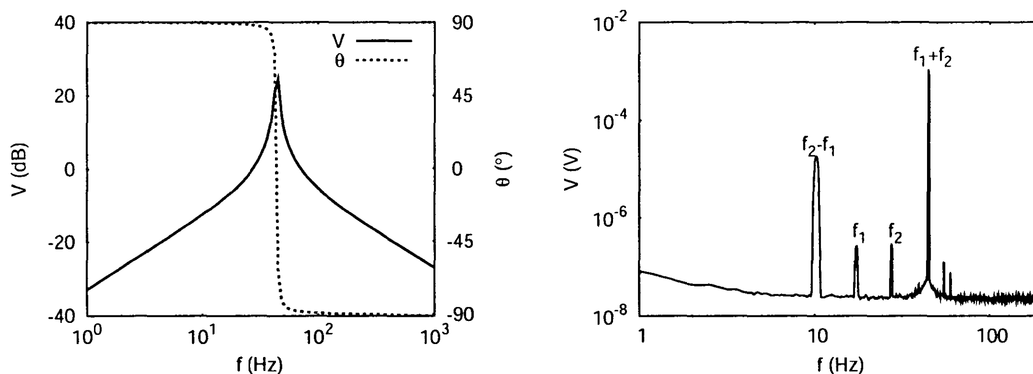

Figure E-3: The output of the band-pass filter Fig. E-2 as simulated with LTspice is shown on the left; on the right is given the measured frequency spectrum of the built electronics (analog multiplier plus band-pass filter).

electronics works quite well. The lockin amplifier is able to lock to the sum-frequency without any drift in phase.

[2]Ideas of David Bono

Bibliography

[1] Igor Žutić, Jaroslav Fabian, and S. Das Sarma. Spintronics: Fundamentals and applications. *Rev. Mod. Phys.*, 76:323–410, 2004.

[2] Mark Johnson and R. H. Silsbee. Interfacial charge-spin coupling: Injection and detection of spin magnetization in metals. *Phys. Rev. Lett.*, 55:1790–1793, 1985.

[3] M. N. Baibich, J. M. Broto, A. Fert, F. Nguyen Van Dau, F. Petroff, P. Eitenne, G. Creuzet, A. Friederich, and J. Chazelas. Giant magnetoresistance of (001)fe/(001)cr magnetic superlattices. *Phys. Rev. Lett.*, 61:2472–2475, 1988.

[4] G. Schmidt, D. Ferrand, L. W. Molenkamp, A. T. Philip, and B. J. van Wees. Fundamental obstacle for electrical spin injection from a ferromagnetic metal into a diffusive semiconductor. *Phys. Rev. B*, 62:R4790–4793, 2000.

[5] E. I. Rashba. Theory of electrical spin injection: Tunnel contacts as a solution of the conductivity mismatch problem. *Phys. Rev. B*, 62:16267(R), 2000.

[6] D. L. Smith and R. N. Silver. Theory of spin injection into semiconductors. *Phys. Rev. B*, 64:045323, 2001.

[7] X. Hao, J. S. Moodera, and R. Meservey. Spin-filter effect of ferromagnetic europium sulfide tunnel barriers. *Phys. Rev. B*, 42:8235–8243, 1990.

[8] W. H. Butler, X.-G. Zhang, T. C. Schulthess, and J. M. MacLaren. Spin-dependent tunneling conductance of fe/mgo/fe sandwiches. *Phys. Rev. B*, 63:054416, 2001.

[9] J. S. Moodera, Lisa R. Kinder, Terrilyn M. Wong, and R. Meservey. Large magnetoresistance at room temperature in ferromagnetic thin film tunnel junctions. *Phys. Rev. Lett.*, 74:3273–3276, 1995.

[10] M. Julliere. Tunneling between ferromagnetic films. *Phys. Lett. A*, 54:225–226, 1975.

[11] J. D. Albrecht and D. L. Smith. Electrical spin injection at a schottky contact. *Phys. Rev. B*, 66:113303, 2002.

[12] S. A. Wolf, D. D. Awschalom, R. A. Buhrman, J. M. Daughton, S. von Molnár, M. L. Roukes, A. Y. Chtchelkanova, and D. M. Treger. Spintronics: A spin-based electronics vision for the future. *Science*, 294:1488–1495, 2001.

[13] R. Fiederling, M. Keim, G. Reuscher, W. Ossau, G. Schmidt, A. Waag, and L. W. Molenkamp. Injection and detection of a spin-polarized current in a light-emitting diode. *Nature*, 402:787–790, 1999.

[14] Y. Ohno, D. K. Young, B. Beschoten, F. Matsukara, H. Ohno, and D. D. Awschalom. Electrical spin injection in a ferromagnetic semiconductor heterostructure. *Nature*, 402:790–792, 1999.

[15] M. I. D'yakonov and V. I. Perel. *Optical Orientation.* North-Holland, Amsterdam, 1984.

[16] B. T. Jonker, Y. D. Park, B. R. Bennett, H. D. Cheong, G. Kioseoglou, and A. Petrou. Robust electrical spin injection into a semiconductor heterostructure. *Phys. Rev. B*, 62:8180–8183, 2000.

[17] A. T. Hanbicki, B. T. Jonker, G. Itskos, G. Kioseoglou, and A. Petrou. Efficient electrical spin injection from a magnetic metal/tunnel barrier contact into a semiconductor. *Appl. Phys. Lett.*, 80:1240, 2002.

[18] O. M. J. van 't Erve, G. Kioseoglou, A. T. Hanbicki, C. H. Li, B. T. Jonker, R. Mallory, M. Yasar, and A. Petrou. Comparison of fe/schottky and fe/al2o3 tunnel barrier contacts for electrical spin injection into gaas. *Appl. Phys. Lett.*, 84:4334, 2004.

[19] V. F. Motsnyi, J. De Boeck, J. Das, W. Van Roy, G. Borghs, E. Goovaerts, and V. I. Safarov. Electrical spin injection in a ferromagnet/tunnel barrier/semiconductor heterostructure. *Appl. Phys. Lett.*, 81:265, 2002.

[20] X. Jiang, R. Wang, R. M. Shelby, R. M. Macfarlane, S. R. Bank, J. S. Harris, and S. S. P. Parkin. Highly spin polarized room temperature tunnel injector for semiconductor spintronics using mgo (100). *Phys. Rev. Lett.*, 94:056601, 2005.

[21] H. J. Zhu, M. Ramsteiner, H. Kostial, M. Wassermeier, H.-P. Schönherr, and K. H. Ploog. Room-temperature spin injection from fe into gaas. *Phys. Rev. Lett.*, 87:016601, 2001.

[22] J. Stephens, J. Berezovsky, J. P. McGuire, L. J. Sham, A. C. Gossard, and D. D. Awschalom. Spin accumulation in forward-biased mnas/gaas schottky diodes. *Phys. Rev. Lett.*, 93:097602, 2004.

[23] Z. G. Yu and M. E. Flatté. Electric-field dependent spin diffusion and spin injection into semiconductors. *Phys. Rev. B*, 66:201202(R), 2002.

[24] Z. G. Yu and M. E. Flatté. Spin diffusion and injection in semiconductor structures: Electric field effects. *Phys. Rev. B*, 66:235302, 2002.

[25] Y. Qi and S. Zhang. Spin diffusion at finite electric and magnetic fields. *Phys. Rev. B*, 67:052407, 2003.

[26] I. D'Amico. Spin injection and electric-field effect in degenerate semiconductors. *Phys. Rev. B*, 69:165305, 2004.

[27] S. A. Crooker, M. Furis, X. Lou, C. Adelmann, D. L. Smith, C. J. Palmstrøm, and P. A. Crowell. Imaging spin transport in lateral ferromagnet/semiconductor structures. *Science*, 309:2191–2195, 2005.

[28] M. Ramsteiner, H. Y. Hao, A. Kawaharazuka, H. J. Zhu, M. Kästner, R. Hey, L. Däweritz, H. T. Grahn, and K. H. Ploog. Electrical spin injection from ferromagnetic mnas metal layers into gaas. *Phys. Rev. B*, 66:081304(R), 2002.

[29] R. M. Stroud, A. T. Hanbicki, Y. D. Park, G. Kioseoglou, A. G. Petukhov, B. T. Jonker, G. Itskos, and A. Petrou. Reduction of spin injection efficiency by interface defect spin scattering in znmnse/algaas spin-polarized light-emitting diodes. *Phys. Rev. Lett.*, 89:166602, 2002.

[30] J. Strand, B. D. Schultz, A. F. Isakovic, C. J. Palmstrøm, and P. A. Crowell. Dynamic nuclear polarization by electrical spin injection in ferromagnet-semiconductor heterostructures. *Phys. Rev. Lett.*, 91:036602, 2003.

[31] P. van Dorpe, W. Van Roy, J. De Boeck, and G. Borghs. Nuclear spin orientation by electrical spin injection in an alxga1-xas/gaas spin-polarized light-emitting diode. *Phys. Rev. B*, 72:035315, 2005.

[32] J. Strand X. Lou C. Adelmann, B. D. Schultz, A. F. Isakovic, C. J. Palmstrøm, and P. A. Crowell. Electron spin dynamics and hyperfine interactions in fe/al0.1ga0.9as/gaas spin injection heterostructures. *Phys. Rev. B*, 72:155308, 2005.

[33] V. F. Motsnyi, P. Van Dorpe, W. Van Roy, E. Goovaerts, V. I. Safarov, G. Borghs, and J. De Boeck. Optical investigation of electrical spin injection into semiconductors. *Phys. Rev. B*, 68:245319, 2003.

[34] J. M. Kikkawa, I. P. Smorchkova, N. Samarth, and D. D. Awschalom. Room-temperature spin memory in two-dimensional electron gases. *Science*, 277:1284–1288, 1997.

[35] C. Adelmann, X. Lou, J. Strand, C. J. Palmstrøm, and P. A. Crowell. Spin injection and relaxation in ferromagnet-semiconductor heterostructures. *Phys. Rev. B*, 71:121301, 2005.

[36] Lorenz Meier, Gian Salis, Ivan Shorubalko, Emilio Gini, Silke Schön, and Klaus Ensslin. Measurement of rashba and dresselhaus spin-orbit magnetic fields. *Nature Physics*, 3:650–654, 2007.

[37] G. Dresselhaus. Spin-orbit coupling effects in zinc blende structures. *Phys. Rev*, 100:580, 1955.

[38] Y. U. Bychkov and E. I. Rashba. Oscillatory effects and the magnetic susceptibility of carriers in inversion layers. *J. Phys. C*, 17:6039, 1984.

[39] Y. Kato, R. C. Myers, A. C. Gossard, and D. D. Awschalom. Coherent spin manipulation without magnetic fields in strained semiconductors. *Nature*, 427:50–53, 2003.

[40] Y. Kato, R. C. Myers, A. C. Gossard, and D. D. Awschalom. Current-induced spin polarization in strained semiconductors. *Phys. Rev. Lett.*, 93:176601, 2004.

[41] S. A. Crooker and D. L. Smith. Imaging spin flows in semiconductors subject to electric, magnetic, and strain fields. *Phys. Rev. Lett.*, 94:236601, 2005.

[42] M. Hruška, Š. Kos, S. A. Crooker, A. Saxena, and D. L. Smith. Effects of strain, electric, and magnetic fields on lateral electron-spin transport in semiconductor epilayers. *Phys. Rev. B*, 73:075306, 2006.

[43] Junsaku Nitta, Tatsushi Akazaki, Hideaki Takayanagi, and Takatomo Enoki. Gate control of spin-orbit interaction in an inverted $In_{0.53}Ga_{0.47}As/In_{0.52}Al_{0.48}As$ heterostructure. *Phys. Rev. Lett.*, 78:1335, 1997.

[44] Takaaki Koga, Junsaku Nitta, Tatsushi Akazaki, and Hideaki Takayanagi. Rashba spin-orbit coupling probed by the weak antilocalization analysis in inalas/ingaas/inalas quantum wells as a function of quantum well asymmetry. *Phys. Rev. Lett.*, 89:046801, 2002.

[45] S. Datta and B. Das. Electronic analog of the electro-optic modulator. *Appl. Phys. Lett.*, 56:665, 1989.

[46] Hyun Cheol Koo, Jae Hyun Kwon, Jonghwa Eom, Joonyeon Chang, Suk Hee Han, and Mark Johnson. Control of spin precession in a spin-injected field effect transistor. *Science*, 325:1515–1518, 2009.

[47] P. R. Hammar, B. R. Bennett, M. J. Yang, and Mark Johnson. Observation of spin injection at a ferromagnet-semiconductor interface. *Phys. Rev. Lett.*, 83:203, 1999.

[48] P. R. Hammar and M. Johnson. Detection of spin-polarized electrons injected into a two-dimensional electron gas. *Phys. Rev. Lett.*, 88:066806, 2002.

[49] X. Lou, C. Adelmann, M. Furis, S. A. Crooker, C. J. Palmstrøm, and P. A. Crowell. Electrical detection of spin accumulation at a ferromagnet-semiconductor interface. *Phys. Rev. Lett.*, 96:176603, 2006.

[50] Xiaohua Lou, Christoph Adelmann, Scott A. Crooker, Eric S. Garlid, Jianjie Zhang, K. S. Madhukar Reddy, Soren D. Flexner, Chris J. Palmstrøm, and Paul A. Crowell. Electrical detection of spin transport in lateral ferromagnet-semiconductor devices. *Nature*, 3:197–202, 2007.

[51] W Hanle. Uber magnetische beeinflussung der polarisation der resonanzfluoreszenz. *Z. Phys.*, 30:93, 1924.

[52] Berend T. Jonker, George Kioseoglou, Aubrey T. Hanbicki, Connie H. Li, and Phillip E. Thompson. Electrical spin-injection into silicon from a ferromagnetic metal/tunnel barrier contact. *Nature Physics*, 3:542–548, 2007.

[53] Louis Costa, Markus Betz, Marko Spasenović, Alan D. Bristow, and Henry M. van Driel. All-optical injection of ballistic electrical currents in unbiased silicon. *Nature Physics*, 3:632–635, 2007.

[54] R. D. R. Bhat and J. E. Sipe. Optically injected spin currents in semiconductors. *Phys. Rev. Lett.*, 85:5432, 2000.

[55] Igor Žutić, Jaroslav Fabian, and Steven C. Erwin. Spin injection and detection in silicon. *Phys. Rev. Lett.*, 97:026602, 2006.

[56] Ian Appelbaum, Biqin Huang, and Douwe J. Monsma. Electronic measurement and control of spin transport in silicon. *Nature*, 447:295–298, 2007.

[57] O. M. J. van 't Erve, A. T. Hanbicki, M. Holub, C. H. Li, C. Awo-Affouda, P. E. Thompson, and B. T. Jonker. Electrical injection and detection of spin-polarized carriers in silicon in a lateral transport geometry. *Appl. Phys. Lett.*, 91:212109, 2007.

[58] Y. Ando, K. Hamaya, K. Kasahara, Y. Kishi, K. Ueda, K. Sawano, T. Sawano, T. Sadoh, and M. Miyao. Electrical injection and detection of spin-polarized electrons in silicon through a Fe_3Si/Si schottky tunnel barrier. *Appl. Phys. Lett.*, 94:182105, 2009.

[59] Saroj P. Dash, Sandeep Sharma, Ram S. Patel, Michel P. de Jong, and Ron Jansen. Electrical creation of spin polarization in silicon at room temperature. *Nature*, 462:491–494, 2009.

[60] Biqin Huang, Douwe J. Monsma, and Ian Appelbaum. Coherent spin transport through a 350 micron thick silicon wafer. *Phys. Rev. Lett.*, 99:177209, 2007.

[61] A. E. Dementyev, D. G. Cory, and C. Ramanathan. Dynamic nuclear polarization in silicon microparticles. *Phys. Rev. Lett.*, 100:127601, 2008.

[62] Ron Jansen, Byoung-Chul Min, and Saroj P. Dash. Oscillatory spin-polarized tunneling from silicon quantum wells controlled by electric field. *Nature Materials*, 2605, 2009.

[63] G. Schmidt, C. Gould, P. Grabs, A. M. Lunde, G. Richter, A.. Slobodskyy, and L. W. Molenkamp. Spin injection in the nonlinear regime: Band bending effects. *Phys. Rev. Lett.*, 92:226602, 2004.

[64] Igor Žutić, Jaroslav Fabian, and S. Das Sarma. Spin injection through the depletion layer: A theory of spin-polarized p-n junctions and solar cells. *Phys. Rev. B*, 64:121201, 2001.

[65] Jaroslav Fabian, Igor Žutić, and S. Das Sarma. Theory of spin-polarized bipolar transport in magnetic p-n junctions. *Phys. Rev. B*, 66:165301, 2002.

[66] Peifeng Chen, Juergen Moser, Philipp Kotissek, Janusz Sadowski, Marcus Zenger, Dieter Weiss, and Werner Wegscheider. All electrical measurement of spin injection in a magnetic p-n junction diode. *Phys. Rev. B*, 74:241302(R), 2006.

[67] H. Saito, S. Yuasa, K. Ando, Y. Hamada, and Y. Suzuki. Spin polarized tunneling in metal-insulator-semiconductor fe/zn/ga1-xmnxas magnetic tunnel diodes. *Appl. Phys. Lett.*, 89:232502, 2006.

[68] Jaroslav Fabian and Igor Žutić. Spin-polarized current amplification and spin injection in magnetic bipolar transistors. *Phys. Rev. B*, 69:115314, 2004.

[69] Y. B. Xu, E. T. M. Kernohan, D. J. Freeland, A. Ercole, M. Tselepi, and J. A. C. Bland. Evolution of the ferromagnetic phase of ultrathin fe films grown on gaas(100)-46. *Phys. Rev. B*, 58:890, 1998.

[70] Igor Žutić, Jaroslav Fabian, and S. Das Sarma. Spin polarized transport in inhomogeneous magnetic semiconductors: Theory of magneti/nonmagnetic p-n junctions. *Phys. Rev. Lett.*, 88:066603, 2002.

[71] Igor Žutić, Jaroslav Fabian, and S. Das Sarma. Proposal for a spin-polarized solar battery. *Appl. Phys. Lett.*, 79:1558, 2001.

[72] M. E. Flatté, Z. G. Yu, E. Johnston-Halperin, and D. D. Awschalom. Theory of semiconductor magnetic bipolar transistors. *Appl. Phys. Lett.*, 82:4740, 2003.

[73] N. Lebedeva and P. Kuivalainen. Modelling of ferromagnetic semiconductor devices for spintronics. *J. Appl. Phys.*, 93:9845, 2003.

[74] G. X. Miao, J. Y. Chang, M. J. van Veenhuizen, K. Thiel, M. Seibt, G. Eilers, M. Münzenberg, and J. S. Moodera. Epitaxial growth of mgo and fe/mgo/fe magnetic tunnel junctions on (100)-si by molecular beam epitaxy. *Appl. Phys. Lett.*, 93:142511, 2008.

[75] CrystalMaker Software Ltd.

[76] Charles Kittel. *Introduction to Solid State Physics.* John Wiley & Sons, Inc., 7 edition, 1996.

[77] Robert Hull. *Properties of crystalline silicon.* INSPEC, 1999.

[78] Ph. Mavropoulos, N. Papanikolaou, and P. H. Dederichs. Complex band structure and tunneling through ferromagnet/insulator/ferromagnet junctions. *Phys. Rev. Lett.*, 85:1088, 2000.

[79] Mildred S. Dresselhaus, Gene Dresselhaus, and Ado Jorio. *Group theory - Applications to the Physics of Condensed Matter.* Springer, 2008. Chapter 10.

[80] M. Ning, Y. Y. Mi, C. K. Ong, P. C. Lim, and S. J. Wang. Growth studies of (220), (200), and (111) oriented mgo films on si (001) without buffer layer. *J. Phys. D: Appl. Phys.*, 40:3678–3682, 2007.

[81] V. V. Osipov, N. A. Viglin, and A. A. Samokhvalov. Investigation of heterostructure "ferromagnetic semiconductor-semiconductor" in the millimeter and submillimeter microwave range. *Phys. Lett. A*, 247:353–359, 1998.

[82] Charles P. Poole. *Electron spin resonance: a comprehensive treatise on experimental techniques.* Dover publications, 1996.

[83] Z. G. Yu and M. G. Flatté. Electric-field dependent spin diffusion and spin injection into semiconductors. *Phys. Rev. B*, 66:021202(R), 2002.

[84] Grant R. Fowles. *Introduction to modern optics.* Dover publications, Inc, New York, 2 edition, 1975.

[85] Peter Ashburn. *Design and realization of bipolar transistors.* John Wiley & Sons, 1988.

[86] Gerold W. Neudeck. *The PN junction diode*, volume 2 of *Modular series on solid state devices.* Addison-Wesley, 2 edition, 1989.

[87] S. M. Sze and Kwok K. NG. *Physics of semiconductor devices.* John Wiley & Sons, 3 edition, 2007. Chapter 8.3.

[88] K. M. Eisele. SF_6, a preferable etchant for plasma etching silicon. *J. Electrochem. Soc.: Solid-State Science and Technology*, 128:123–126, 1981.

[89] L. J. Klein, K. L. M. Lewis, K. A. Slinker, Srijit Goswami, D. W. van der Weide, R. H. Blick, P. M. Mooney, J. O. Chu, S. N. Coppersmith, Mark Friesen, and M. A. Eriksson. Quantum dots and etch-induced depletion of a silicon two-dimensional electron gas. *J. Appl. Phys.*, 99:023509, 2006.

[90] Brigham Young University. Resistivity and mobility calculator.

[91] Martin A. Green and R. Bruce Godfrey. Super-gain silicon mis heterojunction emitter transistors. *IEEE Electron Device Letters*, 7:225–227, 1983.

[92] Kyoung H. Kim, Damon B. Farmer, Jean-Sebastien M. Lehn, P. Venkateswara Rao, and Roy G. Gordon. Atomic layer deposition of gadolinium scandate films with high dielectric constant and low leakage current. *Appl. Phys. Lett.*, 89:133512, 2006.

[93] L. Esaki. New phenomenon in narrow germanium p-n junctions. *Phys. Rev.*, 109:603–604, 1958.

[94] Marc van Veenhuizen, Nicolas Locatelli, Joonyeon Chang, and Jagadeesh Moodera. Observation of negative differential transconductance in tunneling emitter bipolar transistors. *Appl. Phys. Lett.*, 95:072102, 2009.

[95] H. Morkoç, J. Chen, K. Reddy, and T. Henderson. Observation of a negative differential resistance due to tunneling through a single barrier into a quantum well. *Appl. Phys. Lett.*, 49:70–72, 1986.

[96] P. Bedrossian, D. M. Chen, K. Mortensen, and J. A. Golovchenko. Demonstration of the tunnel-diode effect on an atomic scale. *Nature*, 342:258–260, 1989.

[97] D. D. D. Ma, Y. G. Wang, L. Lu, C. S. Lee, and S. T. Lee. Negative differential resistance in scanning-tunneling spectroscopy of diamond films. *Appl. Phys. Lett.*, 80:1231–1233, 2002.

[98] Z. H. Lu, R. S. Khangura, M. W. C. Dharma-wardana, M. Z. Zgierski, and D. Ritchie. Molecular electronics, negative differential resistance, and resonant tunneling in a poled molecular layer on al/ lif electrodes having a sharp density of states. *Appl. Phys. Lett.*, 85:323–325, 2004.

[99] F. Beltram, F. Capasso, S. Luryi, S.-N. G. Chu, A. Y. Cho, and D. L. Sivco. Negative transconductance via gating of the quantum well subbands in a resonant tunneling transistor. *Appl. Phys. Lett.*, 53:219–221, 1988.

[100] Z. Yu and R. W. Dutton. Gummel plot nonlinearities in polysilicon emitter transistors-including negative differential resistance behavior. *IEEE Electron Device Letters*, 6:507–509, 1985.

[101] F. Capasso and R. A. Kiehl. Resonant tunneling transistor with quantum well base and high-energy injection: A new negative differential resistance device. *J. Appl. Phys.*, 58:1366, 1985.

[102] H. Kisaki. Tunnel transistor. *Proc. IEEE*, 61:1053–1055, 1973.

[103] M. N. Feiginov. Negative differential conductance in the tunnel schottky contact with two-dimensional channel. *Appl. Phys. Lett.*, 81:930–932, 2002.

[104] Stefan Rein. *Lifetime spectroscopy: a method of defect characterization in silicon for photovoltaic applications.* Springer, New York, 2005. Chapter 1.2.

[105] John D. Cressler and Guofo Niu. *Silicon-Germanium Heterojunction Bipolar Transistors*. Artech House, 2003. Chapter 9.

[106] D. B. M. Klaassen, J. W. Slotboom, and H. C. de Graaff. Unified apparent bandgap narrowing in n- and p-type silicon. *Solid-State Elect.*, 35:125–129, 1992.

[107] F. E. Najjar, D. C. Radulescu, Y.-K. Chen, G. W. Wicks, P. J. Tasker, and L. F. Eastman. dc characterization of the algaas/gaas tunneling emitter bipolar transistor. *Appl. Phys. Lett.*, 50:1915, 1987.

[108] T. H. Chiu and A. F. J. Levi. Electron transport in an alsb/inas/gasb tunnel emitter hot-electron transistor. *Appl. Phys. Lett.*, 55:1891, 1989.

[109] Chun-Yuan Chen, Shiou-Ying Cheng, Hung-Ming Chuang, Jing-Yuy Chen, Ssu-I Fu, Ching-Hsiu Tsai, Chi-Yuan Chang, Ching-Wen Hung, Chun-Wei Chen, and Wen-Chau Liu. Dc characterization of an inp/ingaas tunneling emitter bipolar transistor (tebt). *Proc. SPIE*, 5274:425–432, 2004.

[110] Tomomi Yoshimoto, Kazuhiko Matsumoto, Kunihiro Sakamoto, and Toshimiti Sakata. Si metal insulator semiconductor tunnel emitter transistor (si mis tet). *Japan. J. Appl. Phys.*, 30:2012–2014, 1991.

[111] Tomomi Yoshimoto and Kazuo Suzuki. A high current gain si metal insulator semiconductor tunnel emitter transistor. *Japan. J. Appl. Phys.*, 32:180–182, 1993.

[112] Ian R. C. Post, Peter Ashburn, and Graham R. Wolstenholme. Polysilicon emitters for bipolar transistors: A review and re-evaluation of theory and experiment. *IEEE Transactions on Electron Devices*, 39:1717–1731, 1992.

[113] T. H. Ning and D. D. Tang. Method for determining the emitter and base series resistances of bipolar transistors. *IEEE Transactions on Electron Devices*, 31:409–412, 1984.

[114] J. E. Lary and R. L. Anderson. Effective base resistance of bipolar transistors. *IEEE Transactions on Electron Devices*, 32:2503–2505, 1985.

[115] F. Ingvarson, M. Linder, and K. O. Jeppson. Extraction of the base and emitter resistances in bipolar transistors using an accurate base resistance model. *IEEE Transactions on Semiconductor Manufacturing*, 16:228–232, 2003.

[116] E. I. Rashba. *Fiz. Tverd. Tela (Leningrad)*, 2:1224, 1960. [Sov. Phys. Solid State **2**, 1109 (1960)].

[117] Y. Aharonov and D. Bohm. *Phys. Rev.*, 115:485, 1959.

[118] Y. Aharonov and A. Casher. Topological quantum effects for neutral particles. *Phys. Rev. Lett.*, 53:319, 1984.

[119] M. Koenig, A. Tschetschetkin, E. M. Hankiewicz, J. Sinova, V. Hock, V. Daumer, M. Schaefer, C. R. Becker, H. Buhmann, and L. W. Molenkamp. Direct observation of the aharonov-casher phase. *Phys. Rev. Lett.*, 96:076804, 2006.

[120] T. Bergsten, T. Kobayashi, Y. Sekine, and J. Nitta. Experimental demonstration of the time reversal aharonov-casher effect. *Phys. Rev. Lett.*, 97:196803, 2006.

[121] J. Nitta, F. E. Meijer, and H. Takayanagi. Spin-interference device. *Appl. Phys. Lett.*, 75:695, 1999.

[122] D. Frustaglia and K. Richter. Spin interference effects in ring conductors subject to rashba coupling. *Phys. Rev. B*, 69:235310, 2004.

[123] M. J. van Veenhuizen, T. Koga, and J. Nitta. Spin-orbit induced interference of ballistic electrons in polygon structures. *Phys. Rev. B*, 73:235315, 2006.

[124] B. Molnár, F. M. Peeters, and P. Vasilopoulos. Spin-dependent magnetotransport through a ring due to spin-orbit interaction. *Phys. Rev. B*, 69:155335, 2004.

[125] U. Aeberhard, K. Wakabayashi, and M. Sigrist. Effect of spin-orbit coupling on zero-conductance resonances in asymmetrically coupled one-dimensional rings. *Phys. Rev. B*, 72:075328, 2005.

[126] R. Citro, F. Romeo, and M. Marinaro. Zero-conductance resonances and spin filtering effects in ring conductors subject to rashba coupling. *Phys. Rev. B*, 74:115329, 2006.

[127] P. Lucignano, D. Giuliano, and A. Tagliacozzo. Quantum rings with rashba spin-orbit coupling: A path-integral approach. *Phys. Rev. B*, 76:045324, 2007.

[128] B. L. Al'tshuler, A. G. Aronov, and B. Z. Spivak. *Pis'ma Zh. Eksp. Teor. Fiz.*, 33:101, 1981. [JETP Lett. **33**, 94 (1981)].

[129] H. Mathur and A. D. Stone. Quantum transport and the electronic aharonov-casher effect. *Phys. Rev. Lett.*, 68:2964, 1992.

[130] A. D. Stone and Y. Imry. Periodicity of the aharonov-bohm effect in normal-metal rings. *Phys. Rev. Lett.*, 56:189, 1986.

[131] O. Kálmán, P. Földi, M. G. Benedict, and F. M. Peeters. Magnetoconductance of rectangular arrays of quantum rings. *Phys. Rev. B*, 78:125306, 2008.

[132] A. W. Cummings, R. Akis, and D. K. Ferry. Spin rotations and non-abelian phases in quantum wire networks. *AIP Conf. Proc.*, 893:1115, 2007.

[133] Péter Földi, Balázs Molnár, Mihály G. Benedict, and F. M. Peeters. Spintronic single-qubit gate based on a quantum ring with spin-orbit interaction. *Phys. Rev. B*, 71:033309, 2005.

[134] X. F. Wang and P. Vasilopoulos. Spin-dependent magnetotransport through a mesoscopic ring in the presence of spin-orbit interaction. *Phys. Rev. B*, 72:165336, 2005.

[135] Satofumi Souma and Branislav K. Nicolić. Spin hall current driven by quantum interferences in mesoscopic rashba rings. *Phys. Rev. Lett*, 94:106602, 2005.

[136] S. Bellucci and P. Onorato. Filtering of spin currents based on a ballistic ring. *J. Phys.: Cond. Mat*, 19:395020, 2007.

[137] J. Nitta, Y. Lin, T. Akazaki, and T. Koga. Gate-controlled electron g factor in an inas-inserted-channel in0.53ga0.47as/in0.52al0.48as heterostructure. *Appl. Phys. Lett.*, 83:4565, 2003.

[138] B. Molnár, P. Vasilopoulos, and F. M. Peeters. Magnetoconductance through a chain of rings with or without periodically modulated spin-orbit interaction strength and magnetic field. *Phys. Rev. B*, 72:075330, 2005.

[139] Zhenyue Zhu, Yong Wang, Ke Xia, X. C. Xie, and Zhongshui Ma. Time-reversal aharonov-casher effect in mesoscopic rings with spin-orbit interaction. *Phys. Rev. B*, 76:125311, 2007.

[140] Orsolya Kálmán, Péter Földi, Mihály G. Benedict, and F. M. Peeters. Magnetoconductance of rectangular arrays of quantum rings. *Phys. Rev. B*, 78:125306, 2008.

[141] Marc van Veenhuizen and Jagadeesh Moodera. Electron deflector in uhv system: Scattered electrons in ebeam evaporation. *Rev. Sci. Instr.*, 79:033907, 2008.

[142] K. S. Sree Harsha. *Principles of Physical Vapor Deposition of Thin Films.* Elsevier, 2006.

[143] K.-D. Schock, F. E. Prins, S. Strähle, and D. P. Kern. Resist processes for low-energy electron-beam lithography. *J. Vac. Sci. Technology B*, 15:2323, 1997.

[144] Y-K Kim and M. E. Rudd. Binary-encounter-dipole model for electron-impact ionization. *Phys. Rev. A*, 50:3954, 1994.

[145] P. L. Bartlett and A. T. Stelbovics. Calculation of electron-impact total-ionization cross sections. *Phys. Rev. A*, 66:012707, 2002.

[146] Eric Perozziello. Silicon thermal oxide thickness calculator.

[147] Z. Y. Zhao, D. Hendrix, L. Y. Wu, and B. K. Cusson. Ion implantation angle variation to device performance and the control in production. *AIP Conf. Proc.*, 680:666–669, 2003.

[148] John G. Simmons. Generalized formula for the electric tunnel effect between similar electrodes separated by a thin insulating film. *J. Appl. Phys.*, 34:1793, 1963.

[149] John G. Simmons. Electric tunnel effect between dissimilar electrodes separated by a thin insulating film. *J. Appl. Phys.*, 34:2581, 1963.

[150] E. H. Rhoderick and R. H. Williams. *Metal-Semiconductor Contacts*, volume 19 of *Monographs in Electrical and Electronic Engineering.* Clarendon, Oxford, 3 edition, 1988.

[151] M. W. J. Prins, R. Jansen, R. H. M. Groenevel, A. P. van Gelder, and H. van Kempen. Photoelectrical properties of semiconductor tips in scanning tunneling microscopy. *Phys. Rev. B*, 53:8090, 1996.

[152] V. J. Goldman, D. C. Tsui, and J. E. Cunningham. Observation of intrinsic bistability in resonant-tunneling structures. *Phys. Rev. Lett.*, 58:1256, 1987.

[153] F. W. Sheard and G. A. Toombs. Space-charge buildup and bistability in resonant-tunneling double-barrier structures. *Appl. Phys. Lett.*, 52:1228, 1988.

[154] Zhenhong Dai and Jun Ni. Tuning bistability and current hysteresis in resonant-tunneling structures. *Phys. Rev. B*, 73:113309, 2006.

[155] G. G. Kareva. Transformation of a metal-oxide-silicon structure into a resonance-tunneling structure with quasi-zero-dimensional quantum states. *Semiconductors*, 33:883–885, 1999.

[156] H. Park, J. Qi, Y. Xu, K. Varga, S. M. Weiss, B. R. Rogers, G. Lüpke, and N. Tolk. Characterization of boron charge traps at the interface of Si/SiO_2 using second harmonic generation. *Appl. Phys. Lett.*, 95:062102, 2009.

[157] R. Guerrero, V. V. Pryadun, F. G. Aliev, R. Villar, J. L. Martinez, and J. Moodera. Complex magnetic response in magnetic tunnel junctions determined via magnetic and transport measurements. *Mat. Res. Soc. Symp. Proc.*, 746:Q2.9.1, 2003.

[158] H. T. Hardner, M. B. Weissman, M. B. Salamon, and S. S. P. Parkin. Fluctuation-dissipation relation for giant magnetoresistive $1/f$ noise. *Phys. Rev. B*, 48:16156, 1993.

[159] William D. Stanley. *Operational amplifiers with linear integrated circuits.* Prentice Hall, 4 edition, 2002.

[160] James K. Roberge. *Operational amplifiers - theory and practice.* John Wiley & Sons, Inc., 1975.